2018

Cavity-Coupled Plasmonic Systems for Enhanced Light-Matter Interactions

Abraham Vazquez-Guardado
University of Central Florida

CAVITY-COUPLED PLASMONIC SYSTEMS FOR ENHANCED LIGHT-MATTER INTERACTIONS

by

ABRAHAM VÁZQUEZ-GUARDADO
B.E. Universidad Autónoma de Nayarit, 2007
M.S. Instituto Nacional de Astrofísica Óptica y Electrónica, 2012
M.S. University of Central Florida, 2016

A dissertation submitted in partial fulfilment of the requirements
for the degree of Doctor of Philosophy
in the College of Optics and Photonics, CREOL,
at the University of Central Florida
Orlando, Florida

Spring Term
2018

Major Professor: Debashis Chanda

ABSTRACT

Light-matter interaction is a pivotal effect that involves the synergetic interplay of electromagnetic fields with fundamental particles. In this regard localized surface plasmons (LSP) arise from coherent interaction of the electromagnetic field with the collective oscillation of free electrons in confined sub-wavelength environments. Their most attractive properties are strong field enhancements at the near field, highly inhomogeneous, peculiar temporal and spatial distributions and unique polarization properties. LSP systems also offer a unique playground for fundamental electromagnetic physics where micro-scale systemic properties can be studied in the macro-scale. These important properties and opportunities are brought up in this work where I study hybrid cavity-coupled plasmonic systems in which the weak plasmonic element is far-field coupled with the photonic cavity by properly tuning its phase. In this work I preset the fundamental understanding of such a complex systems from the multi-resonance interaction picture along experimental demonstration. Using this platform and its intricate near fields I further demonstrate a novel mechanism to generate superchiral light: a field polarization property that adds a degree of freedom to light-matter interactions at the nanoscale exploited in advanced sensing applications and surface effect processes. Finally, the detection of non-chiral analytes, such as proteins, neurotransmitters or nanoparticles, and more complex chiral analytes, such as proteins and its conformation states, amino acids or chiral molecules at low concentrations is demonstrated in several biosensing applications. The accompanied experiential demonstrations were accomplished using the nanoimprinting technique, which places the cavity-coupled hybrid plasmonic system as a unique platform towards realistic applications not limited by expensive lithographic techniques.

ACKNOWLEDGMENTS

In the quest of pursuing life goals oneself faces two options: look from afar and sit silent observing opportunities pass or challenge yourself and fight every day to reach proudly to the summit. However, one always benefits the support and encouragement from others to shake-off the fear and relief the intricate path laying ahead. This is why I really thank and appreciate the support from family, friends, mentors and sponsors for helping me getting to where I am now.

I am deeply thankful with my parents, for teaching me to seek my goals no matter the obstacles I face in the pathway. I am thankful to have them there for me in the harsh and joyful moments of my life. My whole family was always noticed in the process, from siblings, cousins, to aunts and uncles whose support was always there for me and will never be forgotten. There is a special place in these lines for that person who stood by my side along the way: my wife, with whom I share this accomplishment. I truly appreciate her support in the whole extent.

I thank my mentor for his guidance and support in this quest. I am thankful for his advice and motivation to stand out outside the crowd and help me getting the best out of myself. I acknowledge the administrative support from CREOL and NanoScience Technology Center, and the University of Central Florida, for enabling my ongoing development throughout these years. Their staff was very helpful and supportive.

I want to acknowledge the Consejo Nacional de Ciencía y Technología (CONACyT) for awarding the fellowship to pursue my PhD program in the College of Optics and Photonics (CREOL), University of Central Florida. In addition, I acknowledge the Secretaría de Educación Pública (SEP) for the compliment fellowship I received.

TABLE OF CONTENTS

LIST OF FIGURES

LIST OF TABLES

1. INTRODUCTION

1.1. Background.

Light-matter interaction is the most fundamental phenomenon that has allowed the advance of science and technology. It is how the fundamental particles are contained within the volume of matter that dictates its optical and electronic properties. Henceforth, insulators, metals and semiconductors all have very unique optical properties and interaction regimes depending on the photon's energy. Metals, for instance, are dominated by the high free-electron density in the conduction band that allows, not only its high conductivity, but plasma oscillation when driven by external electromagnetic radiation at the right momentum transfer condition imposed by the geometry of the system.

Plasma waves where first discussed by Sommerfeld and Zenneck as the mathematical solution of propagating surface waves supported on the surface of a conductor material with finite conductivity [2,3]. Around the same time Wood was experimenting with metallic gratings that led to the finding of anomalous absorption bands in the reflected spectra of visible light [4]. However, these works stayed uncorrelated until 1941 when Fano linked these theoretical predictions and the anomalous reflection of metallic gratings with his theory of anomalous diffraction gratings [5]. In addition, Ritchie's subsequent work on diffraction of electron beams in metallic foils, and other following him, established an empirical relation between the energy loss of electron beam and its interaction with the metallic films observed in his experiments, and successfully linked his experimental findings with previous Wood's work [6–9]. At the same time, Kretschmann and Raether were able to experimentally prove the excitation of Sommerfeld's surface wave using prism coupling at visible wavelengths [10], followed by Otto [11]. The sequel of these works nailed the concept of surface plasmon polariton as the result of collective oscillation of free electrons coupled to external electromagnetic stimulation [12–14]. Nevertheless it was with the advent of micro

and nanofabrication techniques that triggered the field's flourishing.

1.2. The surface plasmon.

Two fundamental surface plasma wave oscillations are sustained in the dielectric and metals interface, and other highly conductive materials, depending on the geometrical configuration of the system: propagating surface plasmon-polaritons (SPP) supported on planar metal-dielectric interfaces [14–19] and localized surface plasmons (LSP) supported on subwavelength structures [20–24].

In one hand, SPP are propagating TM waves that couple to longitudinal charge oscillation in the metal/dielectric interface. They are short-lived excitation due to the inherent dissipative nature of metal [14]. The main characteristic is the exponential decay of the electric field that results from the collective electron gas oscillation and is maximum right at the dielectric/metal interface. For this surface waves to be excited the correct moment matching condition needs to be satisfied in order to couple free-space electromagnetic radiation to surface plasmons, hence the delay from the theoretically prediction made by Sommerfeld and Zenneck to the first experimental demonstration made by Kretschmann, Raether and Otto.

On the other hand, LSP appears as natural solution of scattering by small conductive particles [25]. The external field polarizes the free electrons confined within the geometrical constrain of the conductor. The polarized charge produces a restoration force opposing the incident field, hence at a particular frequency a resonant effect is observed that is accompanied with strong extinction due to resonant scattering and absorption processes. In the electrostatic regime, the particle is much smaller that the exciting wavelength of light, the solution to the Laplace equation provides the normal modes of oscillation for the subwavelength particle. For a spherical geometry the fundamental mode have a dipolar characteristic with a resonant frequency well defined by the Mie theory [26, 27].

Both types of surface plasmons have in common the capability to generate highly localized

field right at the interface with field intensities several orders of magnitude larger that the incident field. This property has found keen niche of applications in field-enhanced processes such as surface-enhanced Raman spectroscopy [28–30], plasmonic-enhanced nonlinear effects [31–33] or even cancer therapy based on local heat generation [34–36]. In addition, the resonant scattering cross section enhancement has allowed to employ metallic nanoparticles as inorganic labels, for example in nanoparticle-assisted tracking system [37,38], cell/biomolecules labeling detection and imaging [34, 39, 40].

Another interesting property of SPP and LSP is the strong susceptibility to the refractive index of the surrounding medium. Any change in the refractive index of the material in contact with the metal will reduce the particle polarizability, hence a reduction in the restoration force will translate to an spectral red-shift traceable by spectroscopic methods. Refractometric sensing methods employ this effect in bulk refractive index sensing [41–47] or surface sensing in biological applications [48–54].

Unlike SPP, LSP resonance can be tuned not only by changing the surrounding environment but also with the particle size and shape [55]. These two additional degrees of freedom enrich the property of LSP systems where optical properties, such as light scattering and absorption, are crucial. At resonance ohmic losses can severely degrade the surface plasmon performance. For example, SPP modes excited near the resonant plasma frequency propagates just hundreds of nanometers after the initial energy is almost dissipated in the metal. This effect hinders the promising technological benefits of this motivating phenomenon, such as light transmission over sub diffraction metallic waveguides [56, 57]. Nevertheless, the spurious absorption is an essential effect in other applications. In periodic array of nanoparticles or perforated metallic thin films the ability to remove a finite band of a broadband source has made possible for scientist to create reflective [58–60] or transmissive [61–63] optical filters. Perfect absorbers [64–67], broadband absorbers [66,68–72], are also obvious applications of this, somehow detrimental, effect in plasmonic systems. With the capability of LSP resonance tuning the absorption band can be conveniently

tuned satisfying the requirements of the application making this way LSP phenomenon even more attractive.

The list of applications seems to never end and can keep going for ever, for example hot-electron generation [46, 73, 74], extraordinary light transmission [75–78], control emission of radiation [79–82], lasing [83–87], circular dichroism [88–95], superchiral light generation [96–104], negative index metamaterials [105–112] and so on. Furthermore, LSP systems also work as a playground for fundamental science where more complex electromagnetic phenomena can be studied from the point of view of enhanced light-matter interactions or electrodynamics. For example, plasmonic coupling in photonic cavities, [113, 114], multi-particle coupling [115–118], Rabi oscillations [119, 120], optical forces [121–124], quantum electrodynamics [125–130], and so on.

1.3. The scope of this work.

In this work I study a simple hybrid plasmonic system, yet electromagnetically complex and rich of fundamental physics and several application possibilities. The core plasmonic element is comprised of a two dimensional (2D) array of plasmonic elements, either holes on a perforated metallic thin film, or same hole array but coupled to its complementary disk array. Two interaction regimes are considered: one with respect to the periodicity of the array and the other with respect to he hole-disk dimension compared with the excitation wavelength. In the first scenario, diffraction effects can be induced when the incident wavelength is equal or smaller that the array periodicity. Furthermore, the second effect is when the wavelength is compared to the plasmonic geometrical dimensions, in this case the diameter. When it is larger that the diameter the system is under the quasi-static approximation whose response is dominated by the first order dipole expansion. However, if it becomes comparable to the wavelength, higher order dipole excitation are supported. When coupled to an asymmetric photonic cavity, an additional set of properties and effects are brought to perspective as not only the geometry of the plasmonic system determines the net sys-

tem polarizabitliy but its coherent interaction the with the cavity. Consequently, full inhibition or enhanced excitation of the plasmonic resonance is possible and strictly depend on the cavity phase.

Such a complex interaction of cavity and plasmonic system under the two aforementioned interaction regimes is discussed in this work both theoretical and experimentally. In Chapter 2 a the cavity-coupled plasmonic system is studied under the diffraction and non-diffraction regimes for wavelengths slightly larger that the hole diameters. It is found that diffraction orders, along with its polarization properties, have strong influence in the dispersion of the system. In such section I employ the effective index method along the numerical finite difference time domain (FDTD) technique to understand and describe the physics behind this multi-resonant system. In Chapter 3 I describe a second interaction regime; when the wavelength is larger than the geometric parameters of the system. In this regime the metallic grating does not support plasmonic resonances; however, due to the selective polarizability induced by the cavity on the metallic elements, strong plasmonic resonances are induced which are governed by the cavity dispersion. In this particular chapter, single-sign superchiral light generation is demonstrated in the 2D symmetric and achiral plasmonic system unlike previous believes. This unique system performance is achieved not by the local near-field generation but its temporal distribution as theoretically demonstrated.

This work is application focused in which non-traditional lithography techniques are employed to mass produce the plasmonic substrates used in biosensning. In this regard Chapter 4 contains the fabrication and characterization methods employed, such as the nanoimprinting lithography technique, transfer printing methods and soft lithography for microfluidic channel fabrication; and the corresponding optical characterization techniques and related multi-system integration. Finally, Chapter 5 contains the demonstration of biosensing of several analytes: nanoparticles, proteins, and neurotransmitters (dopamine and epinephrine). The integration with microfluidic channel systems and demonstration of analyte detection in whole blood, where plasma is being extracted directly from blood in real time, is the culprit of this work. Such a demonstrations position this plasmonic substrate as a promising technology for point-of-care applications.

2. CAVITY-COUPLED PLASMONIC SYSTEMS

2.1. Introduction.

Recently, strong electromagnetic coupling between plasmonic and photonic cavity modes have been demonstrated in hybrid LSPR Fabry-Perot (FP) cavities. The coherent interaction of the cavity with the plasmon allows rich interaction that brings new application to plasmon-enhanced processes. In these interacting systems two distinct configurations are common encountered: plasmonic element inside [114, 131] and at one [132–134] and both ends [135–138] of the FP cavity. In the first type of configuration the coupling is studied from cavity-atom picture in quantum electrodynamics based on the couple oscillator model; however, it predicting model suffers from the limitation in estimating the coupling coefficient [114, 131]. In the second case the coupling has been studied theoretically using the Fourier modal [132, 135], scattering matrix [137–139], numerical finite difference time domain (FDTD) method [133, 135] and finite integration technique [136] as a function of cavity length. Focusing on the second case, the presence of a back mirror influences surface plasmon excitation constructively or destructively, resulting in strong LSPR enhancement or complete suppression [114, 133, 140]. However, the true nature and origin of this plasmonic-photonic interaction is yet to be understood in systems where high order diffraction, LSPR and cavity resonances overlap in space and frequency.

In this section the cavity-coupled plasmonic system is studied in three different domains: in visible band with and without supporting high order diffraction orders, in the infrared (IR) domain where the cavity interact solely by the fundamental plasmonic mode and in the IR where plasmonic modes are induced by the resonating cavity. The physical understanding of the system will be carried out using the analytical effective index and transfer matrix approaches in conjunction with the FDTD computational method to elucidate the nature of several interaction mechanisms present within the characteristic dispersion of a cavity-coupled plasmonic system.

2.2. Theoretical methods.

2.2.1. The transfer matrix formalism.

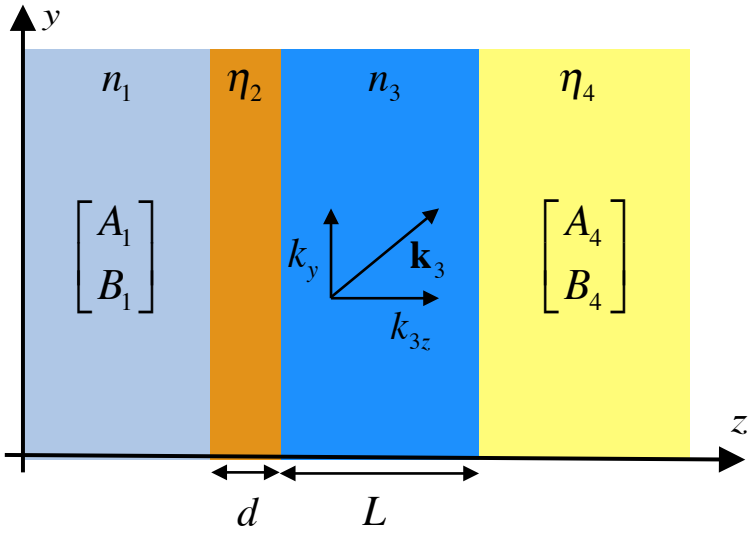

Figure 1: Graphical representation of the multi-layer stack. Medium 1: is the semi-infinite air region, medium 2: the effective medium of fixed thickness d, medium 3: the dielectric filling the optical cavity with variable thickness L and medium 4: the optically thick metal back reflector. η_j is the complex refractive index of metals and n_j the refractive index of lossless dielectrics.

Detailed derivation of transfer matrix formalism can be found in [141]. Consider four homogeneous, linear and isotropic multi-layer stack, as observed in Fig. 1. The transverse electric (TE) or transverse magnetic (TM) field $\mathbf{F}$ in the j^{th} material slab, for arbitrary polarization, can be represented as

$$\mathbf{F} = \hat{\mathbf{a}} \left(A_j e^{-i\mathbf{k}_j \cdot \mathbf{n}} + B_j e^{+i\mathbf{k}_j \cdot \mathbf{n}} \right) e^{-i\mathbf{k}_j \cdot \mathbf{t}}, \tag{1}$$

where $\hat{\mathbf{a}}$ is the polarization vector, A_j and B_j are the field magnitude of the forward and backward propagating plane waves in the j^{th} material slab, respectively, $\mathbf{k}_j$ is the propagation vector and $\mathbf{n}$ and $\mathbf{t}$ are its normal and transverse vector components, respectively. Consider the reference plane as shown in Figure S4, yz plane of incidence. The wave vectors satisfy the relation $\mid \mathbf{k}_j \mid^2 =$

$k_0^2\eta_j^2 = k_y^2 + k_{jz}^2$, where k_0 is the wave vector in vacuum and η_j the complex refractive index in the j^{th} layer, *i.e.* $\eta_j = n_j + i\kappa_j$. At the boundary between slab j^{th} and slab l^{th} the field components are related as

$$\begin{bmatrix} A_j \\ B_j \end{bmatrix} = \frac{1}{t_{jl}} \begin{bmatrix} 1 & r_{jl} \\ r_{jl} & 1 \end{bmatrix} \begin{bmatrix} A_l \\ B_l \end{bmatrix} = \mathbf{T}_{jl} \begin{bmatrix} A_l \\ B_l \end{bmatrix}, \tag{2}$$

where $r_{jl} = (\tilde{k}_{jz} - \tilde{k}_{lz})/(\tilde{k}_{jz} + \tilde{k}_{lz}) = \hat{r}_{jl}e^{i\varphi_{jl}}$, $t_{jl} = 2\tilde{k}_{jz}/(\tilde{k}_{jz} + \tilde{k}_{lz}) = \hat{t}_{jl}e^{i\varphi_{jl}}$ and $\tilde{k}_{jl} = k_{jl}$ or $\tilde{k}_{jl} = k_{jl}/\eta_j^2$ for TE or TM polarization, respectively. $\mathbf{T}_{jl}$ is called the transition matrix from the j^{th} to the l^{th} layer. Similarly, the propagation phase the plane wave acquires after propagating in the j^{th} layer of thickness d_j is

$$\begin{bmatrix} A_j \\ B_j \end{bmatrix} = \begin{bmatrix} e^{ik_{jz}d_j} & 0 \\ 0 & e^{-ik_{jz}d_j} \end{bmatrix} \begin{bmatrix} A'_j \\ B'_j \end{bmatrix} = \mathbf{P}_j \begin{bmatrix} A'_j \\ B'_j \end{bmatrix}, \tag{3}$$

where A_j and B_j are the field coefficients at one end of the layer and A'_j and B'_j the field coefficients at the other end. $\mathbf{P}_j$ is called the propagation matrix. The transfer matrix $\mathbf{M}$ for the entire system is obtained by combining transition and propagation matrix in the stack, hence we obtain:

$$\begin{bmatrix} A_1 \\ B_1 \end{bmatrix} = \mathbf{T}_{12}\mathbf{P}_2\mathbf{T}_{23}\mathbf{P}_3\mathbf{T}_{34} \begin{bmatrix} A_4 \\ B_4 \end{bmatrix} = \mathbf{M} \begin{bmatrix} A_4 \\ B_4 \end{bmatrix} \tag{4}$$

Finally, the reflection coefficient from the stack can be obtained from Eq. 4 as $r = B_1/A_1 = M_{21}/M_{11}$.

2.2.2. The Fabry-Perot resonator.

Consider a three medium system such as $n_1 \neq n_2 \neq n_3$ where the n_i is the refractive index of the i^{th} film. The presence of two boundaries will incur in two reflection instances. The coherent interaction produce constructive or destructive interference, observed as reflection minima or

maxima depending on conditions such as the propagation phase and refractive indices contrasts. Although the classical Fabry-Perot resonator is the most straightforward example of photonic resonator, these type of resonators are present in may complex systems too. The scope of this work is on studying the optical performance of asymetric fabry-perot resonators as observed in the four-stack multilayer system observed in Fig. 1.

Consider the four layer stack shown in Fig 1, where d_2 is substituted by d, which represent the thickness of the effective index medium and d_3 for L, the variable dielectric layer thickness, which in our case will represent the thickness of an asymmetric cavity. The general equation for the reflection coefficient, after proper matrix multiplication, reads as follows:

$$r = \frac{\hat{r}_{12}e^{i\varphi_{12}} + \hat{r}_{23}e^{-i(2\beta d-\varphi_{23})}e^{-2\gamma d} + \hat{r}_{34}e^{-i(2k_{3z}L-\varphi_{34})}\left(e^{-2(i\beta+\gamma)d} + \hat{r}_{12}\hat{r}_{23}e^{i(\varphi_{12}+\varphi_{23})}\right)}{1 + \hat{r}_{12}\hat{r}_{23}e^{-i(2\beta d-\varphi_{12}-\varphi_{23})}e^{-2\gamma d} + \hat{r}_{34}e^{-i(2k_{3z}L-\varphi_{34})}\left(\hat{r}_{23}e^{i\varphi_{23}} + \hat{r}_{12}e^{-2(i\beta+\gamma)d}e^{i\varphi_{12}}\right)}. \quad (5)$$

In this result, the propagation phase in the thin medium $k_{2z} = \beta - i\gamma$ includes phase $\beta = k_0\mathrm{Re}[n_2]$ and the attenuation coefficient $\gamma = k_0\mathrm{Im}[n_2]$, which will play a significant role when calculating the effective parameter of a patterned thin film using numerical methods. In Fig. 2(a) the reflectance dispersion as a function of cavity thickness L for an asymmetric Fabry-Perot resonator comprised of a semitransparent gold thin film with $d = 30$ nm and optically thick back mirror separated by a dielectric film with $n_3 = 1.56$: also known as the Gires-Tournois resonator. The incident medium is air ($n_1 = 1$) and the gold substrate is considered infinite.

The dispersion spectra given by Eq. 5 and observed in Fig. 2(a) shows strong absorption bands and high reflective bands of this asymmetric photonic resonator. The frequency location at which these condition happens follow the classical phase equation for constructive and destructive interference. Consider the reflection phase off the gold thin film, ρ_F from the dielectric medium, and reflectance phase off the thick reflector (back mirror) at the dielectric-metal interface, ρ_{BM}. The propagation phase inside the cavity ϕ is given by the optical path length, *i,e.* $k_0 n_3 L$. There

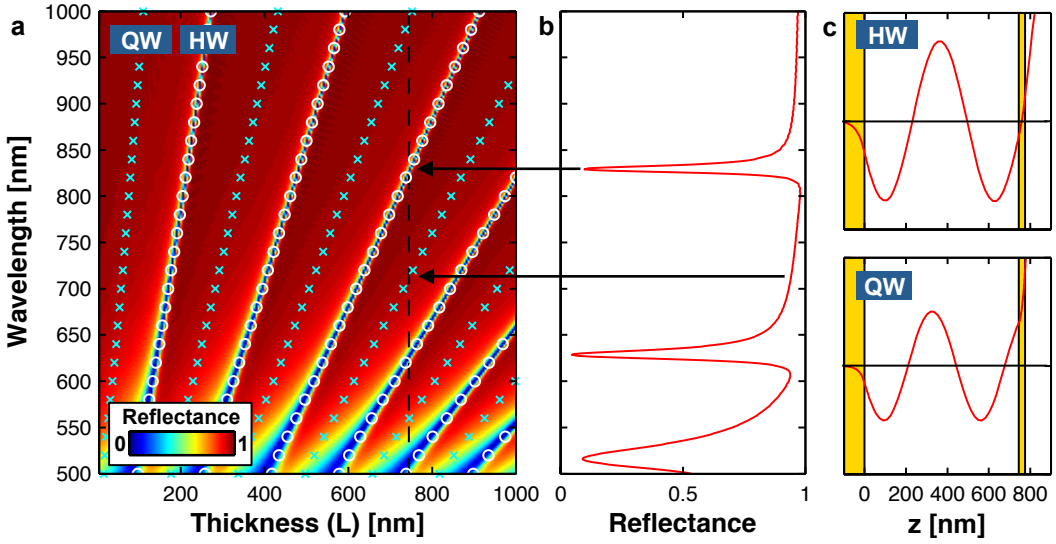

Figure 2: (a) Reflectance dispersion for an asymmetric Fabry-Perot cavity. (b) Reflectance at a thickness of 745 nm. (c) Electric field for two conditions of the cavity, HW (top) and QW (bottom).

will be a photonic resonant mode if the total phase is an integer even multiple of π

$$2\phi - \rho_F - \rho_{BM} = 2s\pi. \tag{6}$$

where s is the mode order. The resonant mode is observed as standing wave inside the cavity with close to zero reflectance. On the other hand, there will be mode rejection or full reflectance when the round trip phase is an odd multiple of π, also known as a quarter wave condition,

$$2\phi - \rho_F - \rho_{BM} = (2s+1)\pi. \tag{7}$$

This set of condition will play a key role in determining the cavity-coupled plasmonic interactions.

2.2.3. The effective index method.

The transfer matrix for an arbitrary slab of refractive index n and thickness d at normal incidence under asymmetric environment, *i.e* $n_i \neq n_f$, can be generally expressed as:

$$M = \frac{1}{2}\begin{bmatrix} 1 & -1/\kappa_1 \\ 1 & -1/\kappa_1 \end{bmatrix}\begin{bmatrix} \cos\delta & -i/\kappa_f \sin\delta \\ i\kappa_f \sin\delta & \cos\delta \end{bmatrix}\begin{bmatrix} 1 & 1 \\ -\kappa_2 & -\kappa_2 \end{bmatrix} \tag{8}$$

where κ_1, κ_2 and κ_f are the normal wavenumbers in the incident, film and exit media and k_0 is the wavenumber of light in vacuum. At normal incidence $\kappa_i = k_0 n_i/\mu_i$ for TE polarization and $\kappa_i = k_0 n_i/\varepsilon_i$ for TM polarization, which apply for the incident and substrate media. For the film $\kappa_f = k_0/Z$ for TE and , $\kappa_f = k_0 Z$ for TM, respectively, where Z is the film impedance given by $Z = \sqrt{\mu_f/\varepsilon_f}$. The resulting matrix will lead to reflection r and transmission t coefficients of the above film as $r = C/A$ and $t = 1/A$.

$$r = \frac{(\kappa_1 - \kappa_2)\cos(k_0 nd) + i(\kappa_f - \kappa_1\kappa_2/\kappa_f)\sin(k_0 nd)}{(\kappa_1 + \kappa_2)\cos(k_0 nd) - i(\kappa_f + \kappa_1\kappa_2/\kappa_f)\sin(k_0 nd)} \tag{9}$$

$$t = \frac{2\kappa_1}{(\kappa_1 + \kappa_2)\cos(k_0 nd) - i(\kappa_f + \kappa_1\kappa_2/\kappa_f)\sin(k_0 nd)} \tag{10}$$

The inversion of these two coupled transcendental equations leads to [142–144]:

$$\cos(k_0 nd) = a\frac{n_1(1 - r^2) + n_2 t^2}{t[(n_1 + n_2) - r(n_1 - n_2)]} = X. \tag{11}$$

The factor $a = 1$ is for TE and $a = n_1/n_2$ for TM polarizations, which make no distinction for symmetric environments, *i.e.* normal angle of incidence and equal substrate and superstrate media. From Eq. 11 we can obtain $e^{ik_0 nd} = X \pm i\sqrt{1 - X^2}$ and the effective index becomes,

$$n = \frac{1}{k_0 d}\left\{\mathrm{Im}\left[ln\left(X \pm i\sqrt{1 - X^2}\right)\right]\right\} - i\frac{1}{k_0 d}\mathrm{Re}\left[ln\left(X \pm i\sqrt{1 - X^2}\right)\right]. \tag{12}$$

Equation 12 is straightforward to solve knowing the reflection and transmission coeffients but its complex nature can lead to ambiguous solutions. However, knowing that the material is passive it constrains the solution of the imaginary part, *i.e.* $\mathrm{Im}[n] \geq 0$. The real part, on the other hand, can follow different branches due to the nature of the logarithm function solutions. Nevertheless, for such small material thickness, leads to $m = 0$, hence $\mathrm{Re}[n]$ can be determined unambiguously.

2.3. The hybrid cavity-coupled plasmonic system.

2.3.1. Multiresonance interaction in system supporting high-order diffraction.

The plasmonic system comprises of a gold thin film perforated with 500 nm diameter holes arranged in a square array with period 740 nm sitting on a dielectric slab as illustrated in Fig. 3(a). This choice of period and nanohole diameter ensures excitation of higher diffraction orders as well as LSPR over the same near-IR spectral range.

In order to identify the location of the LSPR mode, the reflectance (R) and transmittance (T) of the patterned film on the dielectric are calculated using finite difference time domain (FDTD) simulations methods over on a unit cell. The absorption is estimated by $A(\lambda) = 1 - R(\lambda) - T(\lambda)$ and shown in Fig. 3(b). The absorption peak at 879 nm indicates, in this particular case, a localized surface plasmon resonance (LSPR). This type of resonance is a low quality ($Q_{LSP} = 10$) resonance due to the highly lossy nature of the metallic system. The electric field profile 5 nm above the hole demonstrate the plasmonic nature of the resonance as observed in the strong electric field confinement along the hole, see Fig. 3(c).

This periodic 2D metallic grating introduces higher order diffracted light into the cavity whose propagation wavevector satisfies the grating dispersion equation:

$$\left(\frac{2\pi m}{P}\right)^2 + \left(\frac{2\pi n}{P}\right)^2 + k_{mnz}^2 = k_0^2 n_d^2, \tag{13}$$

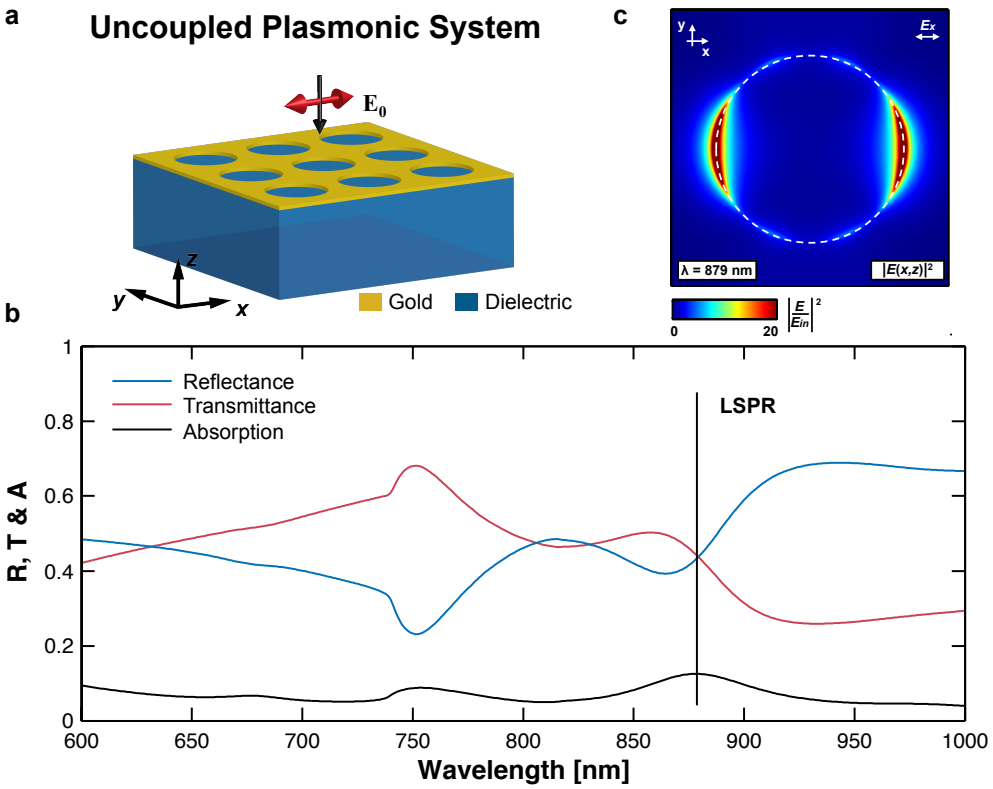

Figure 3: (a) 2D metallic grating with P = 740 nm, D = 500 nm and thickness of 30 nm. (b) Reflectance, transmittance and absorption spectra calculated using FDTD. (c) Electric field intensity enhancement 5 nm above the hole.

where P is the array period, k_{mnz} the longitudinal wavevector component, k_0 the wavevector magnitude in vacuum and (m, n) the diffraction order indices (D_{mn}). Between the wavelengths of 840 nm to 1100 nm, at normal angle of incidence, the 2D grating supports the fundamental and first diffraction orders, denoted by D_{00}, $D_{\pm 10}$ and $D_{\pm 01}$ respectively. For notational simplicity, symmetric diffraction orders are denoted as $D_{-10} = D_{+10} = D_{10}$ and $D_{-01} = D_{+01} = D_{01}$. In our chosen geometrical configuration and incident light polarization, as seen in Fig. 3(c-d), D_{01} and D_{10} are two-fold degenerate transverse electric (TE) and transverse magnetic (TM) modes as graphically represented in Fig. 4(a) and 4(b), respectively.

The cavity is now formed by combining a dielectric slab of variable thickness L and re-

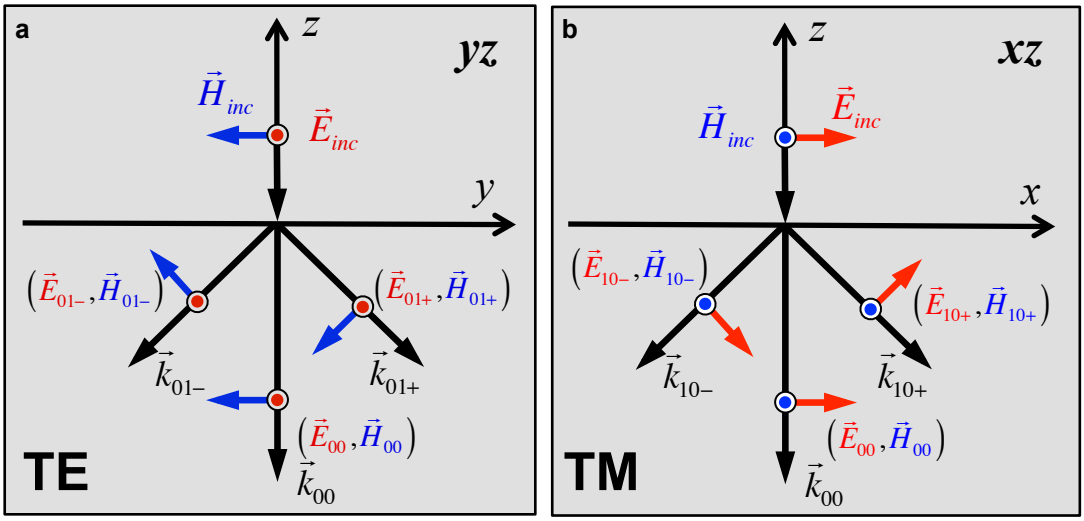

Figure 4: (a) TE and (b) TM polarization convention for the diffraction off the 2D metallic grating imposed by the incident light polarization and the angle of the diffraction propagation orders.

fractive index n_d of 1.56 sandwiched between an optically thick (200 nm) gold back reflector and a patterned thin film of gold (30 nm) as observed in Fig. 5(a). The appropriate choice of cavity thickness further enables the overlap of FP cavity resonances with the LSPR. To elucidate the optical properties of such a system, we begin with the general absorption enhancement of homogenous weakly absorbing materials in asymmetric cavities (*i.e.* dissimilar reflectivity at both ends) [141]. Such absorption is maximized when the top film is located at a quarter wave (QW) distance (antinode) from the back reflector due to constructive phase addition between incident and reflected light as dictated by Eq. 7. Weak absorption is observed when the film is located at half-wavelength (HW) distance (node) from the back reflector corresponding to a FP mode, Eq. 6.

In order to isolate the effect of diffraction and surface plasmons, the top metal is replaced by a perfect electric conductor (PEC). Such a condition states that the tangential electric field right at the boundary of the metal is zero $\mathbf{E}_t = 0$, the surface charge tends to infinity and the charge relaxation time tends to zero. This approximation models a metallic grating with the absence of surface plasmons. Diffraction orders with finite longitudinal wavevector and transverse electric

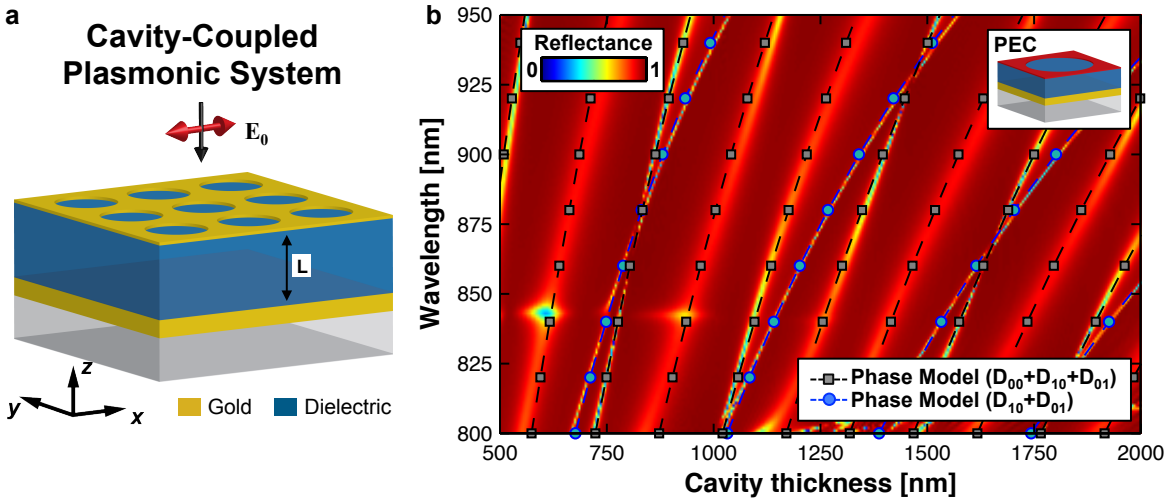

Figure 5: (a) Schematic representation of the studied plasmonic-cavity system in presence of diffraction. (b) FDTD predicted reflectance dispersion for a cavity with top PEC grating and gold back mirror. Analytical predictions from phase model have been overlaid on top for the coherent interaction between the fundamental (D_{00}) and the two degenerate first diffraction orders (D_{10} and D_{01}).

field components coexist and interfere in the cavity. The fundamental and first order modes possess different longitudinal wavevector and experience different propagation phase for the same cavity length. The first order modes, D_{01} and D_{10}, interfere constructively when the phase satisfies the following condition:

$$2k_{1z}L - \phi_1 = 2\pi q, \tag{14}$$

where $k_{1z} = k_{10z} = k_{01z}$, q is a multiple integer, and $\phi_1 = \phi_{01BM} + \phi_{01F} + \phi_{10BM} + \phi_{10F}$ is the total phase accumulated for the $(m,n)^{th}$ order from reflections off the top film (ϕ_{mnF}) and back mirror (ϕ_{mnBM}) interfaces. The fundamental and first order modes, D_{00}, D_{10} and D_{01}, interfere constructively when the phase condition becomes

$$2(k_{00} + k_{1z})L - \phi_{00} - \phi_1 = 2\pi l, \tag{15}$$

where l is a integer multiple, k_{00z} is the longitudinal wavevector and is the total phase due to the reflection at the top film and back mirror for D_{00}.

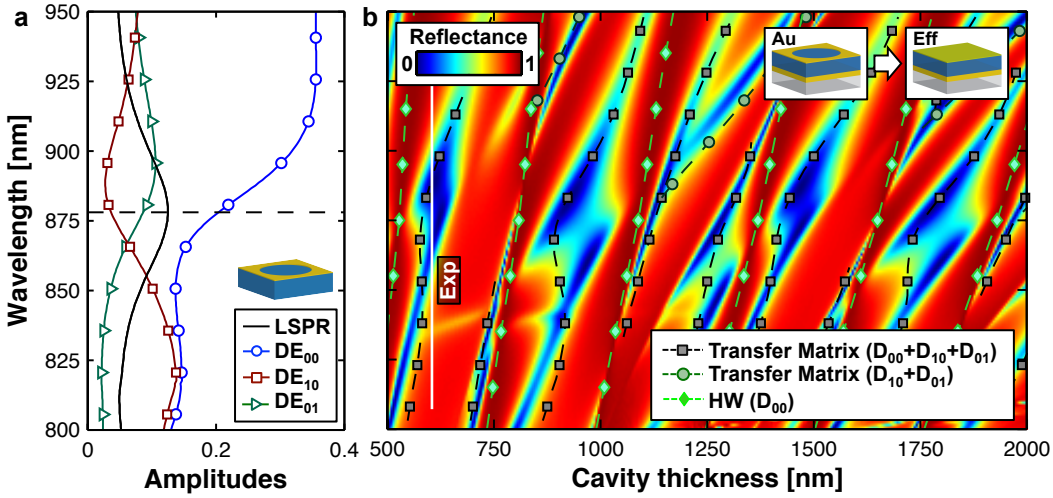

Figure 6: (a) Absorption spectrum (black line) for the perforated gold film showing a LSPR at $\lambda = 879$ nm and diffraction efficiencies for the fundamental D_{00} (blue) and first order modes D_{10} (red) and D_{01} (green). (b) FDTD predicted reflectance spectra for the cavity with top gold pattern. Analytical predictions from transfer matrix have been overlaid on top.

The reflectance spectra for cavity thickness spanning from 500 nm to 2 μm was calculated using FDTD for x-polarized light as shown in Fig. 5(b). Due to the absence of plasmon resonances on the patterned PEC film, Fig. 5(b) purely captures cavity modes induced by diffraction. An experimentally fitted dispersion was used for gold back mirror based on two pole Lorentzian Drude model [145]. On top of the FDTD color plot, the closed form dispersion curves for the HW condition are plotted for the combined D_{10} and D_{01} orders (circle dashed blue line) as described by Eq. (14) and the combination of D_{00}, D_{10} and D_{01} (square dashed black line) as defined by Eq. (15). In the analytical phase model, the phase upon reflection from the top film for all diffraction orders is considered π for the PEC case whereas the phase from reflection on the gold back mirror was calculated from the Fresnel coefficients for the appropriate polarization and wavelength dependent angle of incidence for the first diffraction order. Dips in reflectance are observed as light is coupled

into resonant waveguide modes. The aforementioned intra-cavity multiple beam interference that originates in the absence of plasmon resonance is exploited to identify the interaction between diffraction orders and their spectral dispersion in real metals.

The real interaction scenario happens when the top grating includes the phenomenological information of the plasmon modes. Hence PEC top nanohole array is replaced with a patterned gold film. The effect will be observed as a perturbation to the previously analyzed cavity supporting different photonics modes introduced by the grating diffraction orders. As observed in Fig. 3(c) the electric field distributions clearly show a predominantly dipolar LSPR corresponding to the absorption peak at 879 nm. Diffraction efficiencies computed from far-field projection of the transmission spectrum are also plotted in Fig. 6(c) indicating wavelength dependent relative strengths of major diffraction orders (D_{00}, D_{01} and D_{10}). Three distinct interaction regions between 800 and 950 nm wavelength range can be observed and are defined by the relative strength of the diffraction orders. In region one, between 800 and 850 nm, D_{10}'s strength is comparable to D_{00}'s while D_{01} is roughly an order of magnitude smaller. In the second region, D_{00} is dominant over the 900 to 950 nm wavelength band. In the third transition region, around 875 nm, the TM mode D_{10} experiences extinction due to LSPR excitation unlike its TE counterpart D_{01}. The complete system reflectance spectra are calculated using FDTD for the same wavelength and cavity thickness range, as shown in Fig. 6(b). The absorption is enhanced as well as suppressed periodically as a function of cavity length demonstrating the clear influence of the cavity on the excitation of LSPR on the patterned gold surface. The periodic modulation of the cavity dependent dispersion of LSPR differs among the first three events and repeats periodically every 860 nm as cavity thickness increases; a fact pointed out previously in the PEC case. However, the simple analytical phase model, which accurately predicted the dispersion in the PEC case, is inadequate due to the complex phase retardation on the perforated gold film in presence of LSPR.

In order to quasi-analytically model and predict this intricate resonance dispersion we employ an approach based on the effective index in transfer matrix formalism [141], as previ-

ously described. The perforated metal film is replaced with a uniform layer of equivalent wavelength dependent effective index obtained by inverting Fresnel transmission and reflection coefficients [142–144]. For this purpose the wavelength dependent reflection and transmission coefficients are extracted using FDTD simulations. Then, solving Eq. 12 the effective index can be estimated for this geometry. Since the reflection and transmission coefficients contain the information of the LSP and diffraction, a continuous film with this effective index can be employed in a multi-layer approach to better understand the complex behavior of the system in the presence of a cavity with different cavity modes resonating in the cavity. Figure 7 shows the effective index for this particular metallic 2D grating.

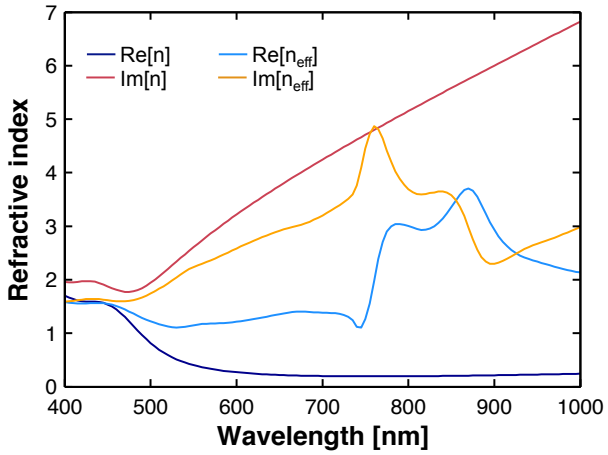

Figure 7: Effective index calculated for a 2D metallic grating with P = 740 nm, D = 500 nm and thickness of 30 nm using the effective index method.

Following the transfer matrix approach, the reflectance spectra produced by the multi-layer stack (Fig. 1) is calculated. This process is repeated for the three independent diffraction orders (D_{00}, D_{01} and D_{10}) and the final reflectance spectrum is obtained from their linear superposition.

The total reflection is obtained by incoherent addition of all modes $R_{Tot} = R_{00} + R_{01} + R_{10}$ and for the first order case $R_{Tot} = R_{01} + R_{10}$. The analytical reflectance minima are overlaid on the FDTD predictions as square dashed black lines in Fig. 6(b). In addition, the combined reflectance

spectra for D_{01} and D_{10}, following the same approach, are calculated and its minima overlaid as circle dashed green lines in Fig. 6(b). The splitting of modes takes place due to phase transition after excitation of the LSPR which is evident from the dispersion of energy density of different diffraction orders as a function of wavelength. Overall, there is excellent correspondence between FDTD predictions and the analytical model. Small discrepancies originate from the limitation of the effective medium approach when the wavelength is comparable to geometrical features. Also due to the limitation of parameter retrieval process, we assumed same effective index for the thin film under TM and TE polarization for all angles. This behavior is not present in the following diffraction-less system where pattern features are smaller than the wavelength of interest.

2.3.2. Multisesonance interaction in the non-diffraction regime.

The sub-diffraction system comprises of a cavity structurally similar to the previous one but with three key modifications: the metal is silver, the periodicity is 300 nm and the hole diameter is 200 nm. Silver was chosen to avoid the strong interband absorption of gold around 300 nm to 550 nm while the decreased 2D grating period excludes higher diffraction orders beyond 450 nm. As with the previous system, the LSPR is determined from the FDTD predicted absorption as, $A(\lambda) = 1 - R(\lambda) - T(\lambda)$, for a patterned silver film attached to a dielectric layer (n_d = 1.56), as illustrated in Fig. 3(a) but with silver instead of gold as the plasmonic material. Experimental dispersion data for silver was used from Ref. [145]. Two absorption peaks are observed, at 610 and 511 nm and represent higher order LSPR oscillations supported by the perforated film under asymmetric environment (air as superstrate and photoresist as substrate), see Fig. 8(b).

Further addition of the silver back mirror completes the cavity-coupled system. The reflectance spectra are obtained by FDTD for cavity thickness ranging from 450 to 700 nm and plotted in Fig. 10. As previously predicted, in the absence of diffraction, a single FP mode corresponding to the fundamental diffraction order is present with strong absorption enhancement around the LSPR wavelength.

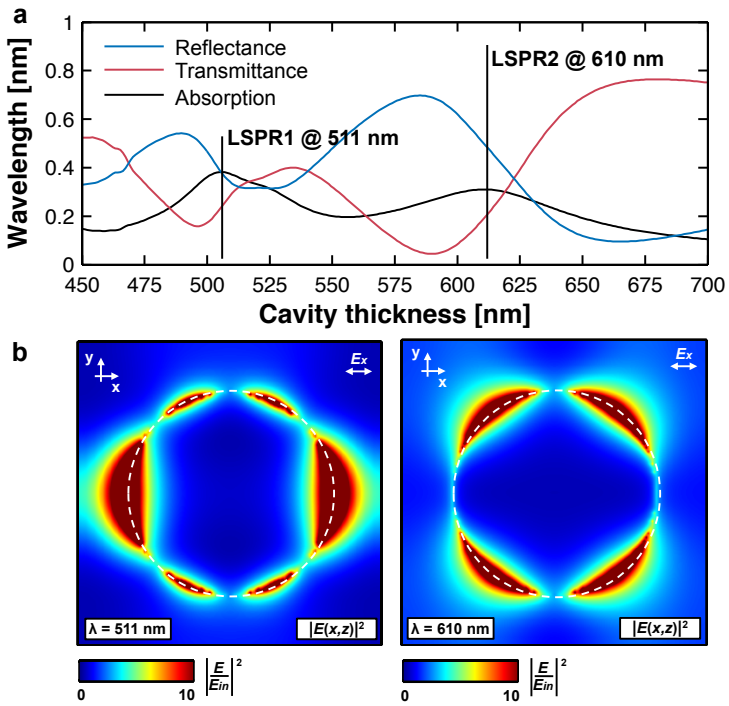

Figure 8: (a) Reflectance, transmittance and absorption spectra for a 2D silver grating with P = 300 nm, D = 200 nm and thickness of 30 nm. Two plasmon resonance are observed at $\lambda = 511$ nm and $\lambda = 610$ nm. (b) Electric field intensity profiled 5 nm above the hole at both LSP resonances.

To understand the dispersion and explain the energy exchange mechanism between photonic and plasmonic modes, previously used approaches based on analytical round trip phase for QW condition (Eq. (7)) and transfer matrix method are followed. In both approaches the top perforated film is modeled by its corresponding effective medium retrieved following the aforementioned effective index method, see Fig. 9. The first order approximation based on simple round trip phase for QW condition predicts the overall dispersion and resonance locations with some degree of accuracy, as can be seen in Fig. 10(b) as diamond dashed blue lines. However, very good correspondence is observed for the transfer matrix case, square dashed brown lines in Fig. 10(b), which includes every reflection and transmission events on all surfaces. As predicted, in a diffraction-less scenario one can observe much closer agreement between numerical simula-

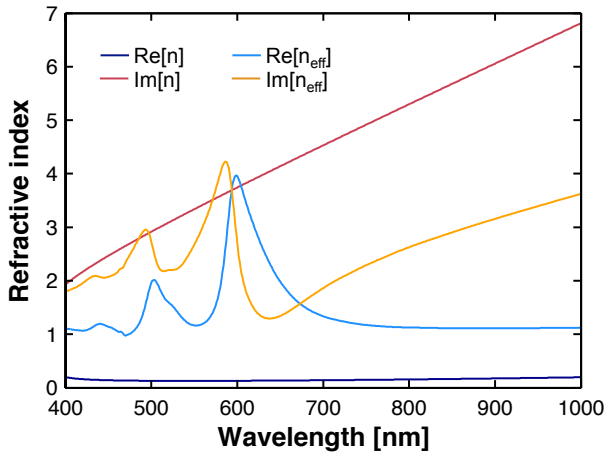

Figure 9: Effective index for a thin perforated silver film with $D = 200$ nm and $P = 300$ nm and its comparison with bulk silver refractive index.

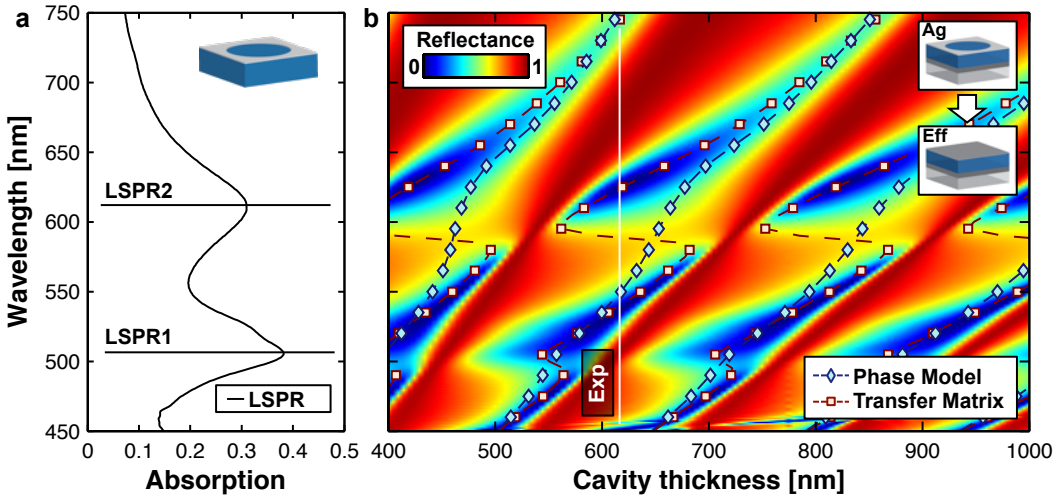

Figure 10: (a) Reflectance, transmittance and absorption spectra for a 2D silver grating with P = 300 nm, D = 200 nm and thickness of 30 nm. Two plasmon resonance are observed at $\lambda = 511$ nm and $\lambda = 610$ nm. (b) Electric field intensity profiled 5 nm above the hole at both LSP resonances.

tion and theoretical models. This is basically due to two reasons. The first one is regarding because the system is in the sub-diffraction regime. Hence not high order diffraction are present that would add additional propagation waves at non normal angle inside the cavity hence skewing the phase

calculation. The second reason is in the effective index method, which is additionally boosted by the lack of diffraction. The plasmonic resonance is slightly above the geometrical dimension of the holed film; therefore the effective index method captures the absorption and phase change by the plane wave without the interaction with the lattice that might extra momentum in the transverse direction.

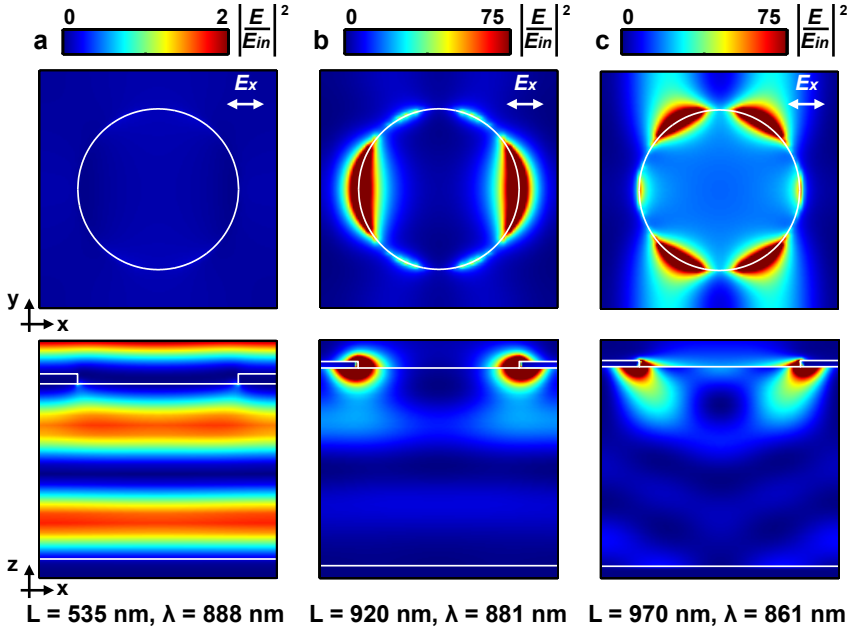

Figure 11: Top view and cross section electric field intensity profiles for different cavity length and wavelenght. (a) $L = 535$ nm and $\lambda = 888$ nm, (a) $L = 920$ nm and $\lambda = 881$ nm, (a) $L = 970$ nm and $\lambda = 861$ nm.

2.3.3. Cavity-enhanced plasmon resonance.

It is shown here that the cavity has direct effects on the plasmonic resonance which depend strictly on its phase. Figure 6 clearly shows the effect. Contrary to the regular asymmetric FP resonator where strong abosrption is observe at the HW condition, or where a standing wave is supported, the hybrid cavity-coupled plasmonic system behave differently. When the HW condition is satis-

fied the electric field is creates a node right at the top film. Therefore, the plasmonic element is poorly overlapped with the electric field producing null excitation. This effect is observed in Fig. 11(a) where the standing wave is observed inside the cavity without a plasmonic mode excitation whatsoever. On the other hand, there are other condition in which the fundamental diffraction order interacts with the first diffraction. It is this combination that strongly enhance the plasmonic resonance, for example observed in Fig. 11(b) and Fig. 11(c). As can observed in the field profile within the cavity Fig. 11(b) is dominated by the fundamental zeroth order diffraction mode parallel phase fronts are present. This is not the case for the Fig. 11(c) in which slated phase front are observed that suggest non-normal propagation direction of the mode supported in the cavity.

This discussion opens the opportunity to dynamically tune the plasmonic mode based on cavity phase. This effect would be possible by either mechanically tuning the cavity thickness or employing an active cavity material that allows its refractive index change by an external stimulus, for example heat, electric field, electrical current or saturable absorption. This effect would leading to switch on and off condition of the plasmonic resonance, condition observed in Fig. 11(a) to Fig. 11(b); or shift the LSPR from condition observed in Fig. 11(b) to Fig. 11(c). Whichever is the tuning mechanism, this effect could also be translated to other domains, for example the mid infrared domain, where similar effects would be observed.

2.3.4. Experimental demonstration.

To experimentally verify the above theoretical predictions, cavity-coupled plasmonic samples were fabricated following a simple nanotransfer printing technique as we previously reported [110,111]. The process is described in details in Chapter 4. The corresponding SEM images are shown in Fig. 12(a) and Fig. 13(a). Reflectance spectra are measured using a microscope coupled Fourier transform infrared (FTIR) spectrometer (Hyperion 1000 - Vertex 80, Bruker Inc.) for cavity thicknesses L = 610 nm and L = 625 nm, Fig. 12(c) and Fig. 13(c) respectively. In both cases good agreement is observed between FDTD predictions and experimental measurements. Slight deviations

originate from variations in cavity thickness, which is difficult to control via spin processing.

The corresponding FDTD predicted cross-sectional and top view intensity profiles at the strongest resonance points (dashed lines on Fig. 13(c) and Fig. 12(c)) are shown in Fig. 13(b) and Fig. 12(b), respectively. Slanted phase fronts (dashed red lines) inside the cavity of Fig. 12(b)(right) for the diffracting system (P = 740 nm) results from higher diffraction order in the resonating mode. Contrary to this, the diffraction-less system (P = 300 nm) shows the fundamental D_{00} mode as a flat wave front within the cavity, Fig. 12(b)(right).

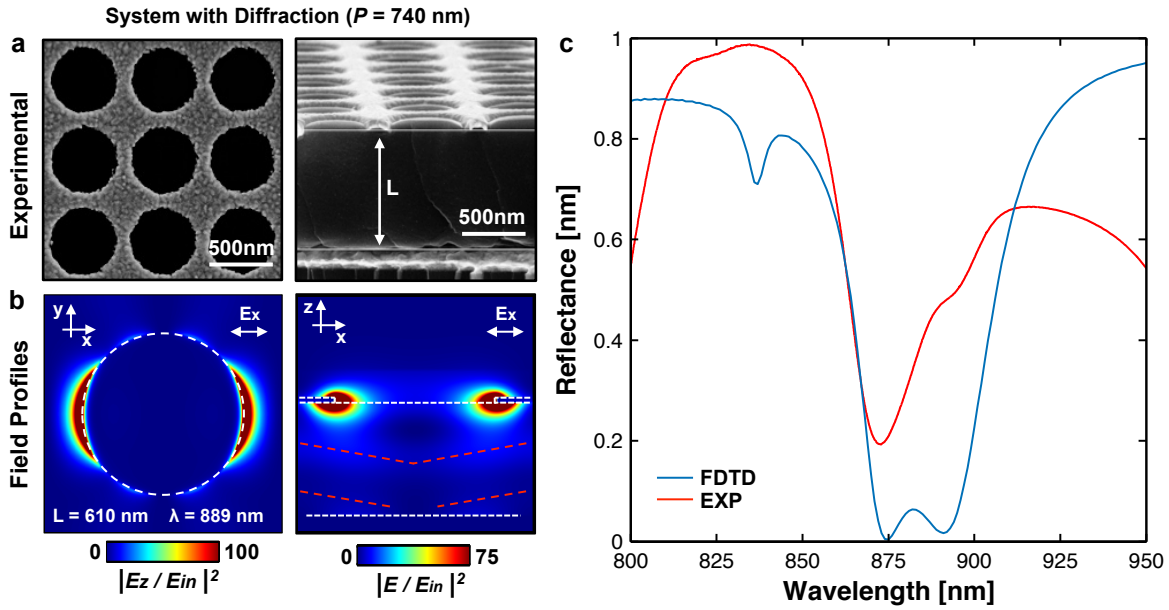

Figure 12: (a) SEM image of one fabricated cavity: top view (left) and cross-sectional view (right). (b) The corresponding spatial field distribution at $\lambda = 889$ nm and $L = 610$ nm: cross-section (right) and top view of the intensity distribution for the real part of E_z component (left). (c) FDTD predicted and experimentally measured reflectance spectrum for cavity thickness $L = 610$ nm for the $P = 740$ nm system.

A photonic cavity interacting with a plasmonic system in diffraction and diffraction-less regimes was studied. In both cases, independent (without diffraction) or combined photonic modes from intra-cavity multiple wave interference (with diffraction) interact with the plasmonic mode based on the cavity phase matching conditions. The thin metallic grating, being a weak absorber

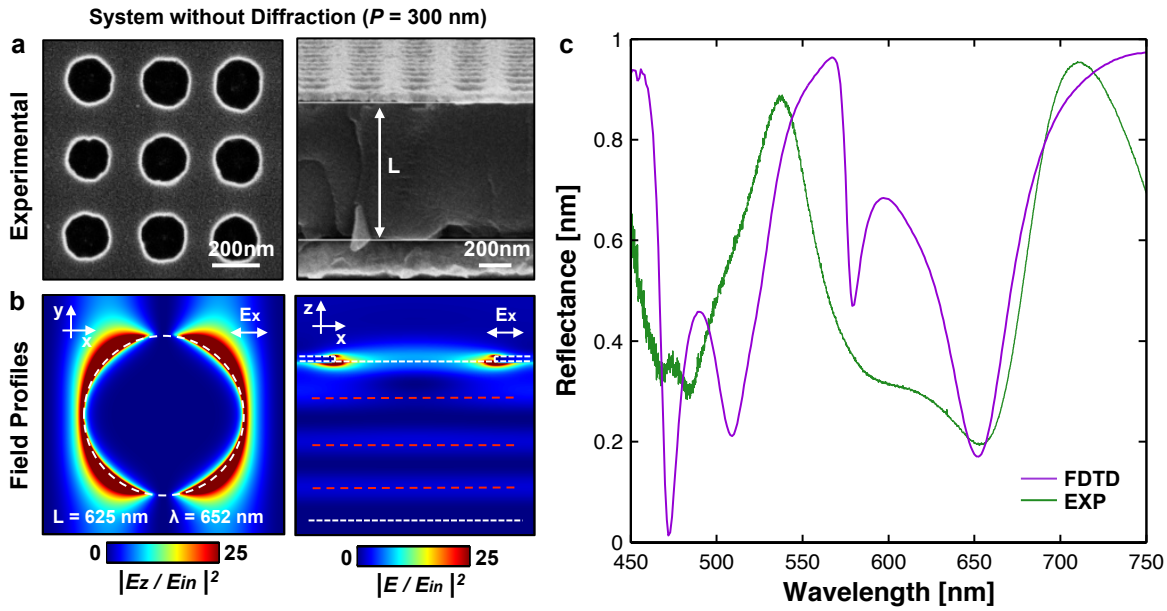

Figure 13: (a) SEM image of one fabricated cavity: top view (left) and cross-sectional view (right). (b) The corresponding spatial field distribution at $\lambda = 652$ nm and $L = 625$ nm: cross-section (right) and top view of the intensity distribution for the real part of E_z component (left). (c) FDTD predicted and experimentally measured reflectance spectrum for cavity thickness $L = 625$ nm for the $P = 300$ nm system.

by itself, can demonstrate strong absorption due to the coherent feedback of the cavity when the electric field creates an antinode at the perforated film. The opposite situation arises and the absorption reduces drastically when the electric field forms a node at the perforated film. Therefore, the LSPR can be enhanced or suppressed in a unique way based on the cavity phase relation.

In this section I presented the first analytical and experimental demonstration of a complex electromagnetic system where not only plasmonic modes but cavity and diffraction orders all interact in space and time and frequency [113]. Consequently, having deeper understanding of the system will allow us to better exploit its properties and land it to interesting and meaningful applications.

3. SUPERCHIRAL LIGHT ON ACHIRAL SUBSTRATES

3.1. Introduction.

Chirality is a ubiquitous property of life found in all biological systems, from fundamental left-handed amino acids to right-handed glucose to the inherent chirality of complex DNA strands and proteins. Present in two enantiometric configurations: left (*sinister*, *s*-) and right (*dexter*, *d*-) [146], chiral molecules have undistinguishable physical properties, such as density, molecular weight or electronic and vibrational transitions frequencies, hence extremely difficult to differentiate with common analytical and spectroscopic techniques. However, it is the interaction with other enantiomers the key to differentiate their intrinsic chiral configuration. For instance, electromagnetic fields carry intrinsic chirality imposed by its polarization states [147]. Circularly polarized light (CPL), either right polarized (RCP) or left polarized (LCP), is a clear example of opposite electromagnetic enantiomers that allow chiral light-matter interaction, for example in optical rotatory dispersion or circular dichroism (CD) spectroscopies [147, 148]. Matter's intrinsic chirality arises from its electromagnetic polarizability; a property imposed by its atomic configuration and proportional to the electromagnetic chiral density [147–149]. However, free propagating electromagnetic fields have an upper limit chiral density whose maximum is that for CPL, thus limiting chiral light-matter interaction.

Recent efforts have been made to produce light fields with chiral density larger than CPL, *superchiral* fields, using specially engineered light fields with the aim to enhance chiral light-matter interaction. One approach is based on macroscopic interference produced by two counter propagating CPL beams of opposite handedness to enhance the absorption rate of chiral molecules placed at the nodes of the standing wave where the electromagnetic chiral density is maximum [148, 150]. The dissymmetry factor observed in the far-field CD is significantly enhanced with respect to CPL excitation. However, the spatial extend of the superchiral field is limited to the

node of the interference pattern where the electric field is weak. Therefore, the overlap between the chiral field and the molecule is extremely small making molecular absorption cross-section low.

Alternative methods employ photonic [151–154] and plasmonic [49, 88–90, 94, 95, 97, 102, 155–163] surfaces to produce superchiral near-fields [89, 91, 92, 97, 98, 100–103, 160, 164]. However, due to geometrical chirality such structures produce strong far-field CD signal that overshadows the weak molecular CD signal produced by the interaction between the chiral near-field and the target chiral molecule. Therefore, the expected signal to noise ration becomes severely affected as the substrate CD noise adds-up with the systems noise. Moreover, it is imperative to obtain pure single-handed chiral near-field in the entire probing volume with simultaneous zero far-field structural CD signal. These mutually exclusive requirements were not accomplished in previous attempts based on macroscopic interferometric superchiral light generation [148, 150], geometrically chiral [49, 89, 92, 97, 100, 160] or achiral [91, 98, 101–103, 159] plasmonic systems.

The scope of this chapter is to understand and manipulate the chiral density of the electromagnetic fields and it's interaction with chiral matter in plasmonic systems. In this regards, first the chiral density of electromagnetic fields is introduced for an arbitrary free-propagating plane wave. Then, the I demonstrate a novel physical mechanism to generate single-handed superchiral near-field based on an electromagnetic dipole model. This model stands as a simple and representative electromagnetic testing playground to study plasmonic systems resonating at its fundamental dipole approximation limit. Under this premises, single-handed superchiral near-field is obtained on an achiral cavity-coupled plasmonic system, as previously introduced. The main finding in this section is the flexibility to generate these type of fields with such a unique property based on degenerate and spatially superimposed plasmonic resonances [96]. I found that it is the spatiotemporal and not the spatial distribution of the near field the actual source of single-handed chiral near-field. Such a performance is broken when the resonant system become asymmetric.

3.2. Chirality of the electromagnetic field.

In 1964 Lipkin introduced the conserved quantity [147], a time-even and parity-odd pseudo vector, whose time average value is

$$C(\mathbf{r}) = \left\langle \frac{\varepsilon_0}{2}\tilde{\mathbf{E}}\cdot\nabla\times\tilde{\mathbf{E}} + \frac{1}{2\mu_0}\tilde{\mathbf{B}}\cdot\nabla\times\tilde{\mathbf{B}} \right\rangle = -\tfrac{1}{2}\varepsilon_0 \mathrm{Im}\left(\mathbf{E}^*\cdot\mathbf{B}\right), \tag{16}$$

where $\mathbf{E}$ and $\mathbf{B}$ are the complex time varying electric and magnetic field vectors, $\tilde{\mathbf{E}}$ and $\tilde{\mathbf{B}}$ are the real parts, respectively, $\mathbf{r}$ is the position vector, ε_0 is the vacuum permittivity and $\langle\rangle$ represents time average. In order to keep notation clean the time dependence is left implicit. Derivation of Eq. 16 is found in Appendix A.1. Although it lacked a physical observable at that time, it was until recently that it was attributed to the electromagnetic chiral density and observable through chiral light-matter interactions [148, 150], and directly related to the spin angular momentum and helicity of light [165–167]. As stated by Eq. 16, it is the collinear configuration with non zero phase difference between the electric and magnetic fields, defined by Maxwell's equations, that produces a finite value of chiral density.

Consider for example a backward propagating plane wave described by the electric field vector, propagation vector $\mathbf{k} = -k\hat{z}$ and the magnetic field $\mathbf{B}$ obtained through Maxwell's equation:

$$\mathbf{E} = \frac{1}{\sqrt{2}}E_0\left(\hat{x} + e^{i\Delta\phi}\hat{y}\right)e^{-i(\omega t - \mathbf{k}\cdot\mathbf{r})},$$
$$\mathbf{B} = \frac{\mathbf{k}\times\mathbf{E}}{\omega} = -\frac{k}{\sqrt{2}\omega}E_0(-e^{i\Delta\phi}\hat{x} + \hat{y})e^{-i(\omega t - \mathbf{k}\cdot\mathbf{r})},$$

where k is the free space wave vector, E_0 is the electric field magnitude and $\Delta\phi$ is the phase between the superposition of two orthogonal field, and which will determine the polarization state. Solving Eq. 16 for this arbitrary field it is obtained

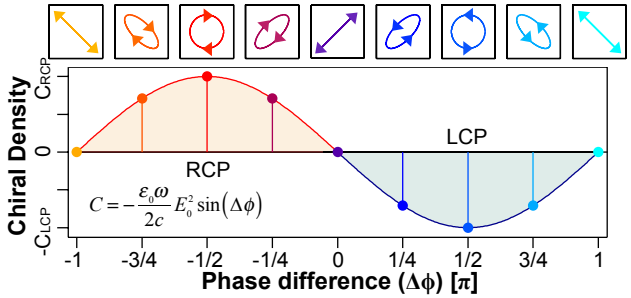

Figure 14: Chiral density of a planewave with an arbitrary polarization state, given by $\Delta\phi$ propagating along the $-z$ direction (into the paper).

$$C = \frac{\varepsilon_0 \omega}{4c} E_0^2 \,\mathrm{Im}\left([\hat{x} + e^{i\Delta\phi}\hat{y}]^* \cdot [\,-e^{i\Delta\phi}\hat{x} + \hat{y}] \right) = \frac{\varepsilon_0 \omega}{4c} E_0^2 \,\mathrm{Im}\left(-e^{i\Delta\phi} + e^{-i\Delta\phi} \right)$$
$$C = \frac{\varepsilon_0 \omega}{4c} E_0^2 \,\mathrm{Im}\left(-i2\sin(\Delta\phi) \right),$$

which reduces to the following simple expression:

$$C = -\frac{\varepsilon_0 \omega}{2c} E_0^2 \sin(\Delta\phi), \tag{17}$$

where c is the speed of light in vacuum, and plotted in Fig. 14. It is clearly evident that a linearly polarized (LP) plane wave ($\Delta\phi = 0$) does not carry chiral density since the transverse $\mathbf{E}$ and $\mathbf{B}$ fields are always orthogonal. This is not the scenario for CPL whose chiral density is

$$C_{\mathrm{CPL}} = - \pm \frac{\varepsilon_0 \omega}{2c} E_0^2 \Big|_{\mathbf{k}=-k\hat{z}}, \tag{18}$$

where $C_{\mathrm{CPL}} < 0$ corresponds to LCP ($\Delta\phi = +\pi/2$) and $C_{\mathrm{CPL}} > 0$ corresponds to RCP ($\Delta\phi = -\pi/2$). Any arbitrary polarization state will render smaller chiral densities than CPL, yet retaining the corresponding helicity as observed in Fig. 14. This is reflected in elliptically polarized light as seen in Fig. 14, where the handedness is maintained but with lower chiral density. The sign

notation $-\pm$ is left in Eq. 18 so that it is straightforward to identify, as it will become more evident in the coming sections, the source of chiral sign.

If the propagation direction flips to forward propagation $\mathbf{k} = k\hat{z}$, so it does the chiral density relation to

$$C_{\text{CPL}} = \pm\frac{\varepsilon_0\omega}{2c}E_0^2\Big|_{\mathbf{k}=+k\hat{z}}. \tag{19}$$

However, the total chiral density sign will remain consistent depending only on the handedness of the electromagnetic field.

3.3. Rotating dipole model.

The oscillating dipole model is a simple playground that captures the fundamental physics in many observed phenomena. It provides an insightful description of matter upon excitation with an electromagnetic field. Hence, it has been the preferred model to test a myriad of physical theories. In our study, this basic electromagnetic unit is used to phenomenologically describe the modal behavior of our plasmonic system and gain further understanding on the fundamental physics. In fact, as the excitation wavelength becomes larger than the plasmonic physical dimension, approaching the quasi-static limit, say length/width in case of nanorods or diameter in case of spheres, disks or holes, the plasmonic excitation at resonance resembles that of an oscillating dipole. For example, Fig. 15 shows the out-of-plane electric field of a plasmonic resonance (left) and point dipole (right). Qualitatively this approach can provide valuable information of the system under study but lacks quantitive accuracy as further considerations need to be address such as real material polarizability, multipolar expansions, near-field and far-field coupling and so on.

For plasmonic systems in particular there is a slight difference between a dipole model formalism. At resonance the scattered near-field can surpass that of the incident field. Depending on the system's configuration this field can even be two to three order of magnitude larger. This condition can apply to both the electric and magnetic fields; however, in most scenarios it the electric

field enhancement the one that is larger that the magnetic field enhancement. Due to this fundamental difference in localized plasmon excitations the dipole model here presented includes a field enhancement factor ξ in the magnetic field. Therefore, if the plasmonic resonance is dominated by el electric field $\xi < 1$ and if it is dominated by the magnetic field it would be $\xi > 1$.

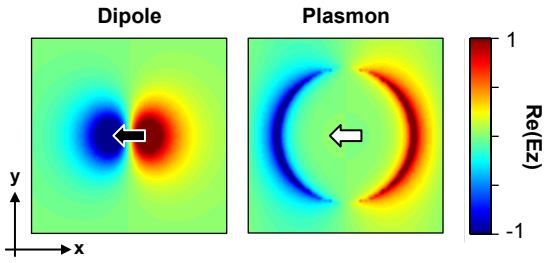

Figure 15: Comparison of an electromagnetic point dipole and the plasmonic excitation of a nano hole, which shows the out-of-plane electric field $\mathrm{Re}(E_z)$.

3.3.1. Stand-alone dipole.

An arbitrary harmonic dipole oscillating at angular frequency ω is physically modeled as

$$\tilde{\mathbf{p}} = p_0 \hat{\mathbf{p}} e^{-i\omega t}, \tag{20}$$

where p_0 is the dipole moment magnitude and $\hat{\mathbf{p}}$ is the dipole moment orientation vector. The corresponding electric and magnetic fields associated with this dipole are [26]:

$$\mathbf{E}_{RD}(\mathbf{r},t) = \frac{1}{4\pi\varepsilon_0}\frac{e^{ikr}}{r^3}\left\{k^2 r^2(\mathbf{n}\times\tilde{\mathbf{p}})\times\mathbf{n} + \Big[3\mathbf{n}(\mathbf{n}\cdot\tilde{\mathbf{p}}) - \tilde{\mathbf{p}}\Big](1-ikr)\right\}, \tag{21}$$

and

$$\mathbf{B}_{RD}(\mathbf{r},t) = \xi\frac{c\mu_0 k^2}{4\pi}\frac{e^{ikr}}{r}(\mathbf{n}\times\tilde{\mathbf{p}})\Big(1-\frac{1}{ikr}\Big). \tag{22}$$

Here $\mathbf{n}$ is the unit vector and $\mathbf{r}$ is the position vector with magnitude r. As previously discussed, Eq. 22 contains the factor ξ. Although here it does not play a role in the final result it will be of great importance in the coming sections. Solving Eq. 16 for this set of vector fields we obtain that the spatial dependence of the RD chiral density is

$$C_{\mathrm{RD}}(\mathbf{r}) = -\frac{\varepsilon_0\omega}{2}\left(\frac{k}{4\pi\varepsilon_0}\right)^2\frac{1}{cr^5}\,\mathrm{Im}\left[\left\{k^2\left[(\mathbf{r}\times\tilde{\mathbf{p}}^*)\times\mathbf{r}\right]\cdot(\mathbf{r}\times\tilde{\mathbf{p}}) + \left[\frac{3}{r^2}\mathbf{r}(\mathbf{r}\cdot\tilde{\mathbf{p}})-\tilde{\mathbf{p}}^*\right]\cdot(\mathbf{r}\times\tilde{\mathbf{p}})(1+ikr)\right\}\left(1-\frac{1}{ikr}\right)\right]. \tag{23}$$

It is straightforward to demonstrate algebraically that the $\mathbf{r}$ and $\tilde{\mathbf{p}}$ vector operations in Eq. 23 can be reduced to the following determinant form:

$$\left[(\mathbf{r}\times\hat{\mathbf{p}}^*)\times\mathbf{r}\right]\cdot(\mathbf{r}\times\hat{\mathbf{p}}) = (\mathbf{r}\cdot\mathbf{r})\det(\mathbf{r},\hat{\mathbf{p}},\hat{\mathbf{p}}^*) - (\hat{\mathbf{p}}\cdot\mathbf{r})\det(\mathbf{r},\hat{\mathbf{p}},\mathbf{r}) = r^2\det(\mathbf{r},\hat{\mathbf{p}},\hat{\mathbf{p}}^*) \tag{24a}$$

$$\hat{\mathbf{p}}^*\cdot(\mathbf{r}\times\hat{\mathbf{p}}) = \det(\hat{\mathbf{p}}^*,\mathbf{r},\hat{\mathbf{p}}) \tag{24b}$$

$$\mathbf{r}(\mathbf{r}\cdot\hat{\mathbf{p}}^*)\cdot(\mathbf{r}\times\hat{\mathbf{p}}) = 0 \tag{24c}$$

where $\det(\mathbf{r},\hat{\mathbf{p}},\mathbf{r}) = 0$ for any configuration of $\hat{\mathbf{p}}$ and $\mathbf{r}(\mathbf{r}\cdot\hat{\mathbf{p}}^*)\cdot(\mathbf{r}\times\hat{\mathbf{p}}) = 0$ as it is equivalent of a dot product of two orthogonal vectors. Employing this formalism, a rotating dipole (RD) is modeled using the superposition of two orthogonal oscillating dipoles with a phase difference of $\Delta\phi = \pm\pi/2$; however, it is just a particular condition of an arbitrary superposition of two orthogonal dipoles with a phase difference of $\Delta\phi$. The dipole moment for a dipole oscillating in the xy plane at $z = 0$ is given by:

$$\tilde{\mathbf{p}} = p_0\left(\hat{x} + e^{i\Delta\phi}\hat{y}\right)e^{-i\omega t}. \tag{25}$$

A right-RD corresponds to a phase difference of $+\pi/2$, whereas a left-RD corresponds to a phase difference of $-\pi/2$. The convention used to determine the dipole rotation direction is discussed in

the rotation convention section 3.3.3. Using Eq. 25, Eq. 24a and Eq. 24b become

$$\Big[(\mathbf{r}\times\hat{\mathbf{p}}^*)\times\mathbf{r}\Big]\cdot(\mathbf{r}\times\hat{\mathbf{p}}) = \frac{r^2}{2}\begin{vmatrix} x & y & z \\ 1 & e^{i\Delta\phi} & 0 \\ 1 & e^{-i\Delta\phi} & 0 \end{vmatrix} = -ir^2 z\sin(\Delta\phi),$$

$$\hat{\mathbf{p}}^*\cdot(\mathbf{r}\times\hat{\mathbf{p}}) = \frac{1}{2}\begin{vmatrix} 1 & e^{-i\Delta\phi} & 0 \\ x & y & z \\ 1 & e^{i\Delta\phi} & 0 \end{vmatrix} = -iz\sin(\Delta\phi),$$

which plugged into Eq. 23 the electromagnetic chiral density produced by this rotating dipole becomes

$$C_{\text{RD}}(\mathbf{r}) = \frac{\varepsilon_0\omega}{2cr^5}\left(\frac{p_0 k}{4\pi\varepsilon_0}\right)^2 \text{Im}\left[\left\{k^2(-ir^2 z\sin(\Delta\phi)) - (-iz\sin(\Delta\phi))(1+ikr)\right\}\left(1-\frac{1}{ikr}\right)\right].$$

The vector operations expressed in a determinant form are demonstrated in Appendix A.3. Finally, after further performing the corresponding algebra, the spatial distribution of the electromagnetic chiral density produced by this RD model is reduced to the following simple expression.

$$C_{\text{RD}}(\mathbf{r}) = C_{RD0}\sin(\Delta\phi)\frac{z}{r^3} \tag{26}$$

were C_{RD0} is a scale factor given by the dipole electromagnetic parameters. The spatial distribution for left and right RD, as described by Eq. 26 is plotted in Fig. 16. From this result we can make four important observations:

- The electromagnetic chiral density is confined in the near field: $\frac{1}{r^2}$.
- The electromagnetic chiral density generated by a linear oscillating dipole ($\Delta\phi = 0$) is zero: $\sin(0) = 0$.

- For a fixed stratum, say $z > 0$, and rotation direction the electromagnetic chiral density has same sign: $\frac{1}{r^3} > 0$.

- For a fixed stratum, say $z > 0$, the electromagnetic chiral density sign reverses uniquely by flipping the rotation direction of the dipole $\Delta\phi$.

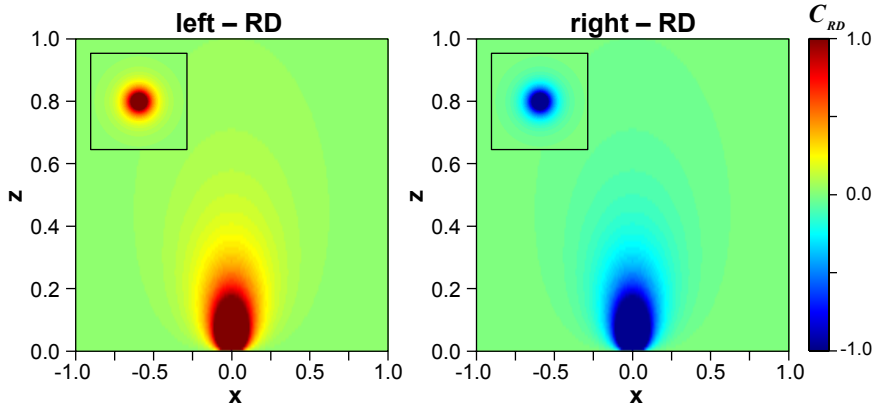

Figure 16: Chiral near field distribution for a left-RD and right-RD given by Eq. 26. As observed, a left-RD dipole generates a single sign chiral near field in semi-infinite domain given by $z > 0$ and reverse sign by only reversing its rotation direction.

3.3.2. Dipole excitation with circularly polarized light.

In a real scenario the dipole excitation is only a result of matter polarizability and radiation based on an external stimulation, such as incident electromagnetic field; given by $\mathbf{E}_i$ and $\mathbf{B}_i$ fields. Furthermore, as the dipole oscillation is the result of the incident electromagnetic excitaiton the dipole moment is now

$$\tilde{\mathbf{p}} = i\frac{1}{\sqrt{2}}\alpha_0 E_0(\hat{x} + e^{i\Delta\phi})e^{-i\omega t}. \tag{27}$$

In this representation the factor i is added to account for excitation of an arbitrary dipole at resonance and α_0 is the dipole polarizability. The total chiral near-field generation produced by the

oscillating dipole must contain the contribution from the incident field as well. In this extent the total field around the dipole are

$$\mathbf{E}_T = \mathbf{E}_i + \mathbf{E}_{\text{RD}} \tag{28a}$$

$$\mathbf{B}_T = \mathbf{B}_i + \mathbf{B}_{\text{RD}}. \tag{28b}$$

Solving Eq. 16 the total chiral density is

$$C_{\text{T}}(\mathbf{r}) = \frac{1}{2}\varepsilon_0 \,\text{Im}\left([\mathbf{E}_i + \mathbf{E}_{\text{RD}}]^* \cdot [\mathbf{B}_i + \mathbf{B}_{\text{RD}}]\right) = C_i + C_{\mathbf{E}0-\mathbf{B}\text{RD}} + C_{\mathbf{E}\text{RD}-\mathbf{B}0} + C_{\text{RD}}.$$

As demonstrated by the previous expression the contribution to the total chiral density, C_{T}, originates from four different sources: the incident field (C_i) and RD (C_{RD}), as previously described in Eq. 17 and Eq. 26, respecteively; and the interaction from the incident electric field with the dipole-generated magnetic field ($C_{\mathbf{E}i-\mathbf{B}\text{RD}}$) and the interaction of the dipole-generated electric field with the incident magnetic field ($C_{\mathbf{E}\text{RD}-\mathbf{B}i}$). The calculation details are listed in Appendix A.2. The total chiral density for ($C_{\mathbf{E}i-\mathbf{B}\text{RD}}$) and ($C_{\mathbf{E}\text{RD}-\mathbf{B}i}$), for a backward propagating plane wave, $\mathbf{k} = -k\hat{z}$, are listed below.

$$C_i(\mathbf{r}) = C_0 \sin(\Delta\phi) \tag{29a}$$

$$C_{\mathbf{E}i-\mathbf{B}\text{RD}}(\mathbf{r}) = C_0 \xi\kappa \frac{z}{r^3} \sin(\Delta\phi) \tag{29b}$$

$$C_{\mathbf{E}\text{RD}-\mathbf{B}i}(\mathbf{r}) = C_0\kappa\frac{1}{2r^3}\left[\left(k - \frac{3}{kr^2}\right)(x^2 - y^2)\right)\cos(\Delta\phi) + \left(\frac{3}{r}(x^2+y^2) - 2r\right)\sin(\Delta\phi)\right] \tag{29c}$$

$$C_{\text{RD}}(\mathbf{r}) = -C_0\xi k^2\kappa^2\frac{z}{r^3}\sin(\Delta\phi) \tag{29d}$$

In this set of equations the term $C_0 = -\varepsilon_0\omega E_0^2/2c$ stands for the magnitude of the chiral density of a LCP plane wave, $\kappa = \alpha_0 k/4\pi\varepsilon_0$ is the normalized dipole polarizability and α_0 is the dipole

polarizability. Finally, the total chiral density as a function of incident polarization is:

$$C_T(\mathbf{r},\Delta\phi) = C_0\left\{1+\frac{\kappa}{r^3}\left[\xi z+\frac{1}{2r}\left(r^2-3z^2\right)-\xi k^2\kappa z\right]\right\}\sin\left(\Delta\phi\right) - C_0\frac{\kappa}{2r^3}\left(k-\frac{3}{kr^2}\right)(x^2-y^2)\cos\left(\Delta\phi\right), \tag{30}$$

This more complex result confirms the previous fundamental observations in which the total chiral density is influenced by the incident polarization. Nevertheless, it is implied that LP light does generate finite chiral density as $\cos\left(\Delta\phi\right)=1$ in contrast to LP or a linear dipole alone, which comes from the contribution of the incident magnetic field and the electric field generated by the RD. Now, considering LCP ($\Delta\phi=+\pi/2$) Eq. 30 becomes

$$C_T(\mathbf{r}) = C_0\left\{1+\frac{\kappa}{r^3}\left[\xi z+\frac{1}{2r}\left(r^2-3z^2\right)-\xi k^2\kappa z\right]\right\}. \tag{31}$$

It is clear that for a weak dipole polarizability, $\kappa \ll 1/r^3$, the total chiral density distribution converges to only that of the incident light. This condition is satisfied, for example in a polarizable element off-resonance. However, for a finite polarizability and magnetic field enhancement the total chiral near-field spatial distribution is severely perturbed. In order to perform a comprehensive analysis we take Eq. 31 and observe at $(x,y)=0$, $r=z$ and $z>0$, plotted in Fig. 17(a) as function of κ and ξ. According to Eq. 31 the chiral density right above the dipole can be zero for a specific set of parameters (κ,ξ). This condition can be obtained by solving Eq. 31.

$$\xi_{th} = \frac{1-\kappa^{-1}r^2}{1-k^2\kappa} \tag{32}$$

This condition states that for a certain polarizability (κ) $C_{\mathrm{T}}<0$ if $\xi>\xi_{th}$ and $C_{\mathrm{T}}>0$ if $\xi<\xi_{th}$. Such a condition is plotted in Fig. 17(a) as a green line. It also determines the nature of

the total chiral density. If $\xi > \xi_{th}$ the dipole magnetic field dominates ($C_{\mathbf{E}CPL-\mathbf{B}RD}$), and if

$$\xi > \frac{1}{1-k^2\kappa}, \tag{33}$$

the total near-field becomes superchiral, blue line in Fig. 17(a).

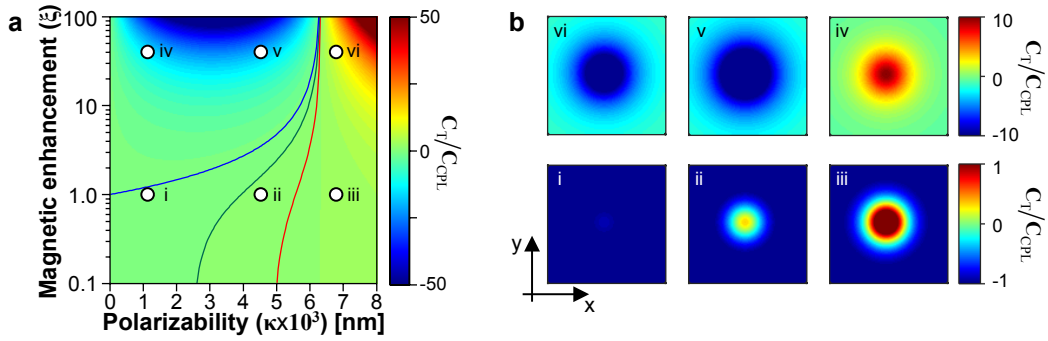

Figure 17: (a) Near field chiral density at $(x, y) = 0$ and $z = 50$ nm produced by the incident and excited dipole fields. The incident field is LCP, propagating in the $-z$ direction with $C < 0$. The green curve represents the threshold line at which the generated near field flips chiral density sign with respect to the incident field. The blue/red dashed line represents the condition at which the chiral density is larger than that of CPL with same/opposite chiral sign as the incident field. (b) Chiral field in the xy plane at $z = 50$ nm for different conditions of (κ, ξ): i $(1.1 \times 10^3, 1)$, ii $(4.5 \times 10^3, 1)$, iii $(6.7 \times 10^3, 1)$, iv $(1.1 \times 10^3, 40)$, v $(4.5 \times 10^3, 40)$, vi $(6.7 \times 10^3, 40)$.

On the other hand, if $\xi < \xi_{th}$ the dipole electric field dominates ($C_{\mathbf{E}RD-\mathbf{B}CPL}$) reversing the chiral density sign with respect to the incident field with superchiral light generation condition when

$$\xi < \frac{1-2\kappa^{-1}r^2}{1-k^2\kappa} \tag{34}$$

as plotted in Fig. 17(a) red line and holds true independently of the magnetic field enhancement factor after $\kappa > k^2$, which corresponds to the asymptotic limit. The compilation of such a set of conditions are plotted in Fig. 17(b). For instance, the total chirality of a weakly excited dipole is dominated by free space chirality with a small perturbation at the center as observed in Fig.

17(b)(i). If the polarizability increases the contribution from the RD is opposite as the incident field, Fig. 17(b)(ii, iii). On the other hand, for a larger magnetic field enhancement the net chirality is preferentially dominated by the RD with same chirality as that of free space, Fig. 17(b)(iv, v). Nevertheless, it reverses as the polarizability surpasses the condition imposed by $\kappa > k^2$, Fig. 17(b)(vi).

3.3.3. Rotation convention.

In order to remain consistent with the rotation convention for the incident free space electromagnetic field the polarization state is determined by the right-hand rule convention, $\hat{x} \times \hat{y} = \hat{z}$, where the thumb points in the direction of propagation and the time evolution of the polarization plane at $z = z_0$ is given by the curl of the four-fingers. Therefore, a forward propagating wave given by the electric field vector $\mathbf{E} = \frac{1}{\sqrt{2}} E_0 \left(\hat{x} + e^{i\Delta\phi}\hat{y}\right) e^{-i(\omega t - \mathbf{k}\cdot\mathbf{r})}$ with $\mathbf{k} = k\hat{z}$ is LCP if $\Delta\phi = -\pi/2$ and RCP if $\Delta\phi = +\pi/2$. On the other hand, for a backward propagating wave $\mathbf{k} = -k\hat{z}$ it becomes LCP if $\Delta\phi = +\pi/2$ and RCP if $\Delta\phi = -\pi/2$.

The rotation convention for an electric dipole is given by Eq. 25: $\tilde{\mathbf{p}} = p_0 \left(\hat{x} + e^{i\Delta\phi}\hat{y}\right) e^{-i\omega t}$. The instantaneous dipole moment orientation, whose time evolution dictates the rotation direction, is determined by the phase difference between the superposition of both orthogonal dipole moments, same as that for CPL. However, the rotation direction could become ambiguous as there is not a propagation direction, which was a reference point in determining the rotation handedness in CPL. Following the same right-hand rule, $\hat{x} \times \hat{y} = \hat{z}$, the thumb points towards the $\hat{z}$ direction and the four finger curl determines the rotation direction. Therefore, a right-rotating dipole corresponds to $\Delta\phi = +\pi/2$ while $\Delta\phi = -\pi/2$ determines a left-rotating dipole.

Both CPL and RD rotation convetions are summarized in Table 1 along with the corresponding chiral density of the corresponding fields as seen in Fig. 14 and Fig. 16. It is worth noticing that when the RD is the result of the excitation with free-space then RCP does not mean it would excite a right rotating dipole but a left rotating dipole, and viceversa for LCP. It is because,

phenomenologically, the local dipole will follow instantaneous polarization plane of the incident wave. This interaction is shown in Fig. 18.

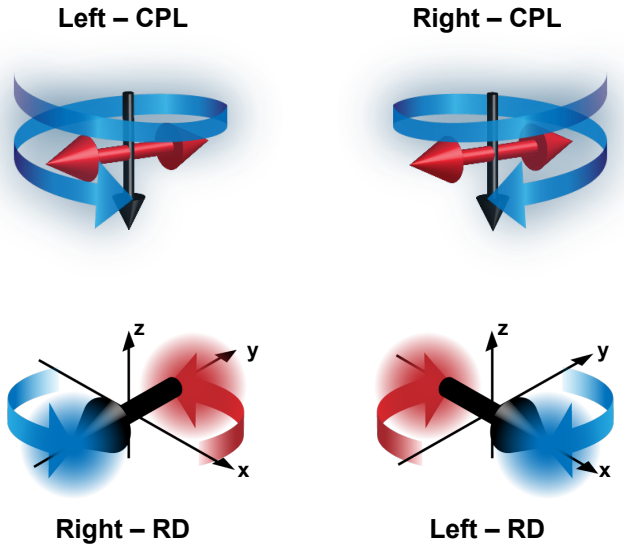

Figure 18: Graphical representation of a dipole excited with CPL. The linear dipole will follow the instantaneous polarization plane, hence LCP excited the Right-RD and viceversa .

Table 1: Convetion adopted to define CPL handedness depending on the propagation direction and phase difference. *Eq. 26, †Eq. 18 and ‡Eq. 19

$\Delta\phi$	RD	C_{RD} $z > 0^{\star}$	Light @ $\mathbf{k} = k\hat{z}^{\dagger}$		Light @ $\mathbf{k} = -k\hat{z}^{\ddagger}$	
$-\pi/2$	Left RD	$C < 0$	LCP	$C < 0$	RCP	$C > 0$
0	Linear	$C = 0$	LP	$C = 0$	LP	$C = 0$
$+\pi/2$	Right RD	$C > 0$	LRP	$C > 0$	LCP	$C < 0$

3.4. Plasmonic systems and superchiral light generation.

3.4.1. Degenerate achiral systems.

As demonstrated in the previous section it is the temporal distribution of the resonance and not its spatial distribution that gives rise to the generation of single-sign superchiral near field. Such unique phenomenon is demonstrated in a totally achiral plasmonic system that is coupled to a photonic cavity. The achiral plasmonic substrate is illustrated in Fig. 19, which is comprised of a symmetric nanostructured gold square lattice hole-disk pattern ($P = 740$ nm, $D = 480$ nm, hole-disc separation $= 350$ nm and gold film thickness $= 30$ nm) coupled with an asymmetric Fabry-Perot cavity. The cavity is formed with a gold back reflector separating the two-element plasmonic pattern with cavity thickness (L) determined by the dielectric film.

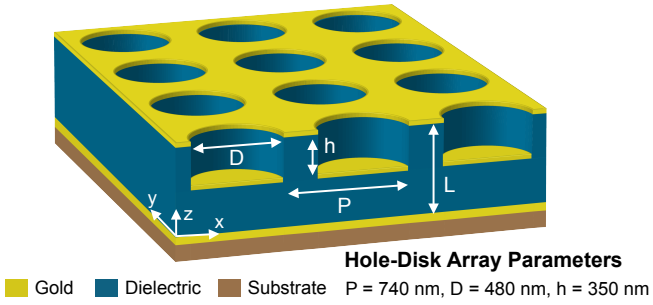

Figure 19: Schematic representation of the cavity-coupled achiral plasmonic systems comprised of a square array of hole-disk on an asymmetric Fabry-Perot cavity.

The first step in studying and understand the performance of this coupled system I performed finite difference time domain (FDTD) simulations for LP light. The dielectric parameter for gold is taken from experimental measured data, Palik [145] and the dielectric layer refractive index is 1.56. One unit cell is employed in the simulations. Periodic boundary conditions are set on the x and y boundaries and perfect matching layer on the z boundaries. The excitation direction is backward, i.e. along the $-z$ direction. With excitation polarization is along the x direction,

which corresponds to one of the symmetric lattice's axes, the cavity thickness (L) is changed and the absorption spectra are extracted.

The cavity-coupled system has two interaction domains. One is in the 9700-7000 cm^{-1} frequency band,where the hole-disk system supports natural localized surface plasmon (LSP) modes induced solely by the geometrical parameters of the hole-disk system: diameter, periodicity and hole-disk separation. In this band hybrid resonance modes are observed as absorption frequency splitting around the LSP absorption band due to the coherent interaction between cavity and plasmonic modes as studied in Chapter 2 [113].

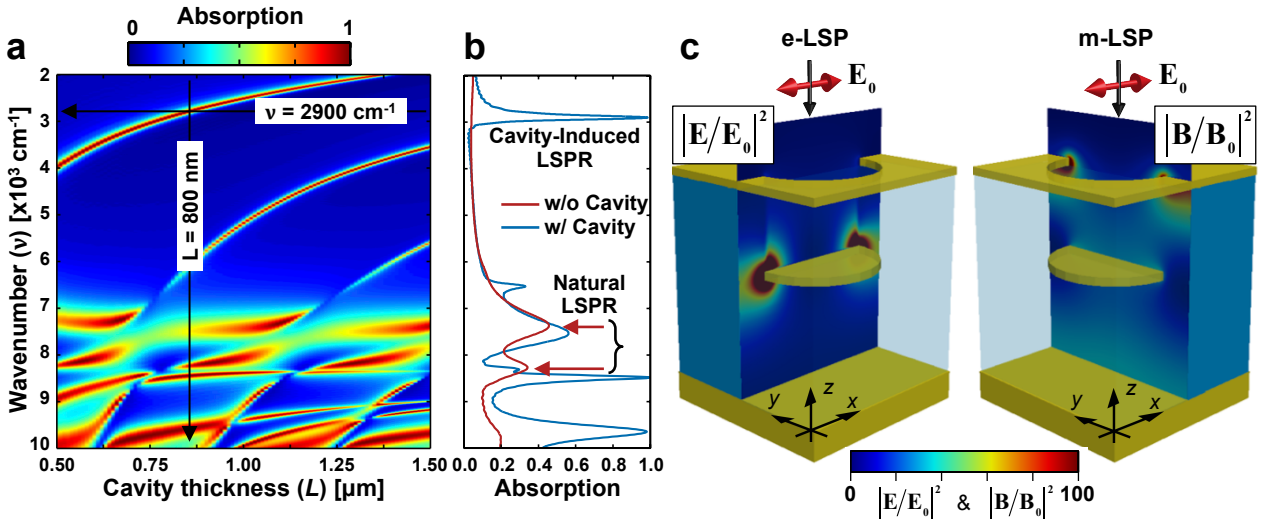

Figure 20: (a) Absorption dispersion as a function of cavity thickness for normal excitation with linearly polarized light. (b) Absorption spectra of the coupled system for a cavity thickness of L = 800 nm and comparison with a flat 2D array without the electromagnetic feedback. The cavity-coupled plasmonic substrate is a 2D symmetric square array of hole with period of 740 nm, diameter of 480 nm and hole depth of 350 nm. (c) Electric (left) and magnetic (right) intensity cross-section at the center of the unit cell for L = 800 nm and ν = 2900 cm^{-1} showing an electric and magnetic LSP resonance, respectively.

A second, yet more interesting, interaction occurs when the cavity resonates away from the natural LSP band of the top plasmonic pattern. Figure 20(a) shows the absorption dispersion for LP light along the x direction. The photonic resonance, for fixed nanostructure parameters,

depends strictly on the propagation phase imposed by the cavity ($n_d kL$), where n_d is the refractive index of the dielectric spacer. Although, adding a cavity enhances the LSP mode at the natural LSP band compared to its uncoupled counterpart [113], the excitation of LSP modes at lower energies is possible when placing a polarizable element inside the cavity, based on quantum cavity electrodynamics [168], as observed in the absorption spectra in Fig. 20(b). At the fundamental photonic resonant mode the electric field antinodes are located around the optical center of the cavity where the disk is placed, while strong magnetic field antinodes are located at the edges of the cavity, *i.e.* the back reflector and the top hole array. As a result, the cavity selectively polarizes the hole-disk system inducing electric/magnetic LSP modes (e-LSP/m-LSP) on the disc/hole as observed in Fig. 21(c).

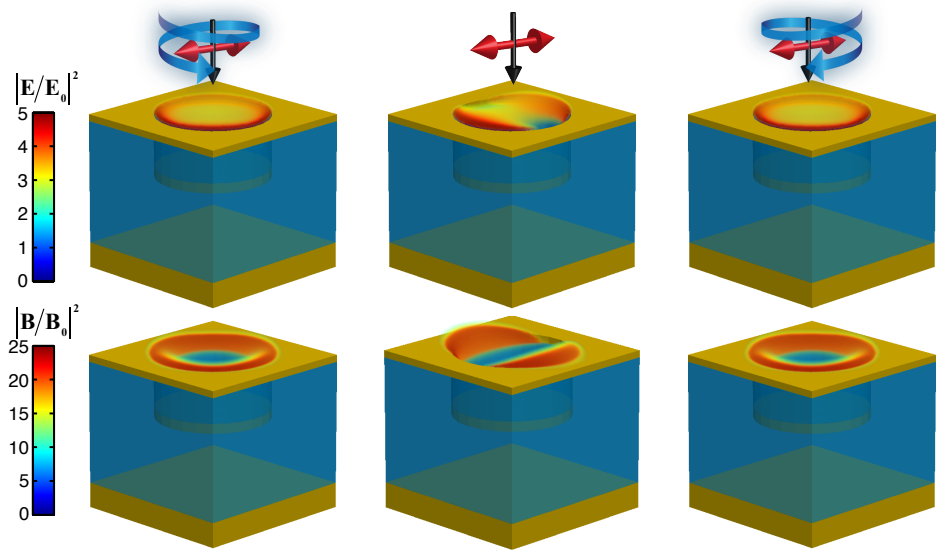

Figure 21: (top row) Electric field and (bottom row) magnetic field volumetric intensity representations at resonance (L = 800 nm and ν = 2900 cm^{-1}) for linear excitation at (left) LCP, (center) LP, and (right) RCP.

The symmetric achiral system supports two degenerate LSP resonances along each of the lattice axes. Upon illumination with CPL both LSP modes are excited simultaneously with a phase difference imposed by the excitation source. Concomitantly an effective rotating dipole is

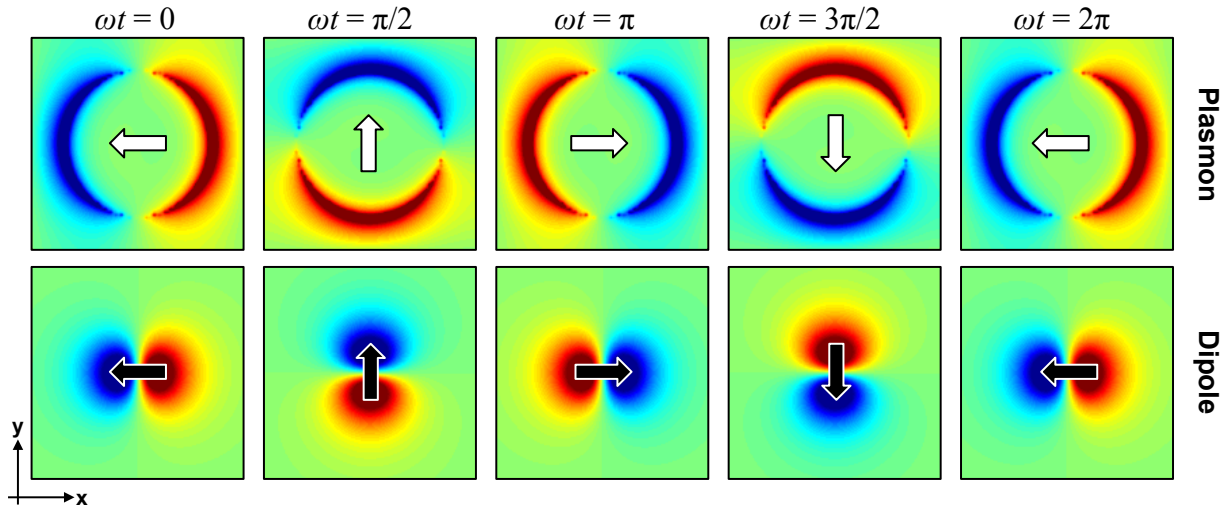

Figure 22: Instantaneous electric field (E_z) distribution in the xy plane for a left rotating plasmon mode (top row) when excited with RCP and a left rotating dipole (bottom row). Snapshot taken in one optical cycle in ωt increments of $\pi/2$.

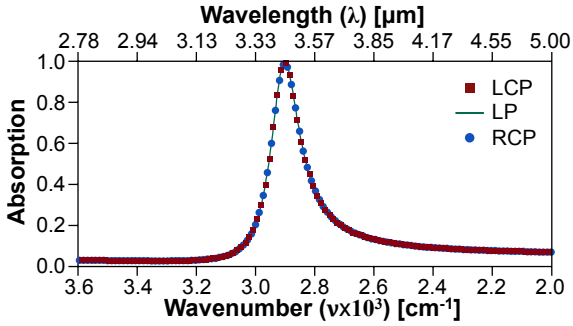

Figure 23: Simulated absorption spectra for the achiral cavity-coupled plasmonic systems when excited with LP (green), LCP (red squares) and RCP (blue circles).

generated on the top hole. This behavior is observed in Fig. 22 where the time snapshots of the out-of-plane electric field in one optical cycle are plotted for this LSP and dipole when excited with RCP. As observed in Fig. 21 both, electric and magnetic field intensity distributions are exactly the same when excited either by LCP or RCP, without any dissymmetry in the absorption spectrum, see Fig. 23. However, the chiral near-field density generated by this system is remarkably different.

As observed in Fig. 24(left) and Fig. 24(right), the near-field chiral density has same handedness as the incident light which fully reverses when flipping the incident CPL excitation on the same geometry.

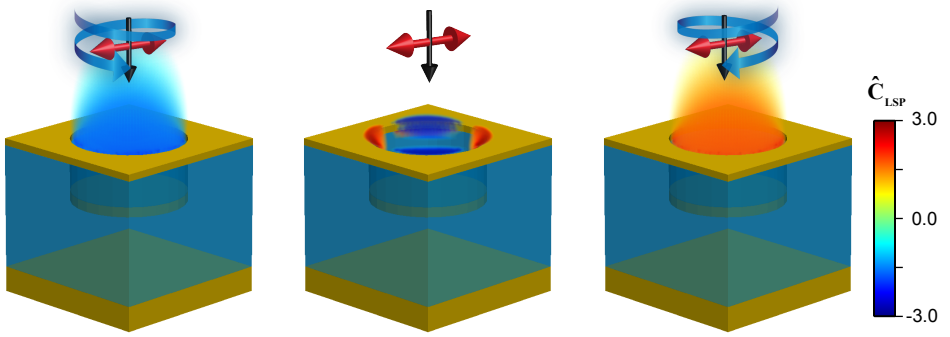

Figure 24: Free space normalized chiral density of the LSP near field when excited with LCP (left), LP (center) and RCP (right).

The generated chiral density purity is obtained by performing volume integration on the numerically calculated freespace-normalized chiral density $C_{\text{LSP}}(\mathbf{r}, \nu)$ in the upper half-space of the unit cell using the following equation:

$$\hat{C}(\nu) = \frac{1}{V_{uc}} \int_{uc} C_{\text{LSP}}(\mathbf{r}, \nu) dV, \tag{35}$$

where V_{uc} is the total volume exposed in the upper space, and uc stands for the unit cell. As observed in Fig. 25 the integrated chiral density peaks right at the plasmonic resonance, $\nu = 2900$ cm^{-1} and is negative for LCP and positive for RCP.

Furthermore, spectral integration in the upper half-space of the unit cell at resonance reveals 99.96% of the near-field has CPL-like chiral density and only 0.04% has the opposite helicity across the entire LSPR band, which can be attributed to numerical artifacts. This is not the case for LP where the chiral near-field volume average is zero as both helicities are present at the same ratio, observed in Fig. 24(center). Such a performance was a severe limitation in previous attempts

to generate uniform superchiral near-fields with achiral plasmonic scatterers which nullifies chiral light-matter when a chiral molecule is placed on such a substrate [91, 98, 102, 103].

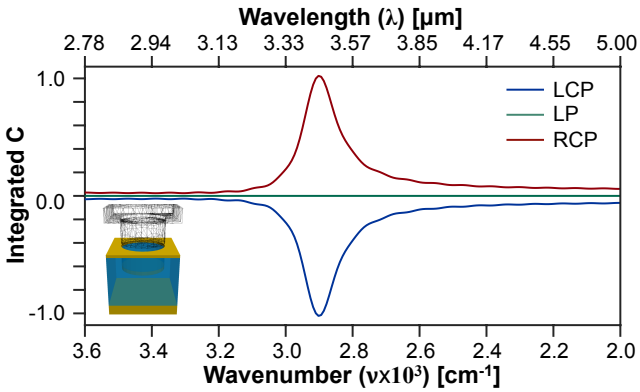

Figure 25: Volume integrated chiral density in the upper stratum, as observed in the inset, for three incident polarization conditions, LCP, LP and RCP.

Table 2: Percentage of the spectral and volume integrated chiral density for LCP, LP and RCP in the upper stratum.

Polarization	$C < 0$ [%]	$C > 0$ [%]
LCP	99.96	0.04
LP	50.00	50.000
RCP	0.04	99.96

3.4.2. Non-degenerate achiral systems.

In this section I will discuss the plasmonic resonance degeneracy effect on the chiral near-field generation in symmetric and achiral systems based on circular and elliptical holes. The plasmonic system is a far-field coupled to a photonic cavity forming a hybrid plasmonic-Fabry-Perot resonator that allows a special resonance hybridization which leads to a unique superchiral light formation in the near-field [96, 113]. It is observed that by lifting the degeneracy the spatiotemporal field

distribution is disturbed degrading the system capability to produce single-handedness superchiral fields.

The plasmonic system is based on a symmetric two-dimensional array of circular holes with 1500 nm period ($P = Px = Py$) and 250 nm diameter ($D = Dx = Dy$) on a 30 nm thick gold film on a dielectric substrate. Finite difference time domain (FDTD) numerical simulations were performed on a unit cell with linearly polarized light along each of the lattice principal axes (Ex or Ey). This systems support degenerate plasmonic resonances ($\lambda_{Dx} = \lambda_{Dy}$) along each of the lattice axes as observed in absorption spectrum in Fig. 26(a). When the circular hole turns elliptical with 300 and 250 nm diameters along the lattice axes (Dx and Dy respectively), the plasmonic resonance degeneracy is lifted ($\lambda_{Dx} \neq \lambda_{Dy}$), which is observed in the frequency splitting in Fig. 26(b). Now, for an achiral and asymmetric plasmonic array two nondegenerate resonances are supported which will have detrimental effect on the chiral near field-generation.

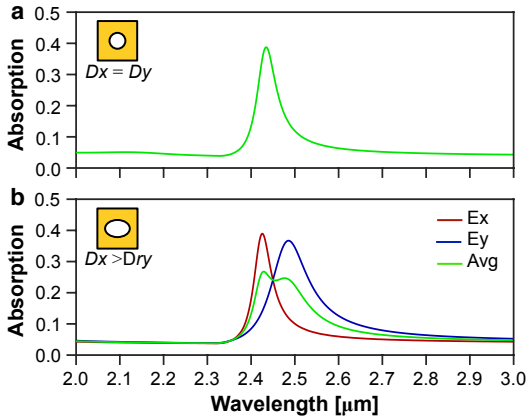

Figure 26: (a) Absorption spectrum for the 2D symmetric hole array with ($D = Dx = Dy =$ 250nm) and $P = 1.5$ μm. (b) Absorption spectra for an asymmetric elliptical 2D array with ($Dx = 300$ nm and $Dy = 250$ nm) and $P = 1.5$ μm when excited with LP along both lattice axes (Ex and Ex) and the corresponding superposition.

The response of the cavity-coupled system shows similar effect as the uncoupled plasmonic array. For the symmetric 2D array the cavity dispersion shows the same plasmonic modes

supported in both lattice axes. So the superposition will lead to two degenerate modes as observed in absorption dispersion plotted in Fig. 27(a). This is not the case again with the asymmetric configuration where now the system response is polarization dependent and the superposition will lead to a two absorption peaks, as seen Fig. 27(b).

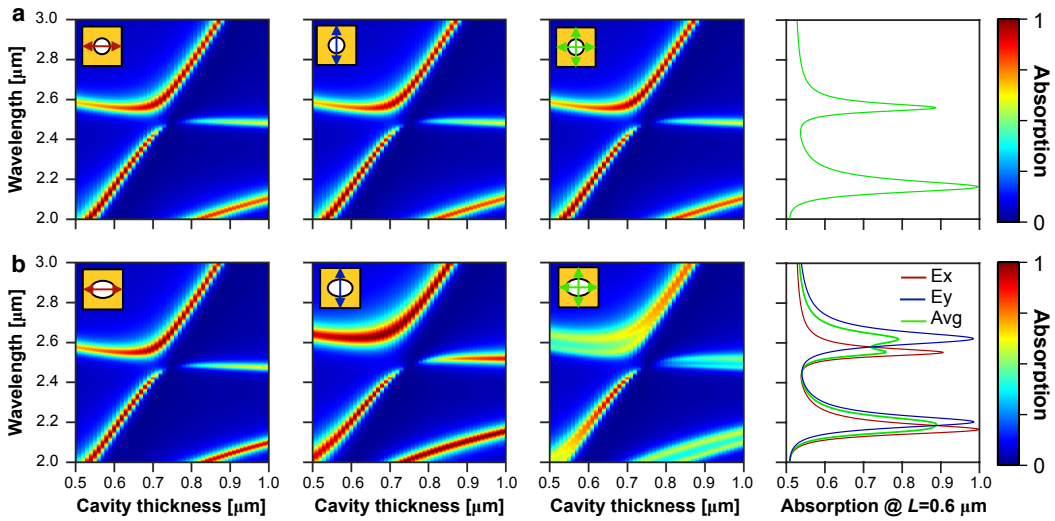

Figure 27: Cavity-coupled absorption dispersion spectra for, from left to right, LP along x, LP along y, its supperposition and the corresponding spectra for cavity thickness $L = 600$ nm for the 2D (a) symmetric (circular) and (b) assymmetric (elliptic) hole array.

The inspection of the resonance temporal distribution reveals another property of these two systems. As previously discussed it is the rotation of the plasmonic element, due to the degenerate plasmonic resonance, that produce single sign chiral near fields. In this case the non degenerate LSP modes supported by the asymmetric array will show a slight different temporal distribution. Figure 28(a) shows the time evolution of the plasmon mode, ploted as the $\mathrm{Re}(Ez)$, along one optical cycle when excited with LCP. The 2D symmetric system shows a full 360° whereas the 2D asymmetric experiences an partial rotation with a dominant beating effect, such as that observed for a linear dipole, see Fig. 28(b). Furthermore, the electric and magnetic field intensities for both conditions, plotted in 28, shows that the electric and magnetic field intensity enhancement factors

are in the order of hundreds and, while the distribution for the 2D symmetric is uniform around the hole, as previously observed, the 2D asymmetric is mostly dominated as a linear dipole profile.

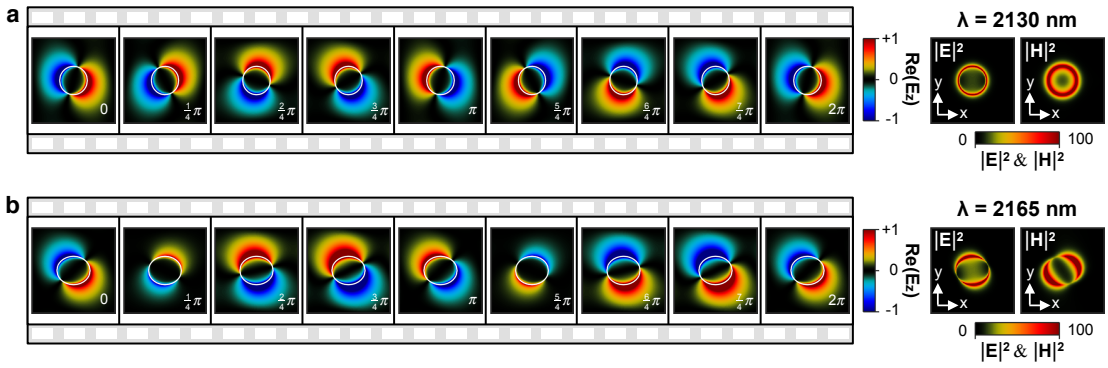

Figure 28: Time evolution over one optical cycle of the (a) degenerate and (b) non-degenerate plasmonic resonance at $\lambda = 2.13$ μm and $\lambda = 2.165$ μm, respectively, and $L = 600$ nm. The right panels shows the time averaged spatial electric and magnetic field intensity distributions 5 nm above the hole.

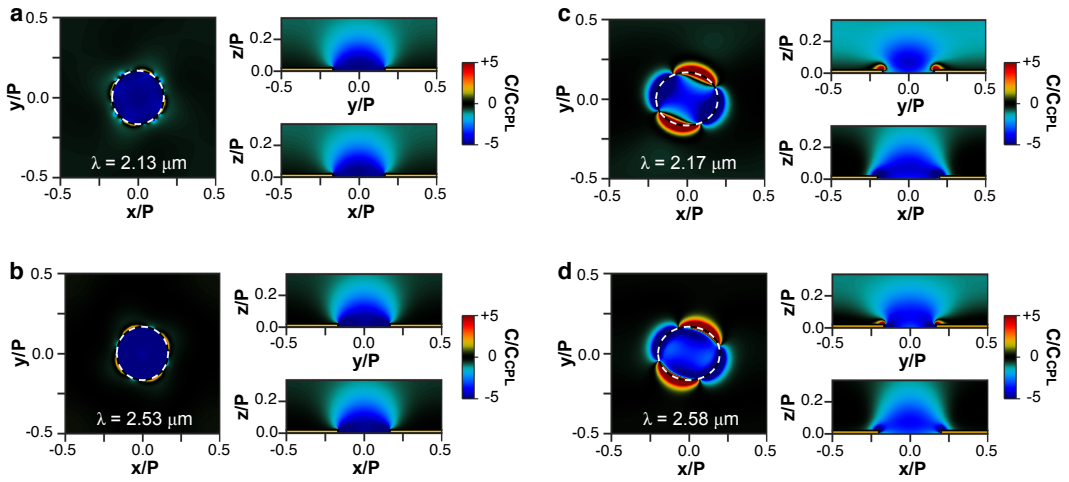

Figure 29: Chiral near-field spatial distribution for a cavity thickness of $L = 600$ nm. (a) Symmetric 2D array at $\lambda = 2.13$ μm, (b) symmetric 2D array at $\lambda = 2.13$ μm, (c) asymmetric 2D array at $\lambda = 2.17$ μm and (d) asymmetric 2D array at $\lambda = 2.58$ μm.

The final effect of this non-degeneracy is observed in the chiral near field generation. Solv-

ing Eq. 16 in the upper stratum above the hole reveals that the chiral near field is single sign in the entire volume, as observed in the spatial distribution plotted in Fig. 29(a) for $\lambda = 2.13$ μm, with very negligible contribution from the opposite chiral density sign. In addition, at a higher wavelength $\lambda = 2.53$ μm similar effect is observed but with slightly higher contribution of the opposite chiral near field, which is plotted in Fig. 29(b). But, for the asymmetric case there is a finite contribution from the opposite chiral density sign in the volume of interest for both as observed in Fig. 29(c) and Fig. 29(d) for two wavelengths $\lambda = 2.17$ μm and $\lambda = 2.58$ μm, respectively. Notice that the cavity-coupled system was exited by LCP along the $\mathbf{k} = -k\hat{z}$ which according to Table 1 $C/C_{CPL} < 0$ which correspond to the spatial distribution in blue color. In both scenarios the total chiral near field is superchiral with magnitudes higher as those previously shown in Fig. 24. This is due to the nature of the LSP mode as they produce more intense electric and magnetic field enhancement factors.

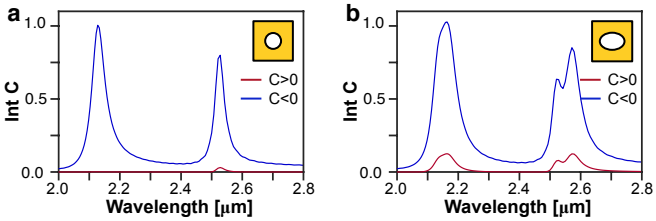

Figure 30: Volume integrated chiral density for (a) symmetric and (b) asymmetric 2D array for cavity thickness of $L = 600$ nm.

Finally, volume integration, as given by Eq. 35, demonstrate the ultimate chiral near field generation efficacy. Figure 30(a) shows the volume integration of the symmetric 2D array. As observed in the $\sim$ 2.1 μm band only one chiral near field density sign is present in the entire volume, which corresponds to the condition plotted in Fig. 29(a). For the same configuration but at a different wavelength $\sim$ 2.5 μm minor contribution from the opposite chiral near field is observed, similar to the observed red shades in 29(b). On the contrary, the volume integration on

the asymmetric 2D array shows that, at both resonant bands $\sim$ 2.1 μm and $\sim$ 2.5 μm, there exist the contribution from both chiral near fields. The contribution from the incident wavelength (LCP) dominates the overal response, such as seen in Fig. 29(c) and Fig. 29(d), but a finite contribution from the opposite handedness is observed yet confined at the near field, see cross section in Fig. 29(c) and Fig. 29(d).

Contrary to what was previously discussed and proposed, chiral light-matter interaction can be exploited in a full achiral and symmetric plasmonic system as demonstrated here. In this regard I demonstrated for the first time the generation of single-sign superchiral light on an achiral degenerate plasmonic systems and showed how to manipulate its sing only by the polarization of the excitation illumination [96]. This concept is expected to excite the field of plasmonic-enabled light-matter interaction applications due to its potential to perform surface-enhanced processes most efficiently as demonstrated in Chapter 5.

4. FABRICATION METHODS AND CHARACTERIZATION

4.1. Nanoimprinting lithography technique.

The majority of plasmonic nano and submicrostructures are fabricated using traditional top-down and bottom-up techniques, which each offer a particular set of advantages and disadvantages. For example, bottom-up techniques are commonly used in the chemical synthesis nano particles of different shapes and dimensions which suitable for mostly solution-based plasmonic applications or surface coatings. Furthermore the long range aligning in, 2D arrays for example, is far from being reached under practical perspective even when it render cost effective. On the other hand top-down techniques are quite popular to fabricate high quality nanostructures widely used in plasmonic applications. For example the majority of previously reported LSP applied to biosensors were constructed by periodic two-dimensional arrays of isolated metallic nanoparticles or perforated holes on a continuous metallic film. They are typically fabricated using top-down techniques, such as electron-beam lithography [169,170], focused-ion beam lithography [50,61], nanosphere lithography or hole-mask colloidal lithography [22,52,53,116,171–174]. In one hand, electron-beam and focused-ion-beam lithography are very expensive, time-consuming and offer low device throughput typically over 100 x 100 μm^2 pattern area. On the other hand, the nanosphere and hole-mask colloidal lithography are cost effective but lacks reproducibility in the self-assembling process.

An alternative fabrication method is the soft nanoimprint lithography technique, also called soft lithography, which is a cheap and fast nanofabrication technique capable of producing high-quality devices with preset geometries. This versatile nanofabrication is cost effective and allows mass scale replication of any arbitrary 2D and quasi-3D plasmonic substrate designs with high spatial resolution ($\sim$30 nm), over large area on planar or curved surfaces without the need for further post processing [175–177]. Therefore, a wide variety of nanoimprinted surfaces with locked-in dimensions are possible with designed optical responses appropriate for the application of interest,

for example sensing [133, 178–182], color surface generation [60, 183], superchiral light generation [96], metamaterials [110, 111, 184] or as an intermediate fabrication in functional optical devices [185–188]. In this work I employ the nanoimprinting lithography (NIL) technique 1) to fabricate the devices used in all the biosensing experiments presented in Chapter 5, and 2) to prepare the hardmask to ink and transfer to another substrate in order to experimentally demonstrate the results presented in Chapter 2.

The NIL technique starts with the writing of a high quality master patter using a conventional lithography techniques, such as ebeam lithography, focused ion beam milling, deep UV lithography or even colloidal mask lithography. Whichever is the route at the end there will be a hard phase mask that will contain the geometrical configuration. Then the surface is passivated with a hydrophobic layer. For this, the device is kept in a vacuum chamber containing a fluorosilane vapor for two hours, usually tridecafluoro-1,1,2,2,-tetrahydrooctyl-1-tricholorosilane. This ultra thin film of a couple of monolayers allows easy detaching in the following step. The following step is to prepare a combination of hard (h) and soft (s) polydimethylsiloxane (PDMS). The h-PDMS is poured, and usually spin coated to form a thin layer on the passivated surface to replicate. This mix is a high Young modulus capable of embossing the space phase information onto a polymer substrate. The s-PDMS works only as a carrier medium. Once cured, the PDMS stamp is detached and ready to replicate the original master pattern.

There are several polymers commonly use in NIL. For example polymethyl methacrylate (PMMA), mr-I 7000R and mr-I 8000R, mr-NIL 6000E, mr-UVCur21, and some others comercially available (Microresist Technology). In this work I employed the resist SU-8 2000.5 (Microchem) as the polymer substrate. This is a positive resist commonly used in UV lithography, when heated above the glass temperature ($\sim 95^{\circ}$C) it becomes maleable, hence pressing the PDMS stamp onto the warm substrate will emboss the pattern. Furthermore, it is UV curable, which allows to keep the imprinted pattern without any risk pattern deformation. Then, any subsequent additive or subtractive nano or micro fabrication process is followed to finalize the target device.

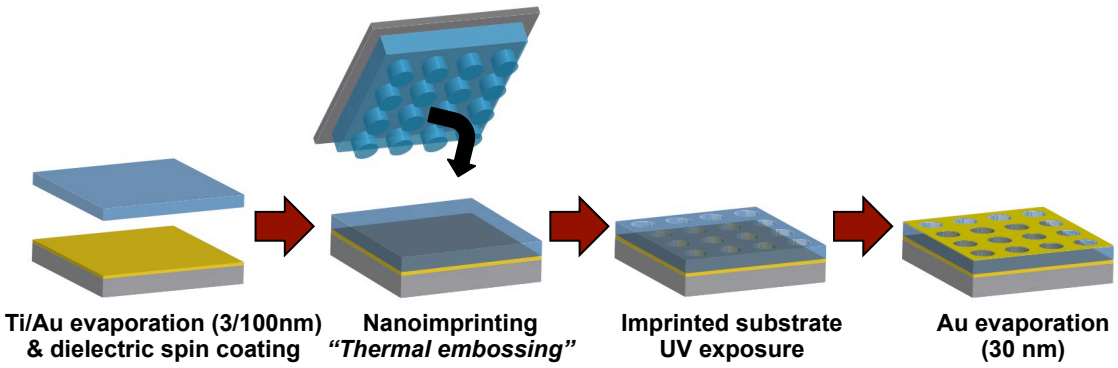

Figure 31: General NIL fabrication workflow for the cavity-coupled plasmonic devices.

Following this method the cavity-coupled plasmonic biosensors were fabricated. The device starts with a 1x1 in^2 glass slide thoroughly cleaned with acetone, isopropanol and water followed by $\sim$ 1 hr baking at 100°C. Then an optically thick gold mirror (80-100 nm) is ebeam evaporated on a previously coated 3 nm titanium layer as the adhesion layer. The following step is to spin coat the SU-8 2000.5 layer whose thickness will depend on the desired cavity thickness for the sensor, usually spin coating at 3000 rpm for 1 min for a $\sim$700 nm film thickness. After 1 min baking at 95°C for 1 min the PDMS stamp is pressed on the SU-8 coated substrate and then the composite is placed on the hot plate, same temperature, and press for an additional $\sim$30 s. The PDMS stamp and substrate are removed from the hot plate and let to cool down while still gently pressing for at least another 30 s. Finally the PDMS is delaminated from the substrate that will contain the replica of the original master pattern. One minute UV exposure (365 nm) followed by and additional 1 min post exposure bake will conclude the imprinting process. The final device is completed by ebeam evaporating 30 nm of gold. This fabrication workflow if summarized in Fig. 31 which is same for those devices demonstrated in Chapter 5.

4.2. Transfer printing method.

The transfer printing method is an alternative method to fabricate a special kind of devices in which traditional lithography techniques would render not practical [111]. For example the continuous metallic thin film perforated with a periodic hole array on a polymer substrate and forming the hybrid cavity-coupled systems as studied in Chapter 2.

The process starts with a clean silicon substrate in which a diluted 4% SU-8 2000.5 in cyclopentanone solvent is spun coated at 3000 rpm for 1 min. Then the NIL technique is employed to make an array of holes on the polymer same as used in section 4.1. After this imprinting step the pattern is then transferred to the hard silicon substrate using reactive ion etching. For this, oxygen (O_2, 15 mTorr, 50 W and 10 sccm for 50 s) plasma is employed first to clean the thin residual pedestal at the bottom of the hole and then sulfur hexafluoride (SF_6, 100 mTorr and 43 sccm for 150 s) chemistry is used to etch into the silicon. The etched substrate is then ebeam evaporated with 50 nm of silicon dioxide (SiO_2) sacrificial layer and 30 nm of Au. The sacrificial SiO_2 layer is gently etched with hydrofluoric acid at 1% in deionized water. Separately, a 25:1 PDMS and curing agent (Sylgard 184, Dow Corning) is prepared and baked for 20 min at 65°C. This mix ratio produces a sticky PDMS block that allows easy pick up of the released Au film after HF etching of the SiO_2 layer. In parallel, the substrates were prepared following same procedure as in section 4.1 until the spin coating without any baking at this time. Having a fresh SU-8 film on a back mirror the PDMS block with the released perforated gold film are brought in contact and placed on the hot plate for around 1 min gently pressing. This step reduces the adhesion between the PDMS and Au film. Finally the thick PDMS block is slowly delaminated from the substrate leaving the perforate gold on top of the SU-8 film. The whole fabrication process is summarized in Fig. 32.

It is worth mentioning that this process is not that straightforward as special care needs to be paid in several steps. For example, if the HF concentration is too high, the etching rate into the SiO_2 will be too fast that the patter will be buckled up and destroyed. In addition, too

sticky PDMS might pick up the released Au film very easy but might not release it afterwards, so the baking needs to be monitoring. In addition continuous and large area and very thin films are always subject to cracks. So it would be desired to have smaller sections, 1x1 mm^2 sections instead of the full 20x20 mm^2.

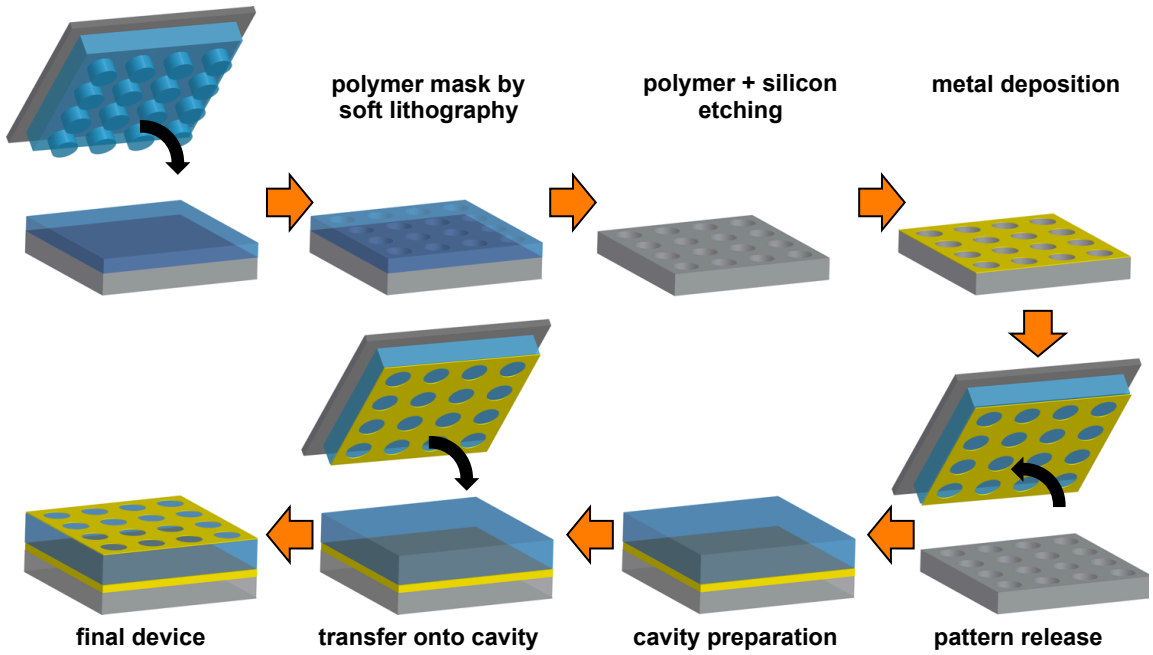

Figure 32: Transfer printing workflow: nanoimprinting on diluted SU-8, dry etching on polymer and silicon, SiO_2/Au layer deposition, SiO_2 etching and release, cavity preparation and thermal transfer.

4.3. Microfluidic channels fabrication.

Microfluidic channels technology has enabled the advance in medicine, biology and diagnostics. It allows the controlled assay with high space and time precision. It also allows the multi platform integration with plasmonic biosensors in which the analyte of interest is delivered right to the active sensing area. In this section I will go over the fabrication process of such systems employed in some of the biosensing demonstrations. It consists on three steps: the mold fabrication, the PDMS

channel fabrication, and the final device integration.

The mold fabrication process starts with a clean 3” silicon wafer, acetone, isopropanol and deionized water followed by 5 min baking at 120 °C. This baking step is important to allow any liquid residue on the surface to evaporate. Then in a closed container, a vacuum jar at mild vacuum could work too, the silicon substrates are placed along a disposable dish with some drops of hexamethyldisilazane (HMDS) as an adhesion promoter and kept for 30 min. The surface treated substrates are then spin coated with SU-8 2050 at 3000 rpm for 1 min. This film will dictate the height of the channel. The coated silicon substrate is soft baked at 65 °C for 3 min and 95 °C for 8 min followed by a 30 s UV (365 nm) exposure with the appropriate UV chrome mask. This time might vary depending on the light intensity of the mask aligner. The following step is the post exposure bake, 65 °C for 2 min and 95 °C for 2 min. This is very important has the SU-8 cross linking will not be completed in the absent of heat treatment. Finally, the silicon substrates are developed in propylene glycol methyl ether acetate (PGMEA) for 5 min. Then the silicon wafers are transfered to another PGMEA fresh bath for an extra 1 min followed by isopropanol rinsing. If a white stream apears on the surface means that there is still PGMEA and SU-8 residues on the surface, hence the samples are placed in the last fresh PGMEA for an extra 1 min. The outcome will be a silicon substrate that contains the inverse of the microfluidic channels made of SU-8.

Once the mold is finished it is surface treated again to create a hydrophobic following same process as in section 4.1 (fluorosilane). In parallel a 10:1 ratio of PDMS to curing agent is thoroughly mixed for 5 min and degased until it becomes a clear, bubble-free, solution. The fluorinated substrate is placed on a petridish or in an aluminum-made petridish which will allow easy demolding and prevent possible destruction of the mold. The PDMS is then poured onto the mold and let sit for 1 hr to let any bubble escape, then it is baked at 75 °C for 1 hr. The cured PDMS, with the aid of a sharp razor blade is delaminated from the substrate and trimmed according to the designed chip footprint. Then the inlets and outlets holes are punched with a biopsy pen with the desired diameter. If the demolding is successful and the substrate was not broken in the process

the silicon mold can be used, as is, for several replication rounds.

The microfluidic chips made of PDMS are now ready for integrating to the plasmonic device. If the substrate containing the plasmonic array and the PDMS block is needed to stay covalently bonded, while the substrate is silicon or glass. Both devices are treated with UV ozone for 5 min to activate their surfaces and then brought together in contact and placed on the hot plate at 100 °C for 30 min. This will allow the water byproduct coming from the covalent bond to difuse into the bulk PDMS. On the other hand, if there is not a need of a covalent bond or the surface of the device does not have any silicon of silicon dioxide, the PDMS block can be secured with a mechanical clamp. This will provide a temporary bond to keep the PDMS in place without further liquid leakage when increasing the input pressure. In addition, after the experiment the PDMS chip is thoroughly cleaned with acetone and isopropanol and will be ready for another test.

4.4. Optical characterization.

The optical characterization is based on optical spectroscopy, near infrared (NIR) for the spectral characterization as employed in Chapter 2 and Chapter 5, and infrared (IR) for the spectral characterization shown in Chapter 5. The spectrometer used is a microscope-coupled Fourier transform infrared (FTIR) spectrometer (Hyperion-Vertex 70, Bruker Optics) interfaced with the data acquisition software OPUS^{TM} (Bruker Optics). For the NIR the system is configured with a calcium fluoride (CaF_2) beam splitter, 0.7 NA CaF_2 objective, silicon gap detector and tungsten light source. The background spectra was referenced on a thick gold mirror. Throughout the series of optical characterization the spectra were retrieved with a 20 kHz sampling rate and 56–128 scans. In the all the spectral measurements in the NIR the reflectance spectra was acquired with linearly polarized light.

For the IR domain the FTIR spectrometer was configured with a potassium bromide (KBr) beam splitter, 0.7 NA CaF_2 objective, mercury cadmium telluride nitrogen cooled detector and

globar light source. Same gold mirror was used for the reference and the spectra were retrieved with a 20 kHz sampling rate and 256 scans. This characterization was employed for the molecular chirality detection as described in Chapter 5. Therefore, the microscope was equipped with a linear polarizer and a magnesium fluoride (MgF_2) quarter wave plate (QWP) (Bernhard Halle Nachfl. GmbH) in order to create CPL that impinges on the sample such as depicted in Fig. 49(b). In this configuration both polarizer and QWP were frequency matched and covered the 2.5 to 7 μm (4000-1430 cm^{-1}). In this particular experiment protocol two background references were collected, one for each polarization (LCP and RCP), and used in when acquiring the corresponding measurement. Finally, the data was exported and analyzed in MATLAB.

5. BIOSENSING: ACHIRAL AND CHIRAL ANALYTES

5.1. Introduction.

Simple optical techniques that can accurately and selectively identify organic and inorganic material are of paramount importance in biological sensing applications. The detection and quantification of minute concentrations of biological compounds is of profound interest in diagnostic methods. While a binary detection, *i.e.* target analyte is present in the tested sample above the limit of detection, suffices in some applications others require its quantification. For example, some biological agents in our body can indicate an early stage of a disease development, for example the prostate-specific antigen (PSA) [189], the ovarian cancer cell line CA-125 [190], exosomes (microvesicles secreted by cells) [191, 192], or antibodies (present in our body as an immune system reaction against invasive antigens) [193].

Traditional labeled methods to detect biomarkers at low concentrations are the enzyme-linked immunosorbent assay (ELISA), Western blot, radioimmunoassay or those employing flourogenic or electroluminescent labels [194]. Nevertheless, these techniques are costly, time consuming and require specialized equipment and large amount of analyte. An alternative biosensing technique is the use of localized surface plasmon (LSP) supported by 2D array of subwavelength metallic scatterers, which offers multiple attractive advantages over traditional methods, for example the capability of free space optical interrogation, label free detection, real-time monitoring, small sample volume and multiplexing scalability [51, 195]. At the LSP resonance (LSPR) wavelength the local electron charge oscillation on the metal-dielectric interface induces strong field localization over subwavelength volumes. In addition, the LSPR is very sensitive to minute environmental fluctuations induced by the change in the local refractive index. An increase in the local refractive index leads to a decrease in the effective restoring force of the electron oscillations due to accumulation of polarization charges inducing a redshift in the LSPR [55].

In biological sensing applications, any biomolecule with finite optical density can trigger a measurable LSPR shift that can be quantified by optical spectroscopic techniques. Nevertheless, such inherent blindness is overcome by imposing the appropriate analyte-specific surface functionalization, *i.e.*, the target analyte is selectively immobilized on the plasmonic sensor's surface through the strong surfactant-analyte binding affinity. As a result, this refractometric sensing method turns into a powerful biological detection mechanism. Consequently, a large variety of analytes of relevant medical interest have been selectively detected primarily on LSPR shift employing the corresponding analyte-specific surface functionalization scheme, such as cancer biomarkers [191, 196–199] hepatitis antigens [200, 201], Alzheimer biomarker [202, 203], glucose [204–206], DNA strands [54] and proteins [207–209].

In the course of this chapter I will present different affinity sensing experiments that are based on selective surface functionalization depending on the target analyte. The plasmonic sensors, having a locked-in dimensions, support sharp deterministic hybrid resonances when couple with an optical cavity, which demonstrates its suitability for high sensitive surface detection. The surface sensing property of this hybrid system, which is important in biosensing applications rather than the bulk sensitivity, is first quantified by precise atomic layer growth of aluminum oxide using the atomic layer deposition technique. Then, detection of inorganic amine-coated iron oxide nanoparticles, streptavidin protein, dopamine and epinephrine is demonstrated. The soft nanoimprint lithography (SNIL) technique is employed to fabricate the high quality and reproducible biosensing substrates. This versatile nanofabrication technique enables cost effective mass scale replication of any arbitrary sensor design for real applications. We foresee that these highly versatile and selective cavity-coupled hybrid plasmonic systems, in conjunction with the large area SNIL technique, promises low cost biosensor development for the detection of a wide range of biomolecules of medical and scientific interests.

5.2. The hybrid cavity-coupled sensor.

These sensing plasmonic substrates are based on a semi-opaque quasi-3D plasmonic crystal, a dielectric layer and an optically thick back reflector, as observed in Fig. 33. The top plasmonic arrays support weak plasmonic resonances, which are observed as low absorption resonances and weak near-field intensity profiles. Nevertheless, as described in Chapter 2 the plasmonic array can be strongly excited by tuning the cavity thickness that induce coherent excitation of the otherwise weak LSPR.

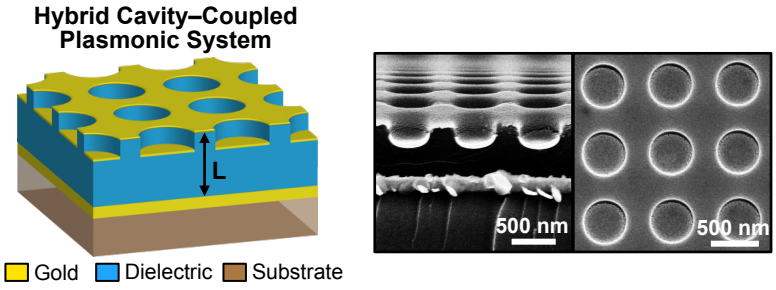

Figure 33: Schematic representation of the hybrid cavity-coupled plasmonic system and SEM image of one fabricated device.

In order to analyzed the optical properties of the system, the optical performance of the uncoupled and coupled plasmonic system is numerically studied using the finite difference time domain (FDTD) method. The model used in the simulations was designed according to the actual fabricated device, see inset in Fig. 34(a) for a cross section view of the model. The refractive indices are 1.56 for the dielectric (SU82000.5) and 1.759 for Al_2O_3. The gold dispersion was fitted to experimental data [145] using a two-pole Lorentzian Drude model. The simulation volume consisted of a symmetric unit cell of 740 nm with periodic boundary conditions in the x and y directions and perfectly matched layers in the z direction. The excitation polarization was in the x direction at normal angle of incidence. Metal discontinuity of 110 nm between top film and bottom disc was used to account for the real fabricated device and evaporating condition using electron

beam evaporation. Refinement meshes were employed as follows: fixed 4 nm mesh in the x and y directions on the whole simulation unit cell and for the z direction 4 nm in the top gold film and bottom gold disc, 5 nm in the well section and 3 nm in the Al_2O_3 layer. The cross section field monitor was placed in the xz plane at $y = 0$ and the top view field monitor was placed 5 nm above the gold film. The above set of geometrical configurations were optimized based on the SEM image cross-section of actual fabricated devices. It is important to notice that several parameters, such as the metal discontinuity and edge roundness play an important role in determining the final spectral shape of an experimentally measured device.

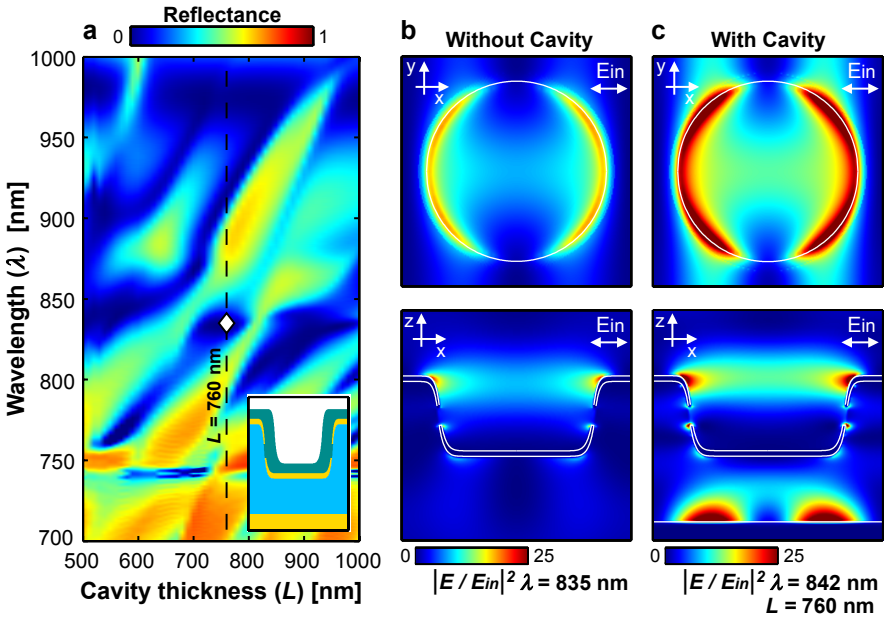

Figure 34: (a) Calculated FDTD reflectance dispersion of the hybrid cavity-coupled plasmonic system as a function of cavity thickness (L). (b) Top and cross sectional spatial field profiles for a plasmonic device without cavity coupling at $\lambda = 835$ nm. (c) Top and cross sectional spatial field profiles for a plasmonic device with cavity coupling at $L = 760$ nm and $\lambda = 842$ nm.

The uncoupled plasmonic system supports a weak LSPR at $\lambda = 835$ nm as seen in the top (5 nm above the surface) and cross-sectional (center of the unit cell) electric field intensity profiles shown in Fig. 34(b). The LSPR linewidth of such uncoupled plasmonic system is ambiguous as

seen in Fig. 35 (green curve). The LSP mode can be strongly excited by tuning the cavity thickness, which allows the Fabry-Perot resonant mode to couple with the broad LSP mode forming a hybrid narrow photonic-plasmonic mode as previously demonstrated in our earlier works [113, 133]. Figure 34(a) shows the FDTD predicted reflection spectra of the hybrid system showing the complex resonance dispersion as a function of the cavity thickness (L). The normalized top and cross-sectional electric field intensity profiles, for L = 760 nm and λ = 842 nm, are plotted in Fig. 34(c). The local field enhancement is considerably stronger (two times) and narrow band in the coupled system ($fwhm$ ~26.2 nm) than its uncoupled counterpart ($fwhm$ ~200 nm) for the same plasmonic mode but slightly redshifted from λ = 835 nm to λ = 842 nm. Compared to the uncoupled plasmonic system, the hybrid LSP mode is ~87% narrower and well defined as can be seen in Fig. 35, which shows the effect of the optical cavity in further reducing the LSPR linewidth as well as enhancement of the local near-field strength. Both local field enhancement and sharp narrowband resonance is beneficial in order to achieve a high figure of merit when such system is used for sensing applications. A strong local field enhances light-matter interaction with the target molecule whereas sharp narrowband resonance improves detectability.

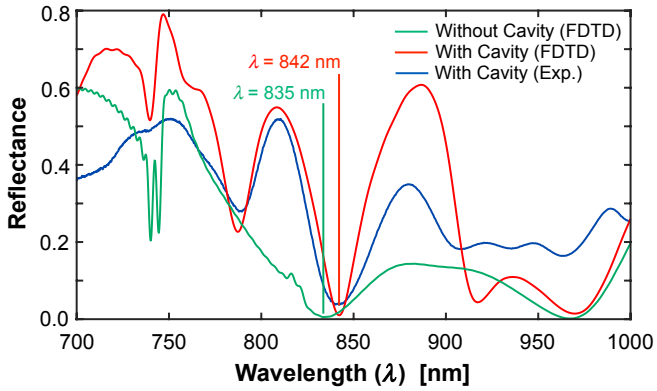

Figure 35: FDTD calculated reflectance spectra of an uncoupled plasmonic system (green) and the hybrid system (red), which show a LSPR at λ = 835 nm and λ = 842 nm, respectively. Reflectance spectra comparison between experimentally measured (blue) and FDTD predicted reflectance spectra (red) for L = 760 nm.

5.3. Surface sensing.

As theoretically demonstrated in a multi-layer stack comprising of an asymmetric Fabry-Perot resonator with a thin aluminium oxide (Al_2O_3) film the photonic resonance does not experience any dispersion with respect to thickness variation for Al_2O_3 film thicknesses less than 100 nm as seen in Fig. 36(a). This is not the case in the plasmonic systems, where the LSP mode generates near-field that extends in the vicinity of the metallic surface, as observed in Fig. 34(c), where any molecule placed within that volume contributes to an observed spectral shift [210, 211]. For example, same Al_2O_3 film test on the cavity-coupled plasmonic system at L = 760 nm shows clear LSPR shift with respect of film thickness, see Fig. 36(b).

In order to experimentally study the surface sensitivity of this device we used the atomic layer deposition (ALD) technique to coat nine high quality conformal layer of Al_2O_3 with atomic layer precision using the Savannah system. Studying the LSPR behavior upon controlled conformal layer deposition provides insights into the surface-sensing abilities of the hybrid LSPR system. FDTD calculations of Al_2O_3 thin film coating were performed to better understand the experimental observations. First of all, this study gives an estimate of the maximum conformal layer thickness that can be measured without detuning the plasmonic hybrid mode away from the photonic resonance. This spectral bandwidth defines the overall dynamic range of the sensor. Secondly, the conformal inorganic material (Al_2O_3) growth on the nanostructured surface functions as a test for the actual biomolecular thin-film coating.

The surface sensitivity is experimentally studied by depositing high quality conformal Al_2O_3 films in 9 nm increments, from 0 to 81 nm, see Chapter 4 for details on fabrication. The reflection spectra were measured after each 9 nm cycle of Al_2O_3 film growth, which are plotted in Fig. 36(c). The LSPR wavelength shifts with respect to the bare uncoated case as a function of Al_2O_3 layer thickness (d) are plotted in Fig. 36(d) along with the corresponding FDTD predictions. A dynamic range of 40 nm was estimated for an Al_2O_3 thickness of 80 nm before the cavity gets

detuned. FDTD calculations show similar trend of the LSPR dispersion as a function of Al_2O_3 as observed in Fig. 36(b) and Fig. 36(d).

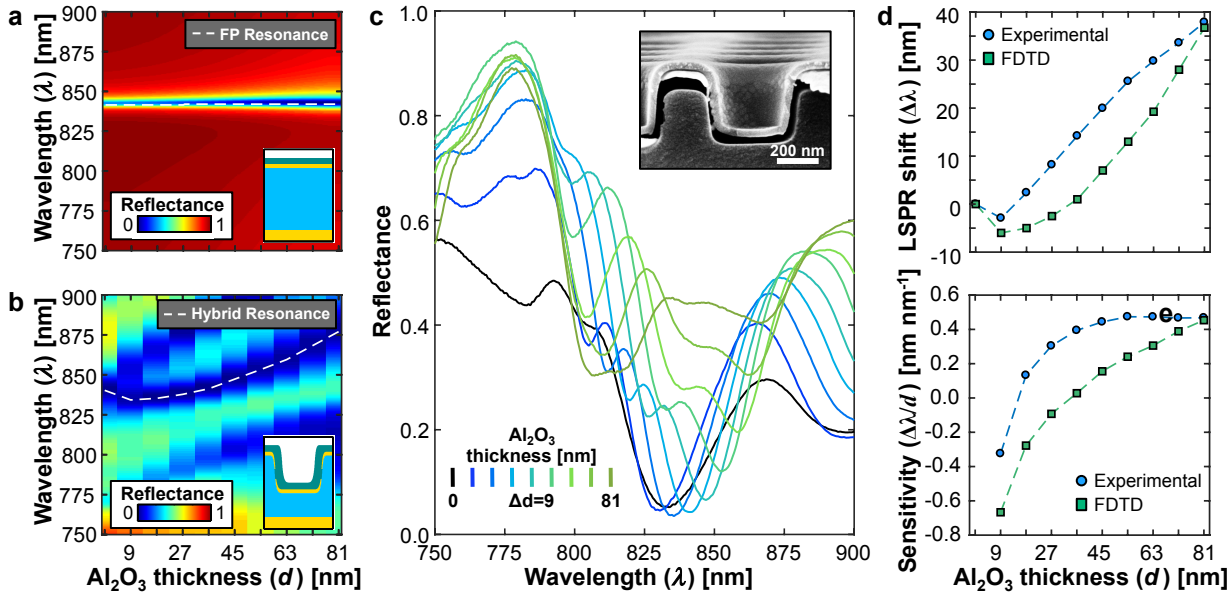

Figure 36: (a) Theoretical reflectance of a multistack showing a Fabry-Perot resonance (white dashed line) independent of the Al_2O_3 thickness (d). The multistack is comprised of air superstrate, Al_2O_3 film (0-81 nm), gold thin film (30 nm), SU8 as a dielectric (760 nm) and gold back reflector (200 nm). (b) FDTD reflectance dispersion of a hybrid cavity-coupled plasmonic system as a function of Al_2O_3 thickness showing the hybrid resonance dispersion (white dashed line). (c) Experimental reflectance of the hybrid cavity-coupled plasmonic system as a function of Al_2O_3 conformal layers at different thicknesses. The inset SEM image corresponds to a coated device with 36 nm Al_2O_3. (d) Experimental (blue circles) and FDTD (green squares) LSPR shift as a function of Al_2O_3 thickness (d). (e) Experimental (blue circles) and FDTD (green squares) surface sensitivity as a function of Al_2O_3 thickness (d).

The surface sensitivity of the system is defined as [211]

$$S = \Delta\lambda/d \tag{36}$$

where $\Delta\lambda$ is the LSPR spectral shift and d is the deposited film thickness. Figure 35(e) shows the spectral sensitivity as a function of Al_2O_3 thickness along with the corresponding FDTD predicted

spectral sensitivity. As observed, both experimentally and numerically, the LSPR blueshifts after the first film deposition and then steadily redshifts until the LSPR decouples from the cavity mode and reappears at a shorter wavelength. This initial blueshift does not arise from the increase in the restoring force of the local electron oscillations but from the detuning effect from the photonic cavity (change in cavity length or round-trip phase), which subsequently red shifts after additional Al_2O_3 layer depositions until completely detunes away from the photonic cavity. Such spectral shift and cavity detuning is the signature of the LSP-cavity interaction because in a system that does not support LSP modes, for example when the top gold film is interchanged by a perfect electrical conductor (PEC), the supported FP modes do not experience dispersion as a function of thin conformal Al_2O_3 layers as seen Fig. 37.

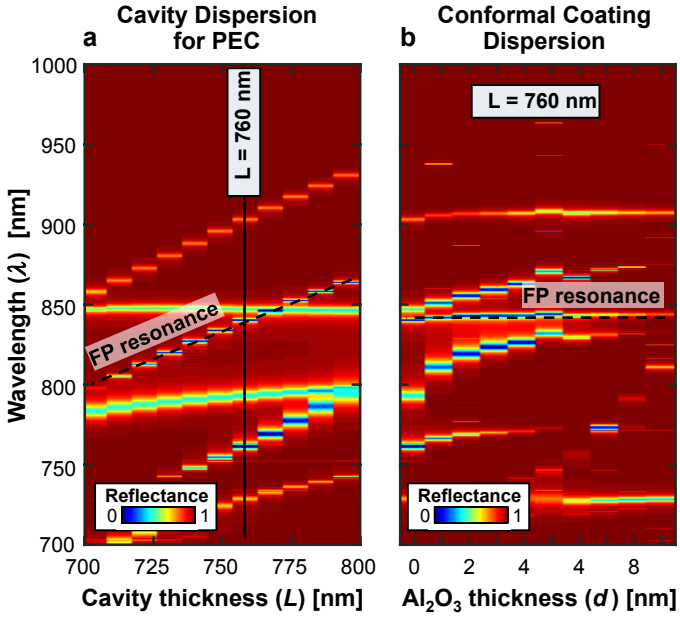

Figure 37: Reflection spectra of a hybrid system with perfect electrical conductor (PEC) interchanging the top gold film. (a) Reflection spectra dispersion as a function of cavity thickness. This graph shows a Fabry-Perot (FP) resonance (dashed line). (b) Reflection spectra dispersion as a function of conformal coating film thickness that shows no dispersion of a FP resonance at L = 760 nm.

5.4. Inorganic sensing of iron oxide nanoparticles.

Detection of inorganic nanoparticles, through the organic amine coating, turns out to be useful due to their ability to amplify the LSP signal when conjugated with other, low mass, analytes [52,209]. The corresponding chemical surface functionalization schemes were employed for analyte-specific binding. The hybrid system, after chemical surface functionalization, captures the target analyte through high affinity binding which results in an LSPR shift. FTIR measurements, see Chapter 4 for more details, were performed to obtain the LSPR at each step of the biosensing progress, the intermediate surface functionalization and the final target analyte capturing (λ_a) . The LSPR reference is that for the device without any treatment (λ_0). The final spectral shift ($\Delta\lambda = \lambda_a - \lambda_0$) will determine then the device response to a particular concentration of analyte. The spectral measurements were performed in a dry environment.

A-IONPs were selectively bound to the gold surface using lipoic acid (LA) and EDC/NHS [212] functionalization chemistry. Each device was washed with deionized water and allowed to dry prior to being submerged in LA (5 mL of 10 mM) and 1,4-Dithio-DL-Threitol (DTT) (5 mL of 10 mM) in pure ethanol. LA reduction allow the thiol groups to bind to the gold surface. The sensors were incubated overnight at room temperature, and then washed twice with pure ethanol to remove any unreacted Dihydrolipoic Acid (DHLA) or DTT. The resulting DHLA coated sensors were activated using different concentrations of EDC and NHS (1:1 ratio, from 1 fM to 100 µM) to activate the DHLA binding sites and subsequently let A-IONPs capturing through a strong amide linkage. A fixed concentration of A-IONP (0.05 mg/mL) in a total volume of 10 mL H_2O was added and allowed to react with the sensor for 15 hrs. The sensors were then washed three times with DI water in order to remove any unreacted or excess material. This chemical workflow is depicted in Fig. 38(a).

Contrary to the conventional binding methods where the entire surface is saturated with the surfactant, which determines the concentration of the analyte that can bind to it, in this method

the DHLA-functionalized surface is activated to bind only a maximum concentration of analyte dictated by the EDC/NHS activating concentration. The graphical representation of the binding process is depicted in Fig. 38(b). In Fig. 38(c) the LSPR spectral shift (red square marks) is plotted as a function of A-IONP concentration showing a logarithmic trend ($R^2 = 0.70$) in LSPR shift represented by the continuous line. A fempto molar concentration was reliably detected with $\sim$6 nm minimum spectral shift.

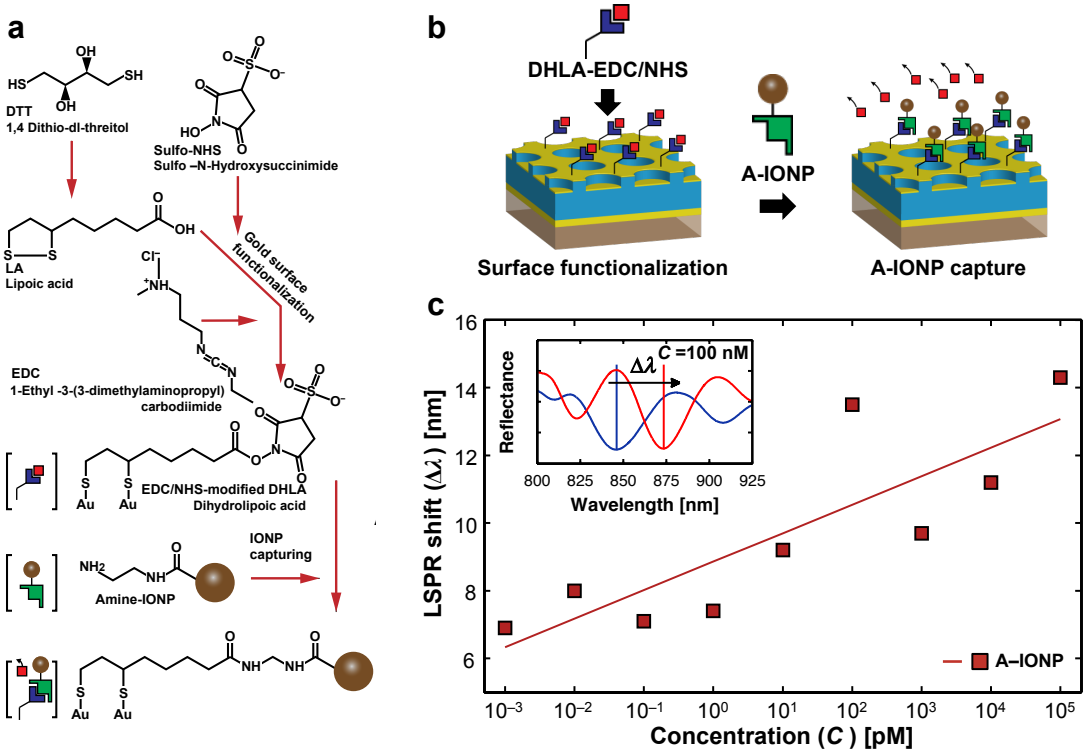

Figure 38: (a) Gold surface functionalization and detection schemes for selective analyte detection of Amine-coated IONP binding. (b) Schematic representation of A-IONP capturing. DHLA-EDC/NHS surface functionalization and A-IONP capture through amine-NHS interchange. (c) LSPR spectral shift of A-IONP with respect to DHLA activated with different concentrations (C) of EDC/NHS chemistry. Continuous line represents logarithmic fit ($R^2 = 0.70$) to the experimental data. Inset shows the reflectance spectra of the sample with $C = 100$ nM.

5.5. Protein biosensing.

5.5.1. Biotin-Streptavidin protein model.

In biological sensing applications proteins are a target analyte as they are present in most of the biomolecules body, cells, bacteria, viruses, and so on. As the first proof of concept a traditional model based on the high affinity biotin-streptavidin conjugate is tested. Furthermore, the biotin-avidin lock-key model is a traditional detection route of a wide range of protein and other biomolecules. The optical characterization mechanism is same as described in section 5.4.

The devices were prepared as follows. Each device was washed with deionized water and allowed to dry prior to being treated with lipoic acid - polyethelene glycol - biotin (LA-PEG_{11}-Biotin) (20 µL of 10 mM) and DTT (20 µL of 10 mM) in DI water to break the sulfur bond in order to facilitate binding to the gold surface. The sensors were incubated for three hours at room temperature, and then washed three times with DI water to remove any unreacted DHLA-PEG_{11}-Biotin or DTT. The devices were incubated in BSA (2 mM) for three hours and washed three times with DI water prior to the addition of streptavidin (40 µL) at different concentrations (7 nM to 14 µM, 1% BSA (v/v)). The sensors were incubated three hours and then washed three times with DI water. The chemical formulation for this experiment is shown in Fig. 39(a) and Fig. 39(b) schematically illustrates the binding process.

The corresponding LSPR shift is plotted in Fig. 39(c), which shows a logarithmic response fit ($R^2 = 0.92$) represented by the continuous line, as a function of avidin concentration. In order to reduce non-specific binding the sensor's surface was saturated with BSA right after the biotin functionalization step. In addition, BSA surface passivation improved detection accuracy by reducing the spread of the measured data compared to the A-IONPs detection (Fig. 38(b)). Nanomolar concentration of avidin was achieved resulting in $\sim$3 nm LSPR shift.

Different plasmonic biosensors, following conventional top-down, bottom-up or a combination of them have been reported with limit of detection in the nano to picomolar range. For

example, Aćimović *et al.* showed, in a microfluidic integrated with gold nanorods, an avidin detection limit of 0.32 nM [199]. Amanda *et al.* used silver nanotriangles and obtained a limit of detection in the low-picomolar concentration without amplification [52]. Guo *et al.* employed gold nanoparticles and multi-walled carbon nanotubes to construct a three-dimensional scaffold working as a biosensor and obtained 0.5 nM detection [213].

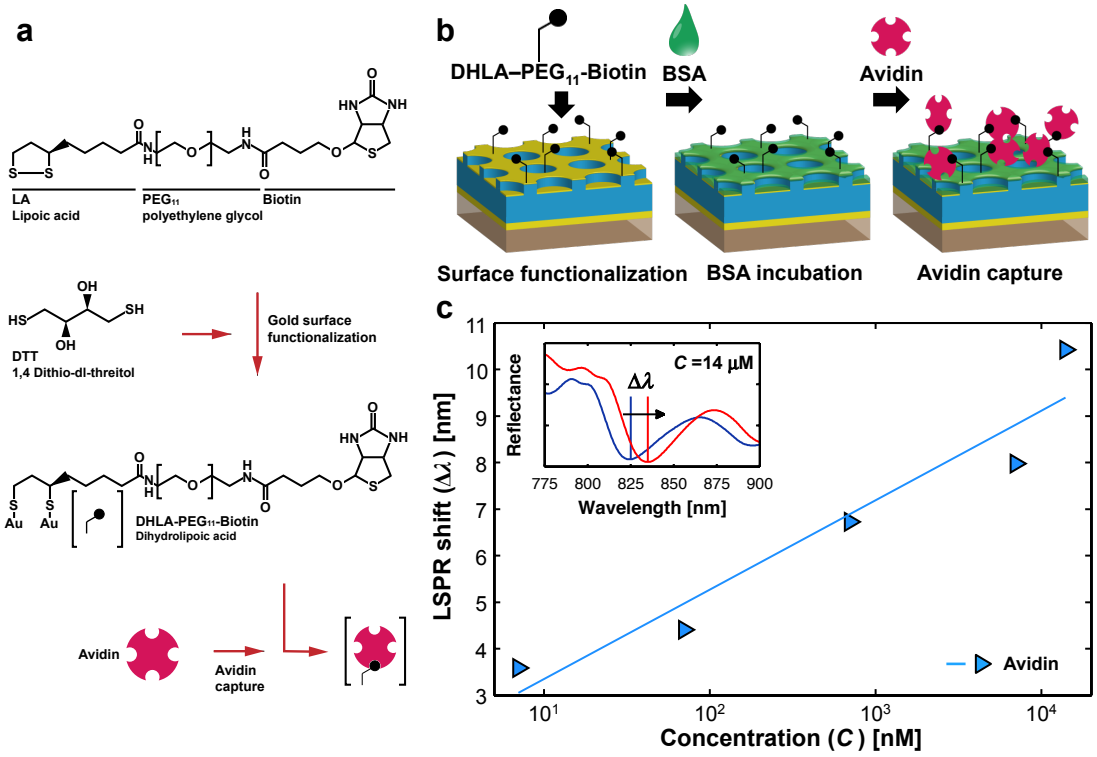

Figure 39: (a) Gold surface functionalization and detection schemes for selective analyte detection of Avidin. (b) Schematic representation of Avidin capturing through sensor's Biotin functionalization and BSA surface saturation for reduction of nonspecific binding. (c) LSPR spectral shift with respect of Avidin concentration (C). Continuous lines represent logarithmic fit (R^2 = 0.92) to the experimental data. Inset shows the reflectance spectra of the sample with C = 14 μM.

5.6. Dopamine biosensing.

Dopamine is an organic electrochemical neurotransmitter that plays a key role in the function of the whole neural system. Many neurological processes are associated with the active dopaminergic neurotransmission, for example happiness, pleasure, addiction, motivation, cognition and fine motor control. Dopamine dysfunction, on the other hand, underlies the pathogenesis of several neurological disorders such as Parkinson's disease, Huntington's disease, depression, schizophrenia or psychosis. It is also a biomarker in the early detection and diagnosis of some cancers such as pheochromocytoma [214–216], neuroblastoma [217], or paraganglioma [218–221]. Therefore, detecting of physiological and clinically significant concentrations of dopamine with high sensitivity and selectivity is of great significance dopamine with high sensitivity and specificity is of paramount importance in basic research understanding the pathophysiology, drug development, as well as in the diagnosis and disease management.

There are currently different dopamine detection methods available. For example, microelectrodes, which relay on the dopamine electroactivity, can be injected near the region of interest for in vivo or in vitro detection of extracellular dopamine levels [222]. Microdialysis, on the other hand, collects biological fluids to be process off-line using a range of analytical methods, such as the high-performance liquid chromatography (HPLC), mass spectroscopy, fluorometry, electrochemical detections, or the enzyme-linked immunosorbent assay (ELISA) [194, 223–225]. However, the current detection limits range in the 1 nM in mass spectrometry, 20 pM for ELISA and 3-8 nM for HPLC.

With the aim to overcome the aforementioned limitation in the traditional dopamine detection methods a myriad of alternative detection schemes have been previously reported, from electrochemical to optical sensors. In electrochemical detection typically modified electrodes are used to enhance the dopamine detection ability. For instance modified electrodes like Au-nanoparticles (NPs) [226,227], Ag NPs [228], single walled carbon nanotubes [224,229], graphene

oxide electrode [230–234], silicon nanoparticles [235], iron oxide NPs [236,237], conductive polymers [238–243], glassy carbon [244–246], and others [247–253]. Electrochemical techniques have the advantages of rapid detection and decreased cost for the detection of dopamine; nevertheless, there are limitations relating its intrinsic transduction. Another important concern is the selectivity in conjunction to oxidizable dopamine metabolites and other compounds like ascorbic acid, which extensively interfere with the detection of dopamine as they have closer oxidizing potentials. Furthermore, most electrochemical detection limits are not close to physiological levels of dopamine, for example plasma dopamine concentration in healthy adults ranges (65-130 pM) [254]. Therefore, the detection of lower concentration of dopamine renders impossible. Optical based dopamine sensors rely on surface plasmon resonances [255–262]. Typically, gold or silver NPs are enzymatically functionalized to bind dopamine and transduce it to an optical signal. However, the main limitation in dopamine detection is its low mass (153.18 Da) hence the lowest detection limits are within 1 nM.

In this section dopamine sensing is demonstrated on our nanoimprinted cavity-coupled plasmonic substrates. The detection method is based on the strong affinity oxygen deficient nanoparticle such as cerium oxide nanoparticles (CNPs) have towards electroactive compounds, such as dopamine. CNPs at the nano scale (3-5 nm diameter) support the coexistence of both Ce^{3+} and Ce^{4+} oxidation states on its surface forming defects in the crystal lattice [1, 263–265]. These oxygen vacancies act like catalytic hotspots for any chemical entity to undergo a unique redox reaction, for example between electroactive compounds in the biological system such as serotonin, epinephrine, dopamine and norepinephrine [1]. As a result, oxidized dopamine binds to the CNP surface forming charge transfer complexes [1] observed in the scattering optical signal modulation. Therefore, CNPs become efficient enzyme-free dopamine optical nanotransducer. Several sensing demonstrations are presented in buffer solutions and in biological fluids, such as plasma.

5.6.1. Interaction mechanism.

CNPs are redox active and support Ce^{3+} and Ce^{4+} ions simultaneously on its surface regulating its enhanced catalytic properties [263]. As previously reported by Hayat et. al. [1] dopamine and CNPs undergo a mutual redox reaction in which dopamine is oxidized and Ce^{4+} is reduced to Ce^{3+}. Then, these two intermediate states binds to each other forming a chemical complex, which is observed as an increase in the optical cross section. This interaction is observed in Fig. 40. Thereby, it is the Ce^{4+}/Ce^{3+} surface ratio (CeSR) that controls the efficiency of the nanoscale redox reaction with different electrochemical compounds, *i.e.* dopamine.

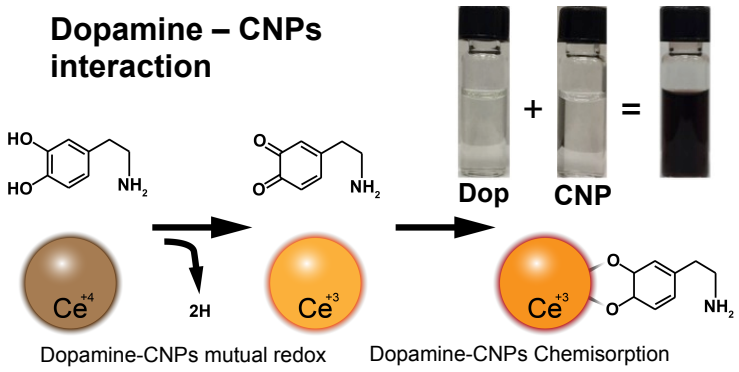

Figure 40: Dopamine and cerium oxide nanoparticles interaction. After mutual redox reaction dopamine and CNPs form a complex which is optically observed as a dark solution given by the change in the optical cross section [1].

In order to test the CeSR effect toward dopamine interaction two CNPs composition were prepared that exhibit different surface chemistry: CNP1 with CeSR > 1 and CNP2 with CeSR < 1. The particles CNP1 and CNP2 have been carefully formulated to have similar spherical shape and size of 3-5 nm that differ only in their surface chemistry. Then, the dopamine-CNPs interaction is studied with UV-Visible electrochemical analysis as a function of oxidation potential. Firstly, dopamine has an extinction peak at 281 nm and gets oxidized upon applying an external potential, which induces an extinction peak at 390 nm as shown in Fig. 41(a). CNP1 (CeSR > 1) solution

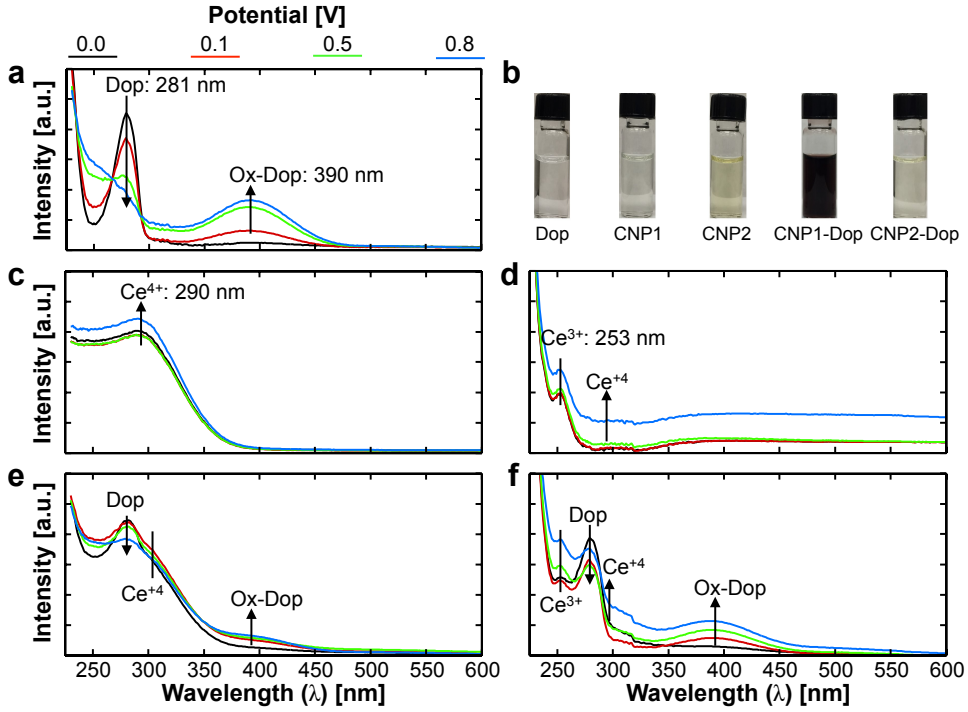

Figure 41: UV-Visible electrochemical analysis of CNPs with two surface oxidation states ratio CeSR and its interaction with dopamine. (a) Oxidation of dopamine alone. (b) Visual observation of CNPs at different CeSR and dopamine. (c) Oxidation of CNP1 (CeSR > 1), and (e) combined with dopamine. (d) Oxidation of CNP2 (CeSR < 1), and (f) combined with dopamine.

has a Ce^{4+} extinction peak at 290 nm. Upon oxidation the Ce^{4+} concentration further increases as observed in the growth of the 290 nm extinction peak as seen in Fig. 41(c). For CNP2 (CeSR < 1) solution the Ce^{4+} extinction peak is not clearly observed, and upon oxidation the increase in Ce^{4+} concentration is manifested as a baseline up-shift as observed in Fig. 41(d). Now, when CNP1 is mixed with dopamine the absorption intensity of Ce^{4+} peak does not increase while the presence of free un-oxidized dopamine decreases (extinction peak at 281 nm), see Fig. 41(e). In addition, the absence of free oxidized dopamine, whose extinction peak does not strongly show at 390 nm, suggests its absorption onto the CNPs surface as previously observed [1]. However, when CNP2 is mixed with dopamine the UV-Visible spectra are a superposition of oxidation of CNP2 and dopamine individually, exhibiting hardly any interaction upon increasing the oxidation

potential as shown in Fig. 41(f). Dopamine-CNPs complex formation is also visually observed. At the beginning both CNPs formulations and dopamine appear clear. Once mixed, there is an immediate change in color for CNP1 (dark brownish) compared to hardly any change observed in CNP2 as shown in Fig. 41(b). This suggests a formation of charge transfer complex, in the form nanoparticle coating, with a decrease of free un-oxidized dopamine, thereby indicating the preference of dopamine oxidation for CNPs with CeSR > 1 as previously observed [1]. The CNPs (from here on refereeing to CNP1) affinity towards dopamine is exploited as an enzyme-free dopamine ligand in biosensing applications.

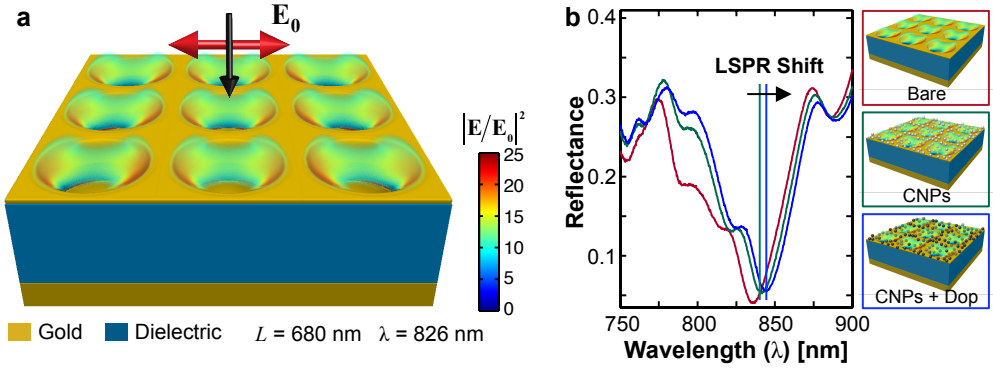

Figure 42: (a) FDTD calculated near-field for the NHPS excited at resonance for a cavity thickness of $L = 680$ nm and $\lambda = 826$ nm. (b) Reflectance spectra of one device experimentally measured at three steps of dopamine sensing as observed in the right panel: bare, after CNPs coating and after dopamine incubation.

The nanostructured hybrid plasmonic sensor (NHPS) is fabricated using the nanoimprinting method, as described in Chapter 4. The active plasmonic substrate is formed by a gold hole-disk system arranged in a square lattice coupled to a photonic cavity producing a strong hybrid cavity-coupled plasmonic resonator, with enhanced near field excitation and narrower plasmonic resonance linewidth [113, 133]. Figure 42 shows the geometry of the NHPS and the engineered near-field intensity profile of the LSP at resonance calculated using the finite difference time domain (FDTD) method. The LSPR is determined by the polarizability of the plasmonic resonator,

which is strongly affected by several factors; however, for a defined geometry the only common factor is the change in the refractive index of the vicinity of the plasmonic resonator. This perturbation can be induced by thin film deposition, either organic or inorganic, or by changing the whole bulk refractive index of the superstrate [178, 210]. Whichever is the cause, the LSPR will suffer a spectral redshift due to accumulation of polarization charges on the metal-dielectric interface. In addition, isolated refractive index perturbations such as nanoparticles can also produce a spectral shift effect on the LSPR. It is the case with CNPs, once attached to the NHPS redshifts the LSPR. Finally, upon dopamine capture on its surface the dopamine-CNP charge transfer induces a change in the CNPs refractive index, in the form of CNPs coating layer, which is further transferred onto the NHPS that experiences an additional LSPR shift. This mechanism is graphically demonstrated in Fig. 42, where one experimentally measured reflectance is captured at three steps of the characterization process. The overall sensor response ($\Delta\lambda_{LSPR}$) is determined by the spectral shift difference from CNPs to the dopamine capture state, see Fig. 42.

5.6.2. Inorganic cerium oxide nanoparticle functionalization.

Cerium oxide nanoparticles (CNPs) stabilized in polyvinyl acetate (PVA) are deposited onto the sensor's gold surface by spincoating. It was found that multiple coating steps were needed in order to produce enough surface coverage of nanoparticle as one spinning step leads poor surface coverage. However, as the surface coating increases it also does the surface to volume ratio lowering that way the reactivity of CNPs toward the target electrochemical analyte. This effect was observed in a characterization experiment where 8, 12 and 16 coating cycles were performed. As seen in Fig. 43(a) the CNPs surface coverage increases as the number of cycles increases and also the LSPR signal from the device increases as seen in Fig. 43(b). However, as observed in Fig. 43(b) the sensor response to dopamine is almost unchanged. Therefore it is not necessary to oversaturate the sensors surface and keep the surface funcitonalization process efficient. For the coming dopamine sensing experiments 8 cycles CNPs coating is adopted.

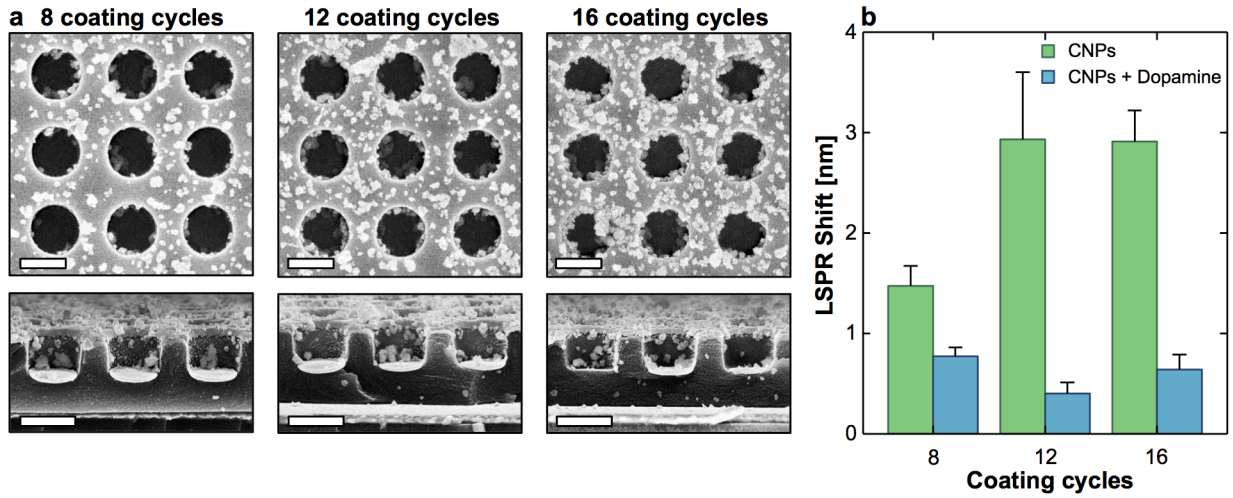

Figure 43: (a) Top and cross section SEM images of sensors coated 8 (left), 12 (center) and 16 (right) times. Scale bar is 500 nm. (b) LSPR response observed in an spectral shift for CNPs coating and dopamine capturing.

5.6.3. Detection in buffer.

The first dopamine demonstration is performed in simulated body fluid (SBF). This type of solution contains same free ionic concentration than human body fluids with the only absence of proteins and cells. The sensor surface consist on a 4x4 mm^2 in which nine spots are optically measured using the FTIR, as described in Chapter 4. After each step extreme care is paid to locate and read the optical signal from each spot. At the end an average of the LSPR is taken and the error bars correspond to the standard deviation. Figure 42(b) graphically shows each step along with the corresponding LSPR shift.

Each sample is coated with CNPs eight times, the SEM of one device is shown in Fig. 44(a), and then dopamine is incubated at different concentrations for one hour. After incubation, each samples what thoroughly washed with deionized water to remove any unreacted dopamine and buffer out of the device and let dry overnight, both at room temperature. In Fig. 44(b) the LSPR shifts as a function of dopamine concentration is plotted. According to these results as low

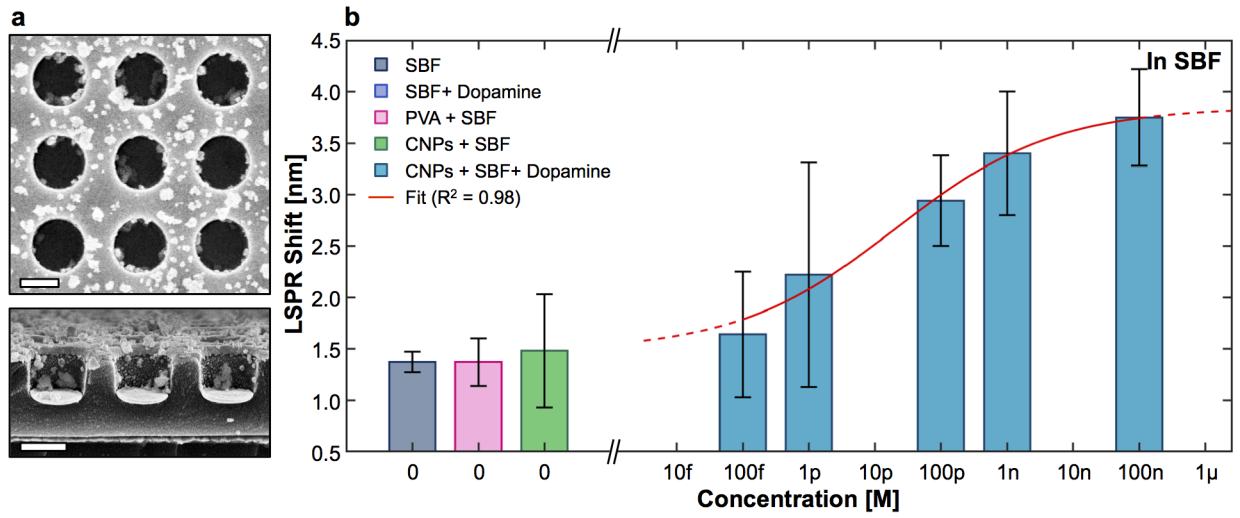

Figure 44: (a) SEM image of one fabricated device. Scale bar is 300 nm. (b) Sensing of dopamine in SBF from 100 fM to 100 nM. Control experiments represent the sensors response in the absence of CNPs coating and buffer effect. Red curve represents fitting to Eq. 37 with R^2 = 0.98. Error bars represent the standard deviation.

as 100 fM concentration was differentiated from the sample pool. The red line in 44(b) is the fit to a sigmoid equation given as

$$f(x) = a + \frac{b-a}{1+e^{-c(x-d)}} \tag{37}$$

where the set of fitting parameters values $\{a, b, c \text{ and } d\}$ are {1.48, 3.85, 0.83 and -10.69} for this experiment with a good of fit of R^2 = 0.98, respectively, and x corresponds to the logarithm of the analyte concentration. According to this fitting model the theoretical limit of detection defined as the concentration at which the total signal drops to 10% is round 10 fM [199].

In order to rule out any affinity towards dopamine besides that of CNPS, a series of control experiments were performed. In first instance, a pristine device was incubated in PBS only. Then a device coated with PVA and incubated in SBF. Finally, a sample coated with CNPs and incubated in SBF. All of these test showed a finite LSPR shift; however, as observed in Fig. 44(b) they all fall below the smallest dopamine concentration on PVA-stabilized CNPs coated devices. It is worth

mentioning that due to the multiple steps involved in the characterization over one to two days, and additional non-uniform CNPS surface coating on the entire 4x4 mm^2 device area, large error bars are observed in the results.

In addition, other catecholamines (compounds containing a benzene ring and two hydroxyl groups), such as 3,4-Dihydrophenylacetic acid (DOPAC) or epinephrine and molecules with same hydroxyl group such as ascorbic acid were tested in order to observe the strength of interaction with CNPs. Figure 45 shows the LSPR shift response of four devices coated with CNPS and incubated with these alike species at the same concentration and compared with that of dopamine alone. It is confirmed that dopamine has the largest response among all four elements in agreement to previous observation in colloidal CNPs [1, 266].

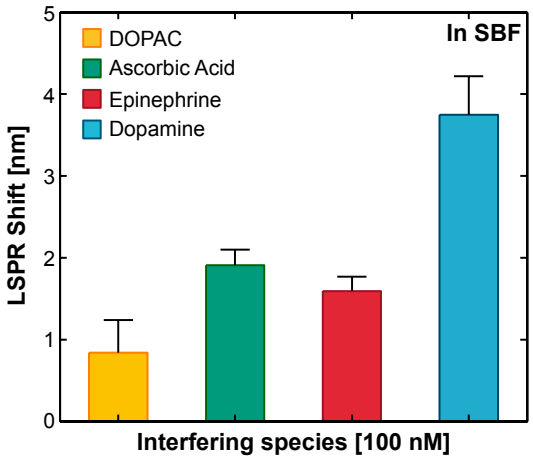

Figure 45: Sensor response to other organic molecules with similar catecholamine moeities (DOPAC, epinephrine) and hydroxyl terminal groups (ascorbic acid) with respect to that of dopamine at the same concentration.

5.6.4. Detection in plasma.

Finally the device was tested in a more complex environment, plasma. This media is the closes to actual biological fluid used in the routine screening taken in the laboratories. It contains the

entire cocktail of ions, proteins, antigen, antibodies, hormones and so on, only with the absence of white and red blood cells and platelets. This preliminary demonstration is carried out with the aim to demonstrate the responsiveness of the device to dopamine when present in plasma. Figure 46 shows the LSPR shift for two samples incubated with sheep plasma containing 10 and 100 nM concentration of dopmaine. Furthermore, a series of control experiments were carried out to rule out the effect of other materials to the entire response of the device. Hence, several devices were prepare. Two devices without coating but incubated in plasma alone or plasma and 100 nM dopamine. One device coated with PVA and another with CNPs and incubated in plasma. As observed in Fig. 46 it is only in the presence of dopamine end CNPs coating where the device reports a larger LSPR signal. All other still have some residual LSPR shift, which is attributed to the possible coating of proteins or other biomolecules on the surface.

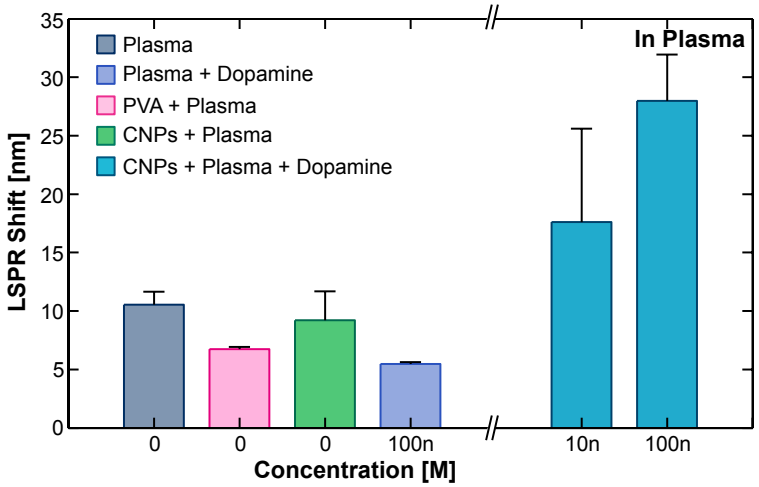

Figure 46: Device response to dopamine present in sheep plasma: a more complex fluid of great interest for point-of-care type of applications. This figure reports the LSPR shift of CNPs coated samples to dopamine and other control experiments.

5.6.5. Dopamine detection in an active plasma separator chip.

The ever-sought goal of plasmonic systems is in its translation to an application that is of great interest for society. In this regard, I demonstrate the detection of dopamine directly from diluted blood using a microfluidic channel system. This plasma separator device employs bio-physical effects such as the Zweigach-Fung bifurcation law and Fahraeus effect [267–269] in order to remove larger hydrodynamic particles from the suspending buffer. Particles, such as blood cells and platelets, can be separated from the plasma matrix at the bifurcation of two channels with a high contrast resistivity, i.e. flow rates.

In this demonstration plasma is separated from the diluted whole blood channel and taken to the plasmonic detection area. Figure 47(a) shows the schematic representation of the microfluidic chip and Fig. 47(b) shows one image of plasma separation on the device. The initial test is performed in two blood samples, one containing 100 nM concentration of dopamine and the other with zero concentration. The assay is run flowing a phosphate-buffered saline buffer (PBS) for around 200 seconds in order to stabilize the device at a pressure of 50 mBar. Then the blood channel is activated with a pressure in the range of 600 mBar in order to produce plasma separation, as observed in Fig. 47(b). In this state the upper branch of the device flows plasma with negligible blood cell content. The system remains in the plasma separation state for an additional 100 sec and then the flow is stop to let the plasma matrix to interact with the CNPs-coated plasmonic surface. Finally the excess plasma is flushed from the channel using PBS.

Figure 47(c) shows the time evolution of the LSPR shift with respect to each state of the device. As observed there in the initial stabilization the LSPR remains unchanged until the plasma separation starts observed as a sudden shift of the LSPR. This is according to the initial change in the liquid refractive index. Then, after ensuring plasma separation, as observed in the inset of Fig. 47(d), the flow is stopped and the LSPR shift starts shifting. After the flush the LSPR returns to its baseline position, which corresponds when the refractive index of the environment solution is

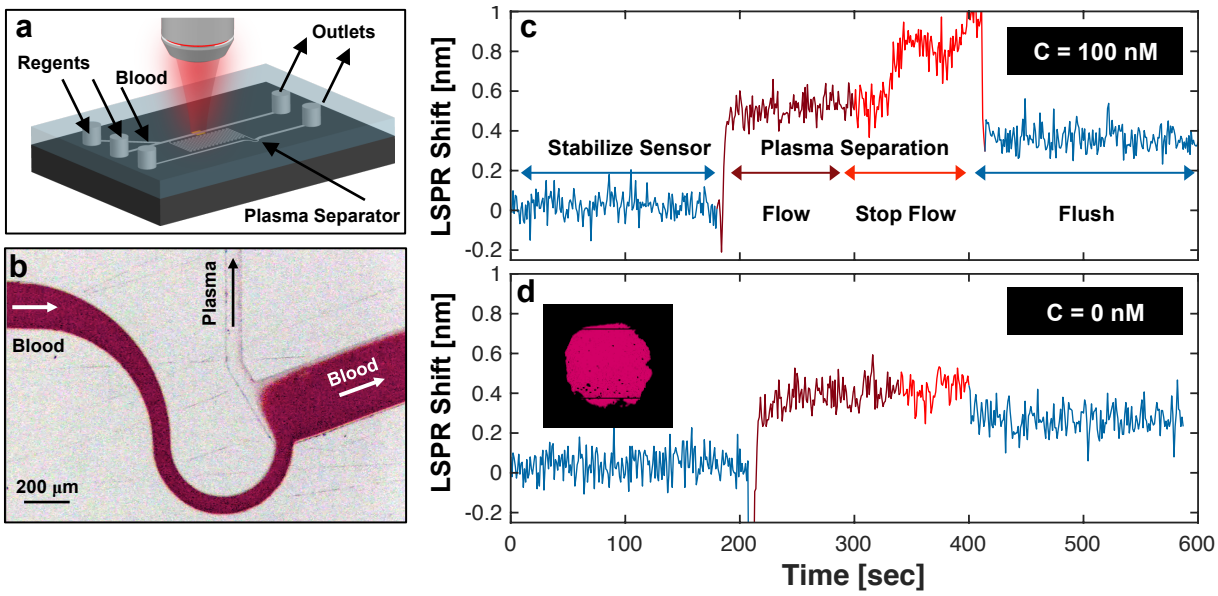

Figure 47: (a) Microfluidic chip that incorporates a plasma separator and plasmonic dopamine sensor. (b) Plasma separation picture for a device running diluted blood at a pressure of 600 mBar. (c) Dopamine detection directly from blood at 100 nM and (d) control sample with same blood without dopamine.

PBS. Comparing with the control sample, which does not include the interaction with dopamine we observed similar effect but without the interaction further shift of the LSPR when the flow is stop. Which confirms the interaction of CNPs-Dopamine.

On observation here is the effect of possible protein coating on the device. Whole blood contains a complex compound of biomolecules present that might electrostatically attach to the gold surfaces. This could be why the LSPR shift does not return to its original baseline after the PBS flush. However, similar effect is observed in both experiments but with a larger offset for that containing dopamine.

5.7. Sensing molecular chirality.

5.7.1 Detection of molecular chirality based on VCD.

The dissymmetry in the absorption rate for an arbitrary molecule under monochromatic CPL excitation is the result of both matter and light chirality [149]. This is carried out through circular dichroism spectroscopy, where the difference in the absorption for CPL or the circular dichroism signal $CD = A^{LCP} - A^{RCP}$ or equivalently it dissymmetry factor

$$g = 2\frac{A^{LCP} - A^{RCP}}{A^{LCP} + A^{RCP}}, \tag{38}$$

reports the intrinsic molecular chiral configuration. Consider for example an ideal molecule electromagnetically described by its electric and magnetic dipole moments $\mathbf{p}$ and $\mathbf{m}$, respectively:

$$\mathbf{p} = \alpha\mathbf{E} - iG\mathbf{B} \tag{39a}$$

$$\mathbf{m} = \chi\mathbf{B} + iG\mathbf{E} \tag{39b}$$

where α/χ are the complex electric/magnetic scalar dipole polarizability and G is the cross term complex electromagnetic polarizability. In reality all these parameters are present in a second rank tensor form; however, for light polarization along the $i = \{x, y, z\}$ the corresponding diagonal elements are dominant as the dipole response is strongly parallel to the polarization of light. The absorption rate for this molecular model is the projection of the dipole moments onto the electromagnetic fields

$$A^{CPL} = \langle \mathbf{p} \cdot \mathbf{E} + \mathbf{m} \cdot \mathbf{B} \rangle^{CPL} \tag{40}$$

For achiral molecules $G = 0$, which leads to $\Delta A^{CPL} = 0$. On the other hand for $G \neq 0$ then a finite value for ΔA^{CPL} is obtained. Under this basic concept the circular dichroism tech-

nique has proved a powerful analytical method to characterize chiral molecules in the UV and IR domains. Nevertheless, chiral molecule's cross section are very small. Henceforth, a high population of them are needed in order obtain a sufficient signal to noise ratio. This is achieve by two methods, one is by increasing the concentration of molecules but without absorbing considerably the probing light. The second is by increasing the detection path length and increasing the assay time.

Another way to increase the dissymmetry factor g is by increasing the chiral density of light. It was previously demonstrated that the dissymmetry factor for chiral molecules as a function of the free-space normalized electromagnetic chiral density C/C_{CPL} is [148]

$$g = -\frac{\mathrm{Im}(G)}{\mathrm{Im}(\alpha)}\frac{C}{C_{\mathrm{CPL}}}. \tag{41}$$

This solution indicates that the dissymmetry is the product of both matter and light and it even suggests a mechanism to enhance it using superchiral light, *i.e.* $C/C_{CPL} > 1$. Nevertheless, while matter chirality is fixed for a particular molecule, it is only the electromagnetic chirality that enhances the dissymmetry in the absorption rate observed in the scattered far-field.

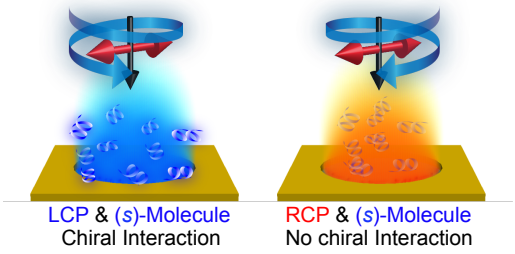

Figure 48: Schematic representation of chiral light-matter interaction between LCP and (*s*)-enantiomer exploited in surface enhanced vibrational circular dichroism spectroscopy.

As described in Chapter 3 plasmonic systems can produce strong chiral near field on demand on achiral plasmonic substrate. In this section I demonstrate surface-enhanced vibrational

circular dichroism (VCD) on an achiral plasmonic substrate comprised of a hole-disk array working in the IR domain, see Fig. 19 and Fig. 24. The test chiral molecule is Camphor on its two enantiomers: (*d*)-Camphor and (*s*)-Camphor. In Fig. 48 the phenomenological representation of VCD for a test (*s*)-Molecule under both signs of superchiral light on the same achiral plasmonic substrate. The plasmonic system is tuned to the C-H vibrational band of camphor, $\nu \sim 3000\ \mathrm{cm}^{-1}$, which are embedded in a polymer matrix solution at ~ 0.614 M concentration, which was spun coated onto the substrate to form a thin film with an approximate 3% molecular filling fraction as observed in Fig. 49(a). The optical characterization is performed using a microscope-coupled FTIR probing 3.8 mm^2 of the sample with an approximate 3.8 nL probing volume. The optical configuration is schematically shown in Fig. 49(b), see Chapter 4 for more details.

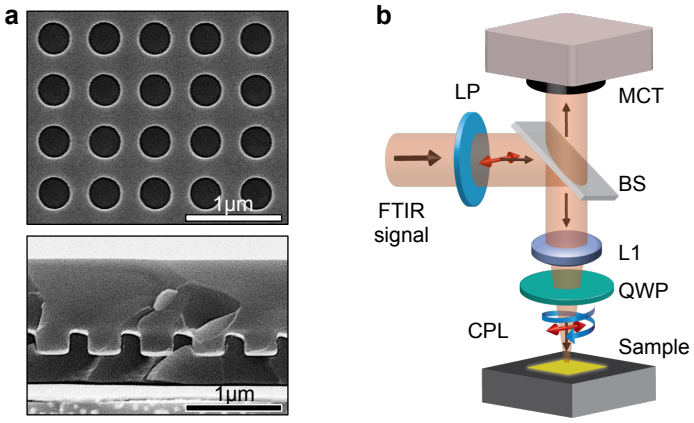

Figure 49: (a) Top view of one uncoated sample and cross section view of one polymer coated substrate embedding the chiral molecule. (b) Experimental configuration of the FTIR and Hyperion microscope to perform the optical characterization.

The dissymmetry factor is calculated as a function of the reflectance spectra for both RCP and LCP

$$g = 2\frac{R^{LCP} - R^{RCP}}{R^{LCP} + R^{RCP}}. \tag{42}$$

The first characterization is to obtain the response of a thing film of polymer embedding the chiral

molecules on a flat gold mirror, then the second is on a detuned cavity and the last one on a tuned substrate whose LSPR overlaps to that of the vibrational resonance of camphor. The dissymmetry in the reflectance for (d)-ccamphor and (s)-camphor is shown in Fig. 50, where clear dissymmetry ($g \sim 5 \times 10^{-3}$) in the reflectance spectra is observed around the LSP resonance, represented by the vertical line in Fig. 50. In contrast, same film deposited and characterized on a flat gold film and on same achiral plasmonic substrate detuned from the camphor absorption band do not show dissymmetry in the reflectance spectra, see Fig. 50. Therefore, it is the chiral near-field generated by the plasmon resonance, which further overlaps with the absorption band of the chiral analyte, that give rise a finite VCD signal since it is at resonance where the chiral near-field density is maximum.

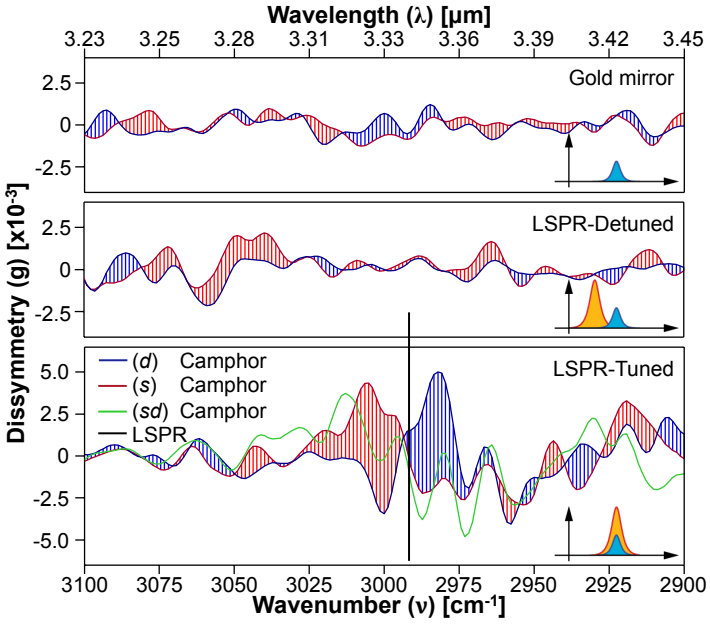

Figure 50: Dissymmetry factor for camphor (from top to bottom) on planar gold mirror, detuned and tuned achiral plasmonic substrate (also illustrated in the inset of each plot). Vertical line represents the LSPR of the tuned substrate.

Conventional VCD spectroscopy of 0.6 M camphor in liquid solvent [270] reveals path length normalized dissymmetry factors (g/μm) in the order of $2 \times 10^{-7} \mu\text{m}^{-1}$. In contrast, this

demonstration on similar concentration but much smaller effective path length of $\sim 1\ \mu$m, dissymmetry factors of $g \sim 5 \times 10^{-3} \mu\text{m}^{-1}$ is observed, with about four orders of magnitude enhancement in detection sensitivity (g/μm). According to our simulations, the achiral plasmonic structure offers superchiral near-field generation through the magnetic plasmon resonance. This is a limiting factor in the current demonstration since chiral molecular absorption rate is predominantly defined by electric dipole transitions. However it would be the perfect scenario for magnetic chiral molecules, which would experience much stronger interaction in this present geometry. Nevertheless, there are further geometries to explore that would lead to electric-field-dominated super chiral near field and, consequently, stronger CD signal could be achieved.

The understanding and control of the plasmon resonance using this cavity-coupling approach allows us to design plasmonic systems with novel characteristics. In addition, the straightforward nanoimprinting technique enables the mass production of such devices time and cost-efficiently, which allows the deployment of functional devices to the market. In this sense, I demonstrated how these simple hybrid systems, yet electromagnetically complex, are applied to biosensing of chiral and nonchiral analytes. The proof of concept presented here paves the road to potential applications outside the laboratory framework.

6. CONCLUSIONS AND FUTURE WORK

The extent of this work was to study the fundamental interaction between plasmonic and photonic resonances in complex electromagnetic environments. From multi-resonance interaction to unique control of the polarization state in the near field, the hybrid cavity-coupled plasmonic system provide unique opportunities to enable novel devices. In addition the fabrication method has an important merit since it does not rely on serial, time-consuming and expensive lithography techniques that impose high technological cost in the portrayed application framework. The nano imprinting lithography technique satisfies the technological constrains of conventional nano fabrication procedures and allows the mass production of high-quality devices as demonstrated in the course of this work and exploited by others. Therefore, the mutual exploitation of the system understanding along with the enabling technology translate in novel devices and applications with important technological impacts outside the laboratory domain.

The coherent interaction of cavity-plasmons, for example, would allow the dynamic excitation of plasmon modes hopping from the enhanced state to the suppressed state by only tuning the cavity phase. Although such a tuning is not possible for passive devices once the device is fabricated, in the presence of an active device that allows the refractive index modulation using an external stimuli this effect would be feasible. The active modulation would permit the dynamic tuning of the plasmonic resonance along with the intrinsic properties, such as absorption, field enhancement, polarization control and so forth.

In biosensing applications, there is further room for improvement and extend the current work presented here. The first sensing demonstrations were made using the incubation method. It means that the baseline of the device is taken first, then the corresponding analyte is incubated for an optimized time, and finally after removing the unreacted analyte and thoroughly dry the sample the response measurement is taken. This characterization method is subject to artificial shift solely by misplacing probing area, but it can be upgraded by incorporating a microfluidic channel system

that performs the full assay on-site on the same spot. Although this approach was utilized at the last stage of my work it opened the window to perform more complex assays that would add technological value to the straightforward biosensing application based on the discussed hybrid cavity-coupled plasmonic substrates. This multi-system integration would allow the fabrication of a point of care module that, for example, would run a particular pathogen profiling assay in region without access to analytical pathogen detection facilities. Therefore, I anticipate future work in this research line taking advantage of the cost relief given by the cheaper fabrication method.

These cavity-couple plasmonic system also allow the unique control and manipulation of the near field'polarization property. This is the case with superchiral light generation; in which the near field polarization exhibit higher phase twist compared to that of freespace CPL. This additional degree of freedom in the already engineered near-field will permit the detection of a certain analyte and characterize its chiral configuration. This concept was demonstrated on two chiral enantiomers of the same molecule using a single achiral substrate. The substrate supports both chiral near-field configurations which can be tuned on demand solely by the incident polarization. Hence, the same system can probe a certain molecule with CPL-like near-field and report in the far-field reflectance spectra this interaction. Considerable enhancement is observed in the dissymmetry factor from the measurement compared to conventional characterization methods, vibrational circular dichroism in this particular case. In addition, this concept can be translated to plasmonic resonances in the NIR to perform supramolecular chiral detection of proteins, for example, or other amino acids or DNA strands. In addition, when integrated with microfluidic channel systems along with a dynamic CPL polarizer the protein conformation dynamics could be observed in real time. This exciting field will not only permit the observation of molecular conformation change in real time but to study its biochemical interaction with drugs or other biomolecules. This synergetic interaction understanding will have profound effect in protein conformation related diseases, such as Alzheimer's disease, which is attributed to protein miss folding.

APPENDIX A: CHIRAL DENSITY DERIVATIONS

A.1. Derivation from original equation.

Lipkin introduced the following equation

$$\tilde{C}(\mathbf{r}) = \tfrac{1}{2}\varepsilon_0 \tilde{\mathbf{E}} \cdot \nabla \times \tilde{\mathbf{E}} + \tfrac{1}{2}\frac{1}{\mu_0}\tilde{\mathbf{B}} \cdot \nabla \times \tilde{\mathbf{B}} \tag{43}$$

of a conserved electromagnetic field quantity that later was attributed as the chiral density of the electromagnetic field. This vector equation is time averaged to reduce to $C(\mathbf{r}) = -\frac{1}{2}\varepsilon_0 \omega \,\mathrm{Im}(\mathbf{E}^* \cdot \mathbf{B})$ as follows. Here $\tilde{\mathbf{E}}$ and $\tilde{\mathbf{B}}$ are the real electric and magnetic vector fields, respectively, given as:

$$\tilde{\mathbf{E}}(\mathbf{r},t) = \mathrm{Re}\left[\mathbf{E}(\mathbf{r})e^{-i\omega t}\right] = \tfrac{1}{2}\left[\mathbf{E}(\mathbf{r})e^{-i\omega t} + \mathbf{E}^*(\mathbf{r})e^{i\omega t}\right] \tag{44}$$

$$\tilde{\mathbf{B}}(\mathbf{r},t) = \mathrm{Re}\left[\mathbf{B}(\mathbf{r})e^{-i\omega t}\right] = \tfrac{1}{2}\left[\mathbf{B}(\mathbf{r})e^{-i\omega t} + \mathbf{B}^*(\mathbf{r})e^{i\omega t}\right]. \tag{45}$$

Using Maxwell's equation on Eq. 44 and Eq. 45 we obtain:

$$\nabla \times \tilde{\mathbf{E}}(\mathbf{r},t) = -\frac{d}{dt}\tilde{\mathbf{B}}(\mathbf{r},t) = i\tfrac{1}{2}\omega\left[\mathbf{B}(\mathbf{r})e^{-i\omega t} - \mathbf{B}^*(\mathbf{r})e^{i\omega t}\right] \tag{46}$$

$$\nabla \times \tilde{\mathbf{B}}(\mathbf{r},t) = \mu_0\varepsilon_0\frac{d}{dt}\tilde{\mathbf{E}}(\mathbf{r},t) = -i\tfrac{1}{2}\mu_0\varepsilon_0\omega\left[\mathbf{E}(\mathbf{r})e^{-i\omega t} - \mathbf{E}^*(\mathbf{r})e^{i\omega t}\right] \tag{47}$$

Then, combining Eq. 44 in Eq. 46 and Eq. 45 in Eq. 47, and using the complex identities $a - a^* = i2\,\mathrm{Im}\,(a)$ and $a^* - a = -i2\,\mathrm{Im}\,(a)$, where a is a complex number, we have

$$\begin{aligned}
\tilde{\mathbf{E}} \cdot \nabla \times \tilde{\mathbf{E}} &= \tfrac{1}{2}\left[\mathbf{E}(\mathbf{r})e^{-i\omega t} + \mathbf{E}^*(\mathbf{r})e^{i\omega t}\right] \cdot i\tfrac{1}{2}\omega\left[\mathbf{B}(\mathbf{r})e^{-i\omega t} - \mathbf{B}^*(\mathbf{r})e^{i\omega t}\right] \\
&= i\tfrac{1}{4}\omega\left[\mathbf{E}\cdot\mathbf{B}e^{-i2\omega t} - \mathbf{E}\cdot\mathbf{B}^* + \mathbf{E}^*\cdot\mathbf{B} - \mathbf{E}^*\cdot\mathbf{B}^* e^{i2\omega t}\right] \\
&= i\tfrac{1}{4}\omega\left[i2\,\mathrm{Im}\,(\mathbf{E}^*\cdot\mathbf{B}) + \mathbf{E}\cdot\mathbf{B}e^{-i2\omega t} - \mathbf{E}^*\cdot\mathbf{B}^* e^{i2\omega t}\right]
\end{aligned}$$

and

$$\begin{aligned}
\tilde{\mathbf{B}} \cdot \nabla \times \tilde{\mathbf{B}} &= \tfrac{1}{2}\left[\mathbf{B}(\mathbf{r})e^{-i\omega t} + \mathbf{B}^*(\mathbf{r})e^{i\omega t}\right] \cdot -i\tfrac{1}{2}\mu_0\varepsilon_0\omega\left[\mathbf{E}(\mathbf{r})e^{-i\omega t} - \mathbf{E}^*(\mathbf{r})e^{i\omega t}\right] \\
&= -i\tfrac{1}{4}\mu_0\varepsilon_0\omega\left[\mathbf{B}\cdot\mathbf{E}e^{-i2\omega t} - \mathbf{B}\cdot\mathbf{E}^* + \mathbf{B}^*\cdot\mathbf{E} - \mathbf{B}^*\cdot\mathbf{E}^*e^{i2\omega t}\right] : \quad \mathbf{B}\cdot\mathbf{E} = \mathbf{E}\cdot\mathbf{B} \\
&= -i\tfrac{1}{4}\mu_0\varepsilon_0\omega\left[\mathbf{E}\cdot\mathbf{B}e^{-i2\omega t} - \mathbf{E}^*\cdot\mathbf{B} + \mathbf{E}\cdot\mathbf{B}^* - \mathbf{E}^*\cdot\mathbf{B}^*e^{i2\omega t}\right] \\
&= -i\tfrac{1}{4}\mu_0\varepsilon_0\omega\left[-i2\,\mathrm{Im}\left(\mathbf{E}^*\cdot\mathbf{B}\right) + \mathbf{E}\cdot\mathbf{B}e^{-i2\omega t} - \mathbf{E}^*\cdot\mathbf{B}^*e^{i2\omega t}\right]
\end{aligned}$$

Finally, combing these equation according to Eq. 43 and solving for the associated algebra, the final equation is obtained.

$$\begin{aligned}
C\left(\mathbf{r}\right) &= \tfrac{1}{2}\varepsilon_0\tilde{\mathbf{E}}\cdot\nabla\times\tilde{\mathbf{E}} + \tfrac{1}{2}\frac{1}{\mu_0}\tilde{\mathbf{B}}\cdot\nabla\times\tilde{\mathbf{B}} \\
&= i\tfrac{1}{2}\tfrac{1}{4}\varepsilon_0\omega\left[i2\,\mathrm{Im}\left(\mathbf{E}^*\cdot\mathbf{B}\right) + \mathbf{E}\cdot\mathbf{B}e^{-i2\omega t} - \mathbf{E}^*\cdot\mathbf{B}^*e^{i2\omega t}\right] \\
&\quad - i\tfrac{1}{2}\tfrac{1}{4}\varepsilon_0\omega\left[-i2\,\mathrm{Im}\left(\mathbf{E}^*\cdot\mathbf{B}\right) + \mathbf{E}\cdot\mathbf{B}e^{-i2\omega t} - \mathbf{E}^*\cdot\mathbf{B}^*e^{i2\omega t}\right] \\
&= i\tfrac{1}{2}\tfrac{1}{4}\varepsilon_0\omega\left[i2\,\mathrm{Im}\left(\mathbf{E}^*\cdot\mathbf{B}\right)\right] + i\tfrac{1}{2}\tfrac{1}{4}\varepsilon_0\omega\left[i2\,\mathrm{Im}\left(\mathbf{E}^*\cdot\mathbf{B}\right)\right] \\
&= -\tfrac{1}{4}\varepsilon_0\omega\,\mathrm{Im}\left(\mathbf{E}^*\cdot\mathbf{B}\right) - \tfrac{1}{4}\varepsilon_0\omega\,\mathrm{Im}\left(\mathbf{E}^*\cdot\mathbf{B}\right)
\end{aligned}$$

$$C\left(\mathbf{r}\right) = -\tfrac{1}{2}\varepsilon_0\omega\,\mathrm{Im}\left(\mathbf{E}^*\cdot\mathbf{B}\right) \tag{48}$$

A.2. Derivation of the chiral density for a dipole excited with free space planewave.

The chiral density is calculated for an electromagnetic planewave, propagating along the backward direction, $\mathbf{k} = -k\hat{\mathbf{k}}$, with electric and magnetic fields given by:

$$\mathbf{E}_i = \tfrac{1}{\sqrt{2}}E_0\left[\hat{x} + e^{i\Delta\phi}\hat{y}\right]e^{ikz} \tag{49}$$

$$\mathbf{B}_i = \frac{1}{\omega}\left[\mathbf{k}\times\mathbf{E}_i\right] = \frac{k}{\sqrt{2}\omega}E_0\left[e^{i\Delta\phi}\hat{x} - \hat{y}\right]e^{ikz}. \tag{50}$$

Notice that the time dependent factor $e^{-i\omega t}$ was omitted for clarity purposes. For a rotating dipole oriented in the xy plane, its dipole moment is given by $\mathbf{p} = i\mathbf{A}\mathbf{E}_i$, where $\mathbf{A}$ is the dipole polarizability matrix

$$\mathbf{A} = \begin{bmatrix} \alpha_x & 0 \\ 0 & \alpha_y \end{bmatrix} = \alpha_0 \begin{bmatrix} 1 & 0 \\ 0 & 1 \end{bmatrix},$$

which produces a dipole moment of the form $\mathbf{p} = ip_0\hat{\mathbf{p}}e^{-i\omega t}$ where $\hat{\mathbf{p}} = \frac{1}{\sqrt{2}}\left(\hat{x} + e^{i\Delta\phi}\hat{y}\right)e^{ikz}$, and $p_0 = \alpha_0 E_0$. The electromagnetic fields radiated by this dipole would be

$$\mathbf{E}_{RD} = i\frac{p_0}{4\pi\varepsilon_0}\frac{e^{ikr}}{r^3}\left\{k^2\left(\mathbf{r}\times\hat{\mathbf{p}}\right)\times\mathbf{r} + \left[\frac{3}{r^2}\mathbf{r}\left(\mathbf{r}\cdot\hat{\mathbf{p}}\right) - \hat{\mathbf{p}}\right](1-ikr)\right\} \tag{51}$$

$$\mathbf{B}_{RD} = i\xi\frac{c\mu_0 p_0 k^2}{4\pi}\frac{e^{ikr}}{r^2}\left(\mathbf{r}\times\hat{\mathbf{p}}\right)\left(1-\frac{1}{ikr}\right). \tag{52}$$

The chiral density for the combination of the incident field and the generated fields, $\mathbf{E} = \mathbf{E}_i + \mathbf{E}_{RD}$ and $\mathbf{B} = \mathbf{B}_i + \mathbf{B}_{RD}$ is

$$\begin{aligned} C\left(\mathbf{r}\right) &= -\tfrac{1}{2}\varepsilon_0\omega\,\mathrm{Im}\left(\mathbf{E}*\cdot\mathbf{B}\right) = -\tfrac{1}{2}\varepsilon_0\omega\,\mathrm{Im}\left(\left[\mathbf{E}_i+\mathbf{E}_{RD}\right]*\cdot\left[\mathbf{B}_i+\mathbf{B}_{RD}\right]\right) \\ &= -\tfrac{1}{2}\varepsilon_0\omega\,\mathrm{Im}\left(\mathbf{E}_i*\cdot\mathbf{B}_i + \mathbf{E}_i*\cdot\mathbf{B}_{RD} + \mathbf{E}_{RD}*\cdot\mathbf{B}_i + \mathbf{E}_{RD}*\cdot\mathbf{B}_{RD}\right) \\ &= C_i + C_{Ei-BRD} + C_{Ei-BRD} + C_{RD} \end{aligned}$$

Dipole E-field and dipole B-field

The derivation for C_{RD}, C_{Ei-BRD} and C_{Ei-BRD} are given bellow. That for C_i is already given in Chapter 3. Firstly, the chiral density of a stand-alone rotating dipole, which is given by Eq. 51 and Eq. 52 and Eq. 48 is as follows.

$$\begin{aligned} C_{RD}(\mathbf{r}) &= -\tfrac{1}{2}\varepsilon_0\omega\,\mathrm{Im}\left[\mathbf{E}^*\cdot\mathbf{B}\right] = -\tfrac{1}{2}\varepsilon_0\omega\xi E_0^2\left(\frac{\alpha_0 k}{4\pi}\right)^2\frac{c\mu_0}{\varepsilon_0 r^5} \\ &\mathrm{Im}\left[\left\{k^2\left[\left(\mathbf{r}\times\hat{\mathbf{p}}^*\right)\times\mathbf{r}\right]\cdot\left(\mathbf{r}\times\hat{\mathbf{p}}\right) + \left[\frac{3}{r^2}\mathbf{r}\left(\mathbf{r}\cdot\hat{\mathbf{p}}^*\right) - \hat{\mathbf{p}}^*\right]\cdot\left(\mathbf{r}\times\hat{\mathbf{p}}\right)(1+ikr)\right\}\left(1-\frac{1}{ikr}\right)\right] \end{aligned}$$

The following vector operations will be demonstrated in section A.3.

$$[(\mathbf{r}\times\hat{\mathbf{p}}^*)\times\mathbf{r}]\cdot(\mathbf{r}\times\hat{\mathbf{p}}) = r^2\det(\mathbf{r},\hat{\mathbf{p}},\hat{\mathbf{p}}^*) \tag{53}$$

$$\hat{\mathbf{p}}^*\cdot(\mathbf{r}\times\hat{\mathbf{p}}) = \det(\hat{\mathbf{p}}^*,\mathbf{r},\hat{\mathbf{p}}) \tag{54}$$

$$\mathbf{r}\,(\mathbf{r}\cdot\hat{\mathbf{p}}*)\cdot(\mathbf{r}\times\hat{\mathbf{p}}) = 0 \tag{55}$$

Solving Eq. 53 using $\hat{\mathbf{p}} = \frac{1}{\sqrt{2}}\left(\hat{x}+e^{i\Delta\phi}\hat{y}\right)$ and $\hat{\mathbf{p}}^* = \frac{1}{\sqrt{2}}\left(\hat{x}+e^{-i\Delta\phi}\hat{y}\right)$, we have:

$$\begin{aligned}
[(\mathbf{r}\times\hat{\mathbf{p}}^*)\times\mathbf{r}]\cdot(\mathbf{r}\times\hat{\mathbf{p}}) = r^2\det(\mathbf{r},\hat{\mathbf{p}},\hat{\mathbf{p}}^*) &= \frac{r^2}{2}\begin{vmatrix} x & y & z \\ 1 & e^{i\Delta\phi} & 0 \\ 1 & e^{-i\Delta\phi} & 0 \end{vmatrix} \\
&= z\frac{r^2}{2}\left(e^{-i\Delta\phi}-e^{i\Delta\phi}\right) \\
&= -ir^2z\sin(\Delta\phi)
\end{aligned}$$

$$\begin{aligned}
\hat{\mathbf{p}}^*\cdot(\mathbf{r}\times\hat{\mathbf{p}}) = \det(\hat{\mathbf{p}}^*,\mathbf{r},\hat{\mathbf{p}}) &= \frac{1}{2}\begin{vmatrix} 1 & e^{-i\Delta\phi} & 0 \\ x & y & z \\ 1 & e^{i\Delta\phi} & 0 \end{vmatrix} \\
&= -\frac{1}{2}ze^{i\Delta\phi}+\frac{1}{2}ze^{-i\Delta\phi} \\
&= -iz\sin(\Delta\phi)
\end{aligned}$$

Finally the chiral density of the rotating dipole is obtained by combined these vector operations and solving the algebra. The terms $\kappa = \frac{\alpha_0 k}{4\pi\varepsilon_0}$ is the normalized polarizability and chiral density of

circularly polarized light $C_0 = -\frac{\varepsilon_0 \omega E_0^2}{2c}$ are used to compress the notation.

$$\begin{aligned}
C_{RD}(\mathbf{r}) &= -\tfrac{1}{2}\varepsilon_0 \omega E_0^2 \xi \left(\frac{\alpha_0 k}{4\pi}\right)^2 \frac{c\mu_0}{\varepsilon_0 r^5} \operatorname{Im}\left[\left\{k^2\left(-ir^2 z \sin(\Delta\phi)\right) - \left(-iz\sin(\Delta\phi)\right)(1+ikr)\right\}\left(1-\frac{1}{ikr}\right)\right] \\
&= C_0 \xi \left(\frac{\alpha_0 k}{4\pi}\right)^2 \frac{c^2\mu_0}{\varepsilon_0 r^5} \operatorname{Im}\left[\left\{-ik^2 r^2 z \sin(\Delta\phi) + iz\sin(\Delta\phi) - krz\sin(\Delta\phi)\right\}\left(1-\frac{1}{ikr}\right)\right] \\
&= C_0 \xi \left(\frac{\alpha_0 k}{4\pi\varepsilon_0}\right)^2 \frac{1}{r^5} \operatorname{Im}\left[-ik^2 r^2 z + iz - krz + krz - \frac{z}{kr} - iz\right]\sin(\Delta\phi) \\
&= C_0 \xi \left(\frac{\alpha_0 k}{4\pi\varepsilon_0}\right)^2 \frac{1}{r^5} \operatorname{Im}\left[-ik^2 r^2 z - \frac{z}{kr}\right]\sin(\Delta\phi) \\
&= -C_0 \xi \kappa^2 k^2 \frac{z}{r^3}\sin(\Delta\phi)
\end{aligned}$$

Incident E-field and dipole B-field

$$\begin{aligned}
C_{\mathbf{E}i-\mathbf{B}RD}(\mathbf{r}) &= -\tfrac{1}{2}\varepsilon_0 \omega \operatorname{Im}\left[\mathbf{E}_i * \cdot \mathbf{B}_{RD}\right] \\
&= -\tfrac{1}{2}\varepsilon_0 \omega \tfrac{1}{\sqrt{2}} E_0^2 \xi \frac{c\mu_0 \alpha_0 k^2}{4\pi r^2} \operatorname{Im}\left[i\left[\hat{x} + e^{-i\Delta\phi}\hat{y}\right]\cdot(\mathbf{r}\times\hat{\mathbf{p}})\left(1-\frac{1}{ikr}\right)\right]
\end{aligned}$$

$$\mathbf{r}\times\hat{\mathbf{p}} = \tfrac{1}{\sqrt{2}}\begin{vmatrix} \hat{x} & \hat{y} & \hat{z} \\ x & y & z \\ 1 & e^{i\Delta\phi} & 0 \end{vmatrix} = \tfrac{1}{\sqrt{2}}\left[-ze^{i\Delta\phi}\hat{x} + z\hat{y} + \left(xe^{i\Delta\phi} - y\right)\hat{z}\right]$$

$$\left[\hat{x} + e^{-i\Delta\phi}\hat{y}\right]\cdot(\mathbf{r}\times\hat{\mathbf{p}}) = \tfrac{1}{\sqrt{2}}\left[-ze^{i\Delta\phi} + ze^{-i\Delta\phi}\right] = -i\tfrac{2}{\sqrt{2}} z\sin(\Delta\phi)$$

$$
\begin{aligned}
C_{\mathbf{E}i-\mathbf{B}RD}\left(\mathbf{r}\right) &= -\tfrac{1}{2}\varepsilon_0\omega\tfrac{1}{\sqrt{2}}E_0^2\xi\frac{c\mu_0\alpha_0k^2}{4\pi r^2}\,\mathrm{Im}\left[i\left(-i\frac{2}{\sqrt{2}}z\sin\left(\Delta\phi\right)\right)\left(1-\frac{1}{ikr}\right)\right] \\
&= C_0\xi\frac{c^2\mu_0\alpha_0k^2}{4\pi r^2}z\sin\left(\Delta\phi\right)\mathrm{Im}\left(1+\frac{i}{kr}\right) \\
&= C_0\xi\frac{\alpha_0k}{4\pi\varepsilon_0}\frac{z}{r^3}\sin\left(\Delta\phi\right) \\
&= C_0\xi\kappa\frac{z}{r^3}\sin\left(\Delta\phi\right)
\end{aligned}
$$

Dipole E-field and incident B-field

$$
\begin{aligned}
&C_{\mathbf{E}RD-\mathbf{B}i} = -\tfrac{1}{2}\varepsilon_0\omega\,\mathrm{Im}\left[\mathbf{E}_{RD}^{*}\cdot\mathbf{B}_i\right] \\
&= -\tfrac{1}{2}\varepsilon_0\omega\,\mathrm{Im}\left[-i\frac{p_0}{4\pi\varepsilon_0}\frac{1}{r^3}\left\{\begin{array}{c}k^2\left(\mathbf{r}\times\hat{\mathbf{p}}^{*}\right)\times\mathbf{r}+\\ \left[\frac{3}{r^2}\mathbf{r}\left(\mathbf{r}\cdot\hat{\mathbf{p}}^{*}\right)-\hat{\mathbf{p}}^{*}\right]\left(1+ikr\right)\end{array}\right\}\cdot\frac{k}{\sqrt{2}\omega}E_0\left[e^{i\Delta\phi}\hat{x}-\hat{y}\right]\right] \\
&= -\tfrac{1}{2}\varepsilon_0\omega\frac{\alpha_0}{4\pi\varepsilon_0}\frac{k}{\sqrt{2}\omega}E_0^2\frac{1}{r^3}\,\mathrm{Im}\left[-i\left\{\begin{array}{c}k^2\left[\left(\mathbf{r}\times\hat{\mathbf{p}}^{*}\right)\times\mathbf{r}\right]\cdot\left[e^{i\Delta\phi}\hat{x}-\hat{y}\right]+\\ \left[\frac{3}{r^2}\mathbf{r}\left(\mathbf{r}\cdot\hat{\mathbf{p}}^{*}\right)\cdot\left[e^{i\Delta\phi}\hat{x}-\hat{y}\right]-\hat{\mathbf{p}}^{*}\cdot\left[e^{i\Delta\phi}\hat{x}-\hat{y}\right]\right]\left(1+ikr\right)\end{array}\right\}\right]
\end{aligned}
$$

$$
\mathbf{r}\times\hat{\mathbf{p}}* = \frac{1}{\sqrt{2}}\begin{vmatrix}\hat{x} & \hat{y} & \hat{z}\\ x & y & z\\ 1 & e^{-i\Delta\phi} & 0\end{vmatrix} = -\tfrac{1}{\sqrt{2}}ze^{-i\Delta\phi}\hat{x}+\tfrac{1}{\sqrt{2}}z\hat{y}+\tfrac{1}{\sqrt{2}}\left(xe^{-i\Delta\phi}-y\right)\hat{z}
$$

$$
\begin{aligned}
(\mathbf{r}\times\hat{\mathbf{p}}*)\times\mathbf{r} &= \tfrac{1}{\sqrt{2}}\begin{vmatrix} \hat{x} & \hat{y} & \hat{z} \\ -ze^{-i\Delta\phi} & z & \left(xe^{-i\Delta\phi}-y\right) \\ x & y & z \end{vmatrix} \\
&= \tfrac{1}{\sqrt{2}}\left\{z^2-xye^{-i\Delta\phi}+y^2\right\}\hat{x}-\tfrac{1}{\sqrt{2}}\left\{-z^2e^{-i\Delta\phi}-x^2e^{-i\Delta\phi}+xy\right\}\hat{y} \\
&\quad+\tfrac{1}{\sqrt{2}}\left\{-yze^{-i\Delta\phi}-xz\right\}\hat{z}
\end{aligned}
$$

$$
\begin{aligned}
\left[(\mathbf{r}\times\hat{\mathbf{p}}*)\times\mathbf{r}\right]\cdot\left[e^{i\Delta\phi}\hat{x}-\hat{y}\right] &= \tfrac{1}{\sqrt{2}}\left\{z^2e^{i\Delta\phi}-xy+y^2e^{i\Delta\phi}\right\}+\tfrac{1}{\sqrt{2}}\left\{-z^2e^{-i\Delta\phi}-x^2e^{-i\Delta\phi}+xy\right\} \\
&= \tfrac{1}{\sqrt{2}}\left\{z^2e^{i\Delta\phi}-xy+y^2e^{i\Delta\phi}-z^2e^{-i\Delta\phi}-x^2e^{-i\Delta\phi}+xy\right\} \\
&= \tfrac{1}{\sqrt{2}}\left\{i2z^2\sin\left(\Delta\phi\right)+y^2e^{i\Delta\phi}-x^2e^{-i\Delta\phi}\right\}
\end{aligned}
$$

$$
\begin{aligned}
\mathbf{r}\left(\mathbf{r}\cdot\hat{\mathbf{p}}*\right)\cdot\left[e^{i\Delta\phi}\hat{x}-\hat{y}\right] &= \tfrac{1}{\sqrt{2}}\left(x+e^{-i\Delta\phi}y\right)\mathbf{r}\cdot\left[e^{i\Delta\phi}\hat{x}-\hat{y}\right] \\
&= \tfrac{1}{\sqrt{2}}\left(x+e^{-i\Delta\phi}y\right)\left(e^{i\Delta\phi}x-y\right) \\
&= \tfrac{1}{\sqrt{2}}\left(x^2e^{i\Delta\phi}-xy+xy-y^2e^{-i\Delta\phi}\right) \\
&= \tfrac{1}{\sqrt{2}}\left(x^2e^{i\Delta\phi}-y^2e^{-i\Delta\phi}\right)
\end{aligned}
$$

$$
\begin{aligned}
\hat{\mathbf{p}}*\cdot\left[e^{i\Delta\phi}\hat{x}-\hat{y}\right] &= \tfrac{1}{\sqrt{2}}\left(\hat{x}+e^{-i\Delta\phi}\hat{y}\right)\cdot\left[e^{i\Delta\phi}\hat{x}-\hat{y}\right] \\
&= \tfrac{1}{\sqrt{2}}\left(e^{i\Delta\phi}-e^{-i\Delta\phi}\right) \\
&= i\tfrac{2}{\sqrt{2}}\sin\left(\Delta\phi\right)
\end{aligned}
$$

$$C_{\mathbf{E}RD-\mathbf{B}i} = C_0 \frac{\alpha_0}{4\pi\varepsilon_0} \frac{1}{\sqrt{2}} \frac{1}{r^3} \operatorname{Im} \left[-i \left\{ \begin{array}{c} k^2 \frac{1}{\sqrt{2}} \left\{ i2z^2 \sin\Delta\phi + y^2 e^{i\Delta\phi} - x^2 e^{-i\Delta\phi} \right\} \\ + \frac{1}{\sqrt{2}} \left[\frac{3}{r^2} \left(x^2 e^{i\Delta\phi} - y^2 e^{-i\Delta\phi} \right) - i2\sin\Delta\phi \right] (1+ikr) \end{array} \right\} \right]$$

$$= -\tfrac{1}{2} C_0 \frac{\alpha_0}{4\pi\varepsilon_0} \frac{1}{r^3} \operatorname{Im} \left[\left\{ \begin{array}{c} -2k^2 z^2 \sin\Delta\phi + ik^2 y^2 e^{i\Delta\phi} - ik^2 x^2 e^{-i\Delta\phi} \\ + \left[\frac{3}{r^2} \left(x^2 e^{i\Delta\phi} - y^2 e^{-i\Delta\phi} \right) - i2\sin\Delta\phi \right] (i - kr) \end{array} \right\} \right]$$

$$= -\tfrac{1}{2} C_0 \frac{\alpha_0}{4\pi\varepsilon_0} \frac{1}{r^3} \operatorname{Im} \begin{bmatrix} -2k^2 z^2 \sin\Delta\phi + ik^2 y^2 \left(\cos\Delta\phi + i\sin\Delta\phi \right) \\ -ik^2 x^2 \left(\cos\Delta\phi - i\sin\Delta\phi \right) + +2\sin\Delta\phi + i2kr\sin\Delta\phi \\ \frac{3}{r^2} \left(ix^2 \left(\cos\Delta\phi + i\sin\Delta\phi \right) - iy^2 \left(\cos\Delta\phi - i\sin\Delta\phi \right) \right) \\ -\frac{3k}{r} \left(x^2 \left(\cos\Delta\phi + i\sin\Delta\phi \right) - y^2 \left(\cos\Delta\phi - i\sin\Delta\phi \right) \right) \end{bmatrix}$$

$$= -\tfrac{1}{2} C_0 \frac{\alpha_0}{4\pi\varepsilon_0} \frac{1}{r^3} \operatorname{Im} \begin{bmatrix} -2k^2 z^2 \sin\Delta\phi + k^2 \left(x^2 - y^2 \right) \sin\Delta\phi \\ -\frac{3}{r^2} \left(x^2 + y^2 \right) \sin\Delta\phi - \frac{3k}{r} \left(x^2 - y^2 \right) \cos\Delta\phi + 2\sin\Delta\phi \\ +ik^2 \left(y^2 - x^2 \right) \cos\Delta\phi + i\frac{3}{r^2} \left(x^2 - y^2 \right) \cos\Delta\phi \\ -i\frac{3k}{r} \left(x^2 + y^2 \right) \sin\Delta\phi + i2kr\sin\Delta\phi \end{bmatrix}$$

$$= \tfrac{1}{2} C_0 \kappa \frac{1}{r^3} \left[k \left(x^2 - y^2 \right) \cos\Delta\phi - \frac{3}{kr^2} \left(x^2 - y^2 \right) \cos\Delta\phi + \frac{3}{r} \left(x^2 + y^2 \right) \sin\Delta\phi - 2r\sin\Delta\phi \right]$$

$$= \tfrac{1}{2} C_0 \kappa \frac{1}{r^3} \left[\left\{ k - \frac{3}{kr^2} \right\} \left(x^2 - y^2 \right) \cos\Delta\phi + \left\{ \frac{3}{r} \left(x^2 + y^2 \right) - 2r \right\} \sin\Delta\phi \right]$$

A.3. Vector operations in determinant form.

For simplicity I will use Einstein summation convention. Let two arbitrary vectors $\mathbf{a}$ and $\mathbf{b}$, such

that their dot and cross product **c** are defined as follow:

$$\mathbf{a}\cdot\mathbf{b}=\sum_{i=1}^{3}a^ib^i\equiv a^ib^i$$

$$\mathbf{c}=\mathbf{a}\times\mathbf{b}=\begin{vmatrix}\hat{e}_1 & \hat{e}_2 & \hat{e}_3\\ a^1 & a^2 & a^3\\ b^1 & b^2 & b^3\end{vmatrix}=\sum_{i=1}^{3}\sum_{j=1}^{3}\sum_{j=2}^{3}\epsilon_{ijk}\hat{e}_ia^jb^k\equiv\epsilon_{ijk}a^jb^k\hat{e}_i.$$

where $\hat{e}_i$ is the unit vector along the i^{th} direction, and ϵ_{ijk} is the Levi-Civita operator with the properties: $\epsilon_{ijk}=+1$ if $(i,j,k)=(1,2,3),(2,3,1)$ or $(3,1,2)$, $\epsilon_{ijk}=-1$ if $(i,j,k)=(3,2,1),(1,3,2)$ or $(2,1,3)$, $\epsilon_{ijk}=0$ if $i=j,j=k$ or $k=i$ and $\varepsilon_{ijk}\varepsilon_{iml}=\delta_{jm}\delta_{kl}-\delta_{jl}\delta_{km}$. The vector equations are calculated.

$$\begin{aligned}[(\mathbf{r}\times\mathbf{p}^*)\times\mathbf{r}]&=\varepsilon_{ijk}r^jp^{k*}\varepsilon_{lim}r^m\hat{e}_l=\varepsilon_{ijk}\varepsilon_{iml}r^jp^{k*}r^m\hat{e}_l=(\delta_{jm}\delta_{kl}-\delta_{jl}\delta_{km})\,r^jp^{k*}r^m\hat{e}_l\\&=\delta_{jm}\delta_{kl}r^jp^{k*}r^m\hat{e}_l-\delta_{jl}\delta_{km}r^jp^{k*}r^m\hat{e}_l=r^mp^{l*}r^m\hat{e}_l-r^lp^{m*}r^m\hat{e}_l\end{aligned}$$

$$\begin{aligned}[(\mathbf{r}\times\mathbf{p}^*)\times\mathbf{r}]\cdot[\mathbf{r}\times\mathbf{p}]&=\left[r^mp^{l*}r^m\hat{e}_l-r^lp^{m*}r^m\hat{e}_l\right]\cdot[\varepsilon_{lqn}r^qp^n\hat{e}_l]\\&=\varepsilon_{lqn}r^mp^{l*}r^mr^qp^n-\varepsilon_{lqn}r^lp^{m*}r^mr^qp^n\\&=r^mr^m\varepsilon_{qnl}r^qp^np^{l*}-p^{m*}r^m\varepsilon_{qnl}r^qp^nr^l\\&=(\mathbf{r}\cdot\mathbf{r})\begin{vmatrix}r^1 & r^2 & r^3\\ p^1 & p^2 & p^3\\ p^{1*} & p^{2*} & p^{3*}\end{vmatrix}-(\mathbf{p}^*\cdot\mathbf{r})\begin{vmatrix}r^1 & r^2 & r^3\\ p^1 & p^2 & p^3\\ r^1 & r^2 & r^3\end{vmatrix}\\&=r^2\det(\mathbf{r},\mathbf{p},\mathbf{p}^*)-(\mathbf{p}^*\cdot\mathbf{r})\det(\mathbf{r},\mathbf{p},\mathbf{r})=r^2\det(\mathbf{r},\mathbf{p},\mathbf{p}^*)\end{aligned}$$

The determinant of a 3×3 matrix is zero if two rows are the same.

$$\mathbf{p}^* \cdot [\mathbf{r} \times \mathbf{p}] = \left(p^{i*}\hat{e}_i\right) \cdot \left(\varepsilon_{ijk} r^j p^k \hat{e}_i\right) = \varepsilon_{ijk} p^{i*} r^j p^k = \begin{vmatrix} p^{1*} & p^{2*} & p^{3*} \\ r^1 & r^2 & r^3 \\ p^1 & p^2 & p^3 \end{vmatrix} = \det\left(\mathbf{p}^*, \mathbf{r}, \mathbf{p}\right)$$

$$\begin{aligned} \mathbf{r}\left(\mathbf{r} \cdot \mathbf{p}^*\right) \cdot (\mathbf{r} \times \mathbf{p}) &= \left(r^i \hat{e}_i r^j p^{j*}\right) \cdot \left(\varepsilon_{klm} r^l p^m \hat{e}_k\right) = r^i r^j p^{j*} \varepsilon_{klm} r^l p^m \left(\hat{e}_i \cdot \hat{e}_k\right) \\ &= r^i r^j p^{j*} \varepsilon_{klm} r^l p^m \delta_{ik} = r^j p^{j*} \varepsilon_{ilm} r^i r^l p^m = \left(\mathbf{r} \cdot \mathbf{p}^*\right) \begin{vmatrix} r^1 & r^2 & r^3 \\ r^1 & r^2 & r^3 \\ p^1 & p^2 & p^3 \end{vmatrix} \\ &= \left(\mathbf{r} \cdot \mathbf{p}^*\right) \det\left(\mathbf{r}, \mathbf{r}, \mathbf{p}\right) = 0 \end{aligned}$$

APPENDIX B: MATERIALS AND METHODS FOR BIOSENSING

B.1. Sensing iron oxide nanoparticles and streptavidin.

Materials.

(+)-α-Lipoic Acid (LA), 1,4-Dithio-DL-threitol (DTT), 1-Ethyl-3-(3-dimethylaminopropyl) carbodiimide (EDC), N-Hydroxy-succinimide (NHS), streptavidin, bovine serum albumin (BSA), $FeCl_3.6H_2O$, $FeCl_2.4H_2O$, NH_4OH, hydrogen chloride (HCL), N,N'-Dicyclohexylcarbodiimide, tetrahydrofuran, ethyl acetate, hexane, poly(acrylic acid), pyridine, dimethylformamide, Biotin-PEG_{11}-NH_2, were used as received. Lipoic Acid conjugates were synthesized using NHS chemistry.

Iron oxide nanoparticle synthesis.

An iron solution consisting of $FeCl_3.6H_2O$ (0.62 g), $FeCl_2.4H_2O$ (0.32 g), H_2O (2 mL) and HCl (100 µL) was added to a 12% (v/v) aqueous solution of NH_4OH under mild mixing. The solution was allowed to mix for 30 seconds to allow for nucleation. Then poly(acrylic acid) (820 g) was dissolved in H_2O (15 mL) and added to the iron solution under rigorous mixing for one hour. The iron oxide nanoparticles (IONP) were purified via centrifugation (30 minutes, 4,000 rpm, three times) to remove large iron particles and with a KROS FLO filter (Spectrum Labs) to remove excess ammonium hydroxide. The nanoparticles size (80-100 nm) was determined by dynamic light scattering (Zetasizer Nano ZS, Malvern).

Lipoic acid-NHS synthesis.

N,N'-Dicyclohexylcarbodiimide (6.00 g) was dissolved in tetrahydrofuran (10 ml) and added slowly to a LA solution (5.00 g) and NHS (3.35 g) in tetrahydrofuran (150 ml) at 40 °C. The mixture was warmed to room temperature and stirred for 5 hours. The precipitate was removed by vacuum filtration and the solvent evaporated *in vacuo*. The crude product was re-dissolved in ethyl acetate (100 ml) and filtered once more by vacuum filtration. The product was recrystallized from

a solution of hot ethyl acetate/hexane (1:1 v/v) as a pale yellow solid (5.88 g, 80%). [1H NMR (400MHz, $CDCl_3$): ä(ppm) 3.58 (m,1H), 3.13 (m, 2H), 2.84 (s, 4H), 2.63 ((t, J)7.1 Hz, 2H), 2.50 (m, 1H), 1.99-1.46 (m, 7H)].

Lipoic acid-PEG_{11}-biotin synthesis.

Biotin-PEG_{11}-NH_2 (50 mg) and catalytic amounts of pyridine (10 µL) were added to Lipoic Acid-NHS (18.71 mg) in dry dimethylformamide (DMF) (2 ml). The mixture was stirred overnight at room temperature. The reaction mixture was then dried *in vacuo* and the resulting solid was re-dissolved in water to precipitate unreacted LA-NHS. The mixture was centrifuged and the supernatant was collected. The product was lyophilized and resulted in thick yellow oil.

B.2. Sensing dopamine with CNPs.

CNPs synthesis and sensor surface coating.

Two different CNPs formulations were prepared; CNP1 with $Ce4^+/Ce3^+ > 1$ and CNP2 with $Ce4^+/Ce3^+ < 1$. CNP1 was synthesized using thermo-hydrolysis method in which cerium nitrate salt precursor is mixed with NH_4OH to form CNP1. CNP2 was synthesized using wet chemical synthesis in which the cerium nitrate precursor was mixed with H_2O_2 to oxidize the particles. It has been previously noted that the CNPs prepared using $_2$ have more $Ce3^+$ compared to CNPs prepared using NH_4OH on its surface. Both synthesis methods produced very similar particle shape (spherical) and size (3-5 nm). The colloidal CNPs solution with $Ce4^+/Ce3^+ > 1$ is used to functionalize the surface of the sensor. Then the CNPs were stabilized in PVA before surface coating, for which a 500 µL PVA-CNPS solution is prepared based on 450 µL of CNPs and 50 µL of PVA at 50 µM concentration. The CNPs solution is drop casted on the surface and spin coated in two steps, 900 rpm for 10 s and 2000 rpm for 30s. This process is repeated eight times followed by convection oven baking at 60 °C for 1 hr.

In-situ UV-Visible spectroelectrochemistry.

Spectroelectrochemistry characterization was performed using a integrated assembly of UV/VIS spectrometer (Lambda 750S UV/Vis, Perkin Elmer) and a potentiostat (VSP, Bio-Logic SA). Sample was placed in an UV/Vis cuvette, 2 mm path length, with a Ag/AgCl reference electrode, a thin platinum mesh of 1x0.7 cm as working electrode and a thin platinum wire as counter electrode. Auto zero corrections were performed to eliminate the effects of all the electrodes inside the cuvette before running the experiments. The open circuit potentials were measured inside the cuvette by taking the measurements for 20 min until the value reached equilibrium. Chrono-amperometry was performed by applying a constant voltage for 3 min while UV-Visible spectrum was simultaneously recorded.

APPENDIX C: LIST OF PUBLICATIONS

[19] N. Otroshi, **A. Vázquez-Guardado**, S. Modak, D. Chanda and L. Tetard. *Nanoscale Infrared Chiroptical Sensing*. **(In preparation)**.

[18] S. Modak, A. Safaei, **A. Vázquez-Guardado**, D. Franklin, and D. Chanda, *Cavity Induced Light Funneling Through Subwavelength Apertures*. **(Under Review)**.

[17] **A. Vázquez-Guardado**, S. Barkam, M. Peppler, W. Dennis, S. Das, S. Seal and D. Chanda. *Nanostructured Enzyme-Free Plasmonic Biosensor for Dopamine Detection in Biological Fluids*. **(In preparation)**.

[16] S. Modak, A. Safaei, J. Lee, S. Chandra, D. Franklin, **A. Vázquez-Guardado** and D. Chanda, *Near-Zero Index Imprinted Surfaces for Frequency Selective Multi-Color Mid-Infrared Photon Detection at Room Temperature*. **(Under review)**.

[15] P. Gurturf, V. Krishnamurthi, **A. Vázquez-Guardado**, A. Banks, C. Haney, E. Waters, I. Kandela, T. Ray, J. Leshock, D. Chanda, and J. A. Rogers. *Advanced, Fully Implantable Optoelectronic Systems for Battery-Free, Multimodal Operation in Neuroscience Research*. **(Under review)**.

[14] N. Zin, K. McIntosh, S. Bakhshi, **A. Vázquez-Guardado**, T. Kho, K. Fong, M. Stocks, E. Franklin, and A. Blakers. *Polyimide for Silicon Solar Cells with Double-Sided Textured Pyramids*. **Solar Energy Materials and Solar Cells**. **(In Press)**.

[13] A. Safaei, **A. Vázquez-Guardado**, D. Franklin , M. Leuenberger, D. Chanda. *High-Efficiency Broadband Mid-Infrared Flat Lens*. **Advanced Optical Materials**, 1800216, 2018.

[12] **A. Vázquez-Guardado**, J. Boroumand, D. Franklin, and D. Chanda. *Broadband Angle Independent Anti-Reflection Coating on Nanostructured Light Trapping Solar Cells*, **Physical Review Materials**, 2, 035201, 2018.

[11] **A. Vázquez-Guardado** and D. Chanda. *Superchiral Light Generation on Degenerate Achiral Surfaces*, **Physical Review Letters**, 120(13): 137601, 2018.

[10] L. Lu, Z. Yang, K. Meacham, C. Cvetkovic, E. A. Corbin, **A. Vázquez-Guardado**, M. Xue, L. Yin, J. Boroumand, G. Pakeltis, T. Sang, K. J. Yu, D. Chanda, R. Bashir, R. W. Gereau, X. Sheng, and J. A. Rogers. *Biodegradable Monocrystalline Silicon Photovoltaic Microcells as Power Supplies for Transient Biomedical Implants*, **Advanced Energy Materials**, 1703035, 2018.

[9] L. Lu, P. Gutruf, L. Xia, D. L. Bhatti, X. Wang, **A. Vázquez-Guardado**, N. Xin, X. Shen, T. Sang, R. Ma, G. Pakeltis, G. Sobczak, H. Zhang, D-O. Seo, M. Xue, L. Yin, D. Chanda, X. Sheng, M. R. Bruchas, and J. A. Rogers. *Wireless optoelectronic photometers for monitoring neuronal dynamics in the deep brain*, **Proceedings of the National Academy of Science**, 115(7):E1374-E1383, 2018.

[8] A. Safaei, S. Chandra, **A. Vázquez-Guardado**, J. Calderon, D. Franklin, L. Tetard, L. Zhai, M. N. Leuenberger, and D. Chanda. *Dynamically Tunable Extraordinary Light Absorption in Monolayer Graphene*, **Physical Review B**, 96(16): 165431, 2017.

[7] **A. Vázquez-Guardado**, A. Smith, W. Wilson, J. Ortega, J. M. Perez, and D. Chanda. *Hybrid Cavity-Coupled Plasmonic Biosensors for Low Concentration, Label-Free and Selective Biomolecular Detection*, **Optics Express**, 24(22): 25785-25796, 2016.

[6] J. Boroumand, S. Das, **A. Vázquez-Guardado**, D. Franklin, and D. Chanda. *Unified Electromagnetic -Electronic Design of Light Trapping Silicon Solar Cells*, **Scientific Reports**, 6: 31013, 2016.

[5] **A. Vázquez-Guardado**, M. Money, N. McKinney, and D. Chanda. *Multi-Spectral Infrared Spectroscopy for Robust Plastic Identification*, **Applied Optics**, 54(24): 7396-7405, 2015.

[4] D. Franklin, Y. Chen, **A. Vázquez-Guardado**, S. Modak, J. Boroumand, D. Xu, S. T. Wu, and D. Chanda. *Polarization-independent actively tunable colour generation on imprinted plasmonic surfaces*, **Nature Communications**, 6: 7337, 2015. **(Featured Article)**

[3] **A. Vázquez-Guardado**, A. Safaei, S. Modak, D. Franklin, and D. Chanda. *Hybrid Coupling Mechanism in a System Supporting High Order Diffraction, Plasmonic, and Cavity Resonances*, **Physcal Review Letters**, 113(26): 263902, 2014.

[2] L. Gao, K. Shigeta, **A. Vázquez-Guardado**, C. J. Progler, G. R. Bogart, J. A. Rogers, and D. Chanda. *Nanoimprinting Techniques for Large-Area Three-Dimensional Negative Index Metamaterials with Operation in the Visible and Telecom Bands*, **ACS Nano**, 8(6): 5535-5542, 2014.

[1] L. Gao, Y. Kim, **A. Vázquez-Guardado**, K. Shigeta, S. Hartanto, D. Franklin, Christopher J. Progler, G. R. Bogart, J. A. Rogers, and D. Chanda. *Materials Selections and Growth Conditions for Large-Area, Multilayered, Visible Negative Index Metamaterials Formed by Nanotransfer Printing*, **Advanced Optical Materials**, 2(3): 256-261, 2014. **(Cover Article)**

LIST OF REFERENCES

[1] A Hayat, D Andreescu, G Bulbul, and S Andreescu. Redox reactivity of cerium oxide nanoparticles against dopamine. *Journal of Colloid And Interface Science*, 418:240–245, 2014.

[2] A Sommerfeld. Ueber die Fortpflanzung elektrodynamischer Wellen längs eines Drahtes. *Annalen der Physik*, 303(2):233–290, 1899.

[3] J Zenneck. Über die Fortpflanzung ebener elektromagnetischer Wellen längs einer ebenen Leiterfläche und ihre Beziehung zur drahtlosen Telegraphie. *Annalen der Physik*, 328(10):846–866, 1907.

[4] R W Wood. On a Remarkable Case of Uneven Distribution of Light in a Diffraction Grating Spectrum. *Proceedings of the Physical Society of London*, 18(1):269–275, 1902.

[5] U Fano. The Theory of Anomalous Diffraction Gratings and of Quasi-Stationary Waves on Metallic Surfaces (Sommerfeld's Waves). *JOSA*, 31(3):213–222, 1941.

[6] R H Ritchie. Plasma Losses by Fast Electrons in Thin Films. *Phys.Rev.*, 106(5):874–881, 1957.

[7] R H Ritchie, E T Arakawa, J J Cowan, and R N Hamm. Surface-plasmon resonance effect in grating diffraction. *Physical Review Letters*, 21(22):1530–1533, 1968.

[8] E Stern and R Ferrell. Surface Plasma Oscillations of a Degenerate Electron Gas. *Physical Review Letters*, 120(1):130–136, 1960.

[9] C Powell and J Swan. Origin of the Characteristic Electron Energy Losses in Aluminum. *Physical Review Letters*, 115(4):869–875, 1959.

[10] E Kretschmann and H Raether. *Radiative Decay of Non Radiative Surface Plasmons Excited by Light*. *Zeitschrift für Naturforschung*, 23A:2135–2136, 1968.

[11] A Otto. Excitation of nonradiative surface plasma waves in silver by the method of frustrated total reflection. *Zeitschrift für Physik A Hadrons and nuclei*, 216(4):398–410, 1968.

[12] R Ferrell. Predicted Radiation of Plasma Oscillations in Metal Films. *Physical Review Letters*, 111(5):1214–1222, 1958.

[13] J Crowell and R H Ritchie. Surface-Plasmon Effect in the Reflectance of a Metal. *Journal of the Optical Society of America*, 60:794–799, 1970.

[14] H Raether. *Surface Plasmons on Smooth and Rough Surfaces and on Gratings*. Springer-Verlag, Berlin, 1988.

[15] G Goubau. Surface waves and their application to transmission lines. *Journal of Applied Physics*, 21(11):1119, 1950.

[16] P Berini. Plasmon-polariton waves guided by thin lossy metal films of finite width: Bound modes of symmetric structures. *Physical Review B*, 61(15):10484–10503, 2000.

[17] A D Boardman. *Electromagnetic Surface Modes*. John Wiley & Sons, 1982.

[18] S A Maier. *Plasmonics*. fundamentals and applications. Springer Verlag, 1 edition, 2007.

[19] H Guerboukha, G Yan, O Skorobogata, and M Skorobogatiy. Silk Foam Terahertz Waveguides. *Advanced Optical Materials*, 2(12):1181–1192, 2014.

[20] R Wannemacher. Plasmon-supported transmission of light through nanometric holes in metallic thin films. *Optics Communications*, 195(1):107–118, 2001.

[21] C Sonnichsen, A C Duch, G Steininger, M Koch, G Von Plessen, and J Feldmann. Launching surface plasmons into nanoholes in metal films. *Applied Physics Letters*, 76(2):140–142, 2000.

[22] C L Haynes, A D McFarland, L L Zhao, R P Van Duyne, G C Schatz, L Gunnarsson, J Prikulis, B Kasemo, and M Käll. Nanoparticle Optics: The Importance of Radiative Dipole Coupling in Two-Dimensional Nanoparticle Arrays. *The Journal of Physical Chemistry B*, 107(30):7337–7342, 2003.

[23] J J Mock, D R Smith, and S Schultz. Local Refractive Index Dependence of Plasmon Resonance Spectra from Individual Nanoparticles. *Nano Letters*, 3(4):485–491, 2003.

[24] M Meier, A Wokaun, and P F Liao. Enhanced fields on rough surfaces: dipolar interactions among particles of sizes exceeding the Rayleigh limit. *Journal of the Optical Society of America*, 2(6):931–949, 1985.

[25] M Gustav. Beiträge zur Optik trüber Medien, speziell kolloidaler Metallösungen. *Annalen der Physik*, 330(3):377–445, 1908.

[26] Jackson, J D. *Classical Electrodynamics, 3rd Ed.* John Wiley & Sons, 3 edition, 2007.

[27] L Novotny and Hecht B. *Principles of nano-optics*. Cambridge University Press, 1 edition, 2006.

[28] K T Carron, H W Lehmann, W Fluhr, M Meier, and A Wokaun. Resonances of two-dimensional particle gratings in surface-enhanced Raman scattering. *Journal of the Optical Society of America*, 3(3):430–440, 1986.

[29] L Scarabelli, M Coronado-Puchau, J J Giner-Casares, J Langer, and L M Liz-Marzán. Monodisperse Gold Nanotriangles: Size Control, Large-Scale Self-Assembly and Performance in Surface Enhanced Raman Scattering. *ACS Nano*, 8(6):5833–5842, 2014.

[30] GV P Kumar. Plasmonic nano-architectures for surface enhanced Raman scattering: a review. *Journal of Nanophotonics*, 6(1):064503, 2012.

[31] T Utikal, T Zentgraf, T Paul, C Rockstuhl, F Lederer, M Lippitz, and H Giessen. Towards the Origin of the Nonlinear Response in Hybrid Plasmonic Systems. *Physical Review Letters*, 106(13):133901, 2011.

[32] I Rukhlenko, A Pannipitiya, M Premaratne, and G Agrawal. Exact dispersion relation for nonlinear plasmonic waveguides. *Physical Review B*, 84(11):113409, 2011.

[33] M Kauranen and A V Zayats. Nonlinear plasmonics. *Nature Photonics*, 6(11):737–748, 2012.

[34] Y Ge and B Kang. Surface plasmon resonance scattering and absorption of biofunctionalized gold nanoparticles for targeted cancer imaging and laser therapy. *Science China Technological Sciences*, 54(9):2358–2362, 2011.

[35] D K Roper, W Ahn, and M Hoepfner. Microscale Heat Transfer Transduced by Surface Plasmon Resonant Gold Nanoparticles. *Journal of Physical Chemistry C*, 111(9):3636–3641, 2007.

[36] E A Hawes, J T Hastings, C Crofcheck, and M P Mengüç. Spectrally selective heating of nanosized particles by surface plasmon resonance. *Journal of Quantitative Spectroscopy and Radiative Transfer*, 104(2):199–207, 2007.

[37] A Malloy. Count, size and visualize nanoparticles. *Materials Today*, 14(4):170–173, 2011.

[38] V Sokolova, A-K Ludwig, S Hornung, O Rotan, P A Horn, M Epple, and B Giebel. Characterisation of exosomes derived from human cells by nanoparticle tracking analysis and scanning electron microscopy. *Colloids and Surfaces B: Biointerfaces*, 87(1):146–150, 2011.

[39] Y Li, H J Lee, and R M Corn. Fabrication and characterization of RNA aptamer microarrays for the study of protein-aptamer interactions with SPR imaging. *Nucleic Acids Research*, 34(22):6416–6424, 2006.

[40] S Kawata, Y Inouye, and P Verna. Plasmonics for near-field nano-imaging and superlensing. *Nature Photonics*, 3(7):388–394, 2009.

[41] A Tittl, H Giessen, and N Liu. Plasmonic gas and chemical sensing. *Nanophotonics*, 3(3):157–180, 2014.

[42] D Nau, A Seidel, R B Orzekowsky, S H Lee, S Deb, and H Giessen. Hydrogen sensor based on metallic photonic crystal slabs. *OPTICS LETTERS*, 35(18):3150–3152, 2010.

[43] T Lang, T Hirsch, C Fenzl, F Brandl, and O S Wolfbeis. Surface Plasmon Resonance Sensor for Dissolved and Gaseous Carbon Dioxide. *Analytical Chemistry*, 84(21):9085–9088, 2012.

[44] L E Kreno, J T Hupp, and R P Van Duyne. Metal–Organic Framework Thin Film for Enhanced Localized Surface Plasmon Resonance Gas Sensing. *Analytical Chemistry*, 82(19):8042–8046, 2010.

[45] D G Zhu and M C Petty. An optical sensor for nitrogen dioxide based on a copper phthalocyanine langmuir-blodgett film. *Sensors and Actuators B*, 2:265–269, 2001.

[46] D Sil, K D Gilroy, A Niaux, A Boulesbaa, S Neretina, and E Borguet. Seeing Is Believing: Hot Electron Based Gold Nanoplasmonic Optical Hydrogen Sensor. *ACS Nano*, page 140729085733001, 2014.

[47] J Homola. Surface plasmon resonance sensors for detection of chemical and biological species. *Chemical Reviews*, 108(2):462–493, 2008.

[48] L B Sagle, L K Ruvuna, J A Ruemmele, and R P Van Duyne. Advances in localized surface plasmon resonance spectroscopy biosensing. *Nanomedicine*, 6(8):1447–1462, 2011.

[49] E Hendry, T Carpy, J Johnston, M Popland, R V Mikhaylovskiy, A J Lapthorn, S M Kelly, L D Barron, N Gadegaard, and M Kadodwala. Ultrasensitive detection and characterization of biomolecules using superchiral fields. *Nature Nanotechnology*, 5(11):783–787, 2010.

[50] C Escobedo, A G Brolo, R Gordon, and D Sinton. Optofluidic Concentration: Plasmonic Nanostructure as Concentrator and Sensor. *Nano Letters*, 12(3):1592–1596, 2012.

[51] J N Anker, W P Hall, O. Lyandres, N C Shah, J Zhao, and R P Van Duyne. Biosensing with plasmonic nanosensors. *Nature materials*, 7(6):442–453, 2008.

[52] A J Haes and R P Van Duyne. A Nanoscale Optical Biosensor: Sensitivity and Selectivity of an Approach Based on the Localized Surface Plasmon Resonance Spectroscopy of Triangular Silver Nanoparticles. *Journal of the American Chemical Society*, 124(35):10596–10604, 2002.

[53] J C Riboh, A J Haes, A D McFarland, C Ranjit Yonzon, and R P Van Duyne. A Nanoscale Optical Biosensor: Real-Time Immunoassay in Physiological Buffer Enabled by Improved Nanoparticle Adhesion. *The Journal of Physical Chemistry B*, 107(8):1772–1780, 2003.

[54] Z Altintas, Y Uludag, Y Gurbuz, and I Tothill. Development of surface chemistry for surface plasmon resonance based sensors for the detection of proteins and DNA molecules. *Analytica Chimica Acta*, 712:138–144, 2012.

[55] S A Maier and H A Atwater. Plasmonics: Localization and guiding of electromagnetic energy in metal/dielectric structures. *Journal of Applied Physics*, 98(1):011101, 2005.

[56] K F MacDonald, Z L Sámson, M I Stockman, and N I Zheludev. Ultrafast active plasmonics. *Nature Photonics*, 3(1):55–58, 2008.

[57] W L Barnes, A Dereux, and T W Ebbesen. Surface plasmon subwavelength optics. *Nature*, 424:824–830, 2003.

[58] S J Tan, L Zhang, D Zhu, X Ming Goh, Y M Wang, K Kumar, C-W Qiu, and J K W Yang. Plasmonic Color Palettes for Photorealistic Printing with Aluminum Nanostructures. *Nano Letters*, 14(7):4023–4029, 2014.

[59] K Kumar, H Duan, R S Hegde, S C W Koh, J N Wei, and J K W Yang. Printing colour at the optical diffraction limit. *Nature Nanotechnology*, 7(9):557–561, 2012.

[60] D Franklin, Y Chen, A Vázquez-Guardado, S Modak, J Boroumand, D Xu, S-T Wu, and D Chanda. Polarization-independent actively tunable colour generation on imprinted plasmonic surfaces. *Nature Communications*, 6:7337, 2015.

[61] S Yokogawa, S P Burgos, and H A Atwater. Plasmonic Color Filters for CMOS Image Sensor Applications. *Nano Letters*, 12(8):4349–4354, 2012.

[62] Q Chen, D Chitnis, K Walls, T D Drysdale, S Collins, and D R S Cumming. CMOS Photodetectors Integrated With Plasmonic Color Filters. *Photonics Technology Letters, IEEE*, 24(3):197–199, 2012.

[63] T Xu, Y-K Wu, X Luo, and L J Guo. Plasmonic nanoresonators for high-resolution colour filtering and spectral imaging. *Nature Communications*, 1(5):59–5, 2010.

[64] P V Tuong, V D Lam, J W Park, E H Choi, S A Nikitov, and Y P Lee. Perfect-absorber metamaterial based on flower-shaped structure. *Photonics and Nanostructures - Fundamentals and Applications*, 11(1):89–94, 2013.

[65] M A Kats, D Sharma, J Lin, P Genevet, R Blanchard, Z Yang, M M Qazilbash, D N Basov, S Ramanathan, and F Capasso. Ultra-thin perfect absorber employing a tunable

phase change material. *Applied Physics Letters*, 101(22):221101, 2012.

[66] S Butun and K Aydin. Structurally tunable resonant absorption bands in ultrathin broadband plasmonic absorbers. *Optics Express*, 22(16):19457–19468, 2014.

[67] X Liu, T Starr, A F Starr, and W J Padilla. Infrared Spatial and Frequency Selective Metamaterial with Near-Unity Absorbance. *Physical Review Letters*, 104(20):207403, 2010.

[68] C Argyropoulos, K Q Le, N Mattiucci, G D'Aguanno, and A Alù. Broadband absorbers and selective emitters based on plasmonic Brewster metasurfaces. *Physical Review B*, 87(20):205112, 2013.

[69] W Ma, Y Wen, and X Yu. Broadband metamaterial absorber at mid-infrared using multiplexed cross resonators. *Optics Express*, 21(25):30724–30730, 2013.

[70] T Cao, C-W Wei, R E Simpson, L Zhang, and M J Cryan. Broadband Polarization-Independent Perfect Absorber Using a Phase-Change Metamaterial at Visible Frequencies. *Scientific reports*, 4, 2014.

[71] K Aydin, V E Ferry, R M Briggs, and H A Atwater. Broadband polarization-independent resonant light absorption using ultrathin plasmonic super absorbers. *Nature Communications*, 2:517, 2011.

[72] D Ji, H Song, X Zeng, H Hu, K Liu, N Zhang, and Q Gan. Broadband absorption engineering of hyperbolic metafilm patterns. *Scientific reports*, 4, 2014.

[73] S Mukherjee, F Libisch, N Large, O Neumann, L V Brown, J Cheng, J B Lassiter, E A Carter, P Nordlander, and N J Halas. Hot Electrons Do the Impossible: Plasmon-Induced Dissociation of H2 on Au. *Nano Letters*, 13(1):240–247, 2013.

[74] C Clavero. Plasmon-induced hot-electron generation at nanoparticle/metal-oxide interfaces for photovoltaic and photocatalytic devices. *Nature Photonics*, 8(2):95–103, 2014.

[75] T W Ebbesen, H J Lezec, H F Ghaemi, T Thio, and P A Wolff. Extraordinary optical transmission through sub-wavelength hole arrays. *Nature*, 391(6668):667–669, 1998.

[76] L Martín-Moreno, F García-Vidal, H Lezec, K Pellerin, T Thio, J Pendry, and T Ebbesen. Theory of Extraordinary Optical Transmission through Subwavelength Hole Arrays. *Physical Review Letters*, 86(6):1114–1117, 2001.

[77] Y Liang, W Peng, R Hu, and L Xie. Extraordinary optical properties in the subwavelength metallodielectric free-standing grating. *Optics Express*, 22(16):19484–19494, 2014.

[78] Y-J Bao, R-W Peng, D-J Shu, M Wang, X Lu, J Shao, W Lu, and N-B Ming. Role of Interference between Localized and Propagating Surface Waves on the Extraordinary Optical Transmission Through a Subwavelength-Aperture Array. *Physical Review Letters*, 101(8):087401, 2008.

[79] S Enoch, G Tayeb, P Sabouroux, N Guérin, and P Vincent. A Metamaterial for Directive Emission. *Physical Review Letters*, 89(21):213902, 2002.

[80] S Enoch, J J Simon, L Escoubas, Z Elalmy, F Lemarquis, P Torchio, and G Albrand. Simple layer-by-layer photonic crystal for the control of thermal emission. *Applied Physics Letters*, 86(26):261101, 2005.

[81] K Ikeda, H T Miyazaki, T Kasaya, K Yamamoto, Y Inoue, K Fujimura, T Kanakugi, M Okada, K Hatade, and S Kitagawa. Controlled thermal emission of polarized infrared waves from arrayed plasmon nanocavities. *Applied Physics Letters*, 92(2):021117, 2008.

[82] D Vercruysse, X Zheng, Y Sonnefraud, N Verellen, G Di Martino, L Lagae, G A E Vandenbosch, V V Moshchalkov, S A Maier, and P Van Dorpe. Directional fluorescence emission by individual V-antennas explained by mode expansion. *ACS Nano*, 8(8):8232–8241, 2014.

[83] R-M Ma, S Ota, Y Li, S Yang, and X Zhang. Explosives detection in a lasing plasmon nanocavity. *Nature Nanotechnology*, 9(8):600–604, 2014.

[84] R F Oulton, V J Sorger, T Zentgraf, R-M Ma, C Gladden, L Dai, G Bartal, and X Zhang. Plasmon lasers at deep subwavelength scale. *Nature*, 461(7264):629–632, 2009.

[85] A Yang, Z Li, M P Knudson, A J Hryn, W Wang, K Aydin, and T W Odom. Unidirectional Lasing from Template-Stripped Two-Dimensional Plasmonic Crystals. *ACS Nano*,

9(12):11582–11588, 2015.

[86] A Yang, T B Hoang, M Dridi, C Deeb, M H Mikkelsen, G C Schatz, and T W Odom. Real-time tunable lasing from plasmonic nanocavity arrays. *Nature Communications*, 6:1–7, 2015.

[87] W Zhou, M Dridi, J Y Suh, C H Kim, D T Co, M R Wasielewski, G C Schatz, and T W Odom. Lasing action in strongly coupled plasmonic nanocavity arrays. *Nature Nanotechnology*, 8(7):506–511, 2013.

[88] B Frank, X Yin, M Schäferling, J Zhao, S M Hein, P V Braun, and H Giessen. Large-Area 3D Chiral Plasmonic Structures. *ACS Nano*, 7(7):6321–6329, 2013.

[89] N Meinzer, E Hendry, and W L Barnes. Probing the chiral nature of electromagnetic fields surrounding plasmonic nanostructures. *Physical Review B*, 88(4):041407, 2013.

[90] V K Valev, J J Baumberg, C Sibilia, and T Verbiest. Chirality and Chiroptical Effects in Plasmonic Nanostructures: Fundamentals, Recent Progress, and Outlook. *Advanced Materials*, 25(18):2517–2534, 2013.

[91] A García-Etxarri and J A Dionne. Surface-enhanced circular dichroism spectroscopy mediated by nonchiral nanoantennas. *Physical Review B*, 87(23):235409, 2013.

[92] M Schäferling, D Dregely, M Hentschel, and H Giessen. Tailoring Enhanced Optical Chirality: Design Principles for Chiral Plasmonic Nanostructures. *Physical Review X*, 2(3):031010, 2012.

[93] N A Abdulrahman, Z Fan, T Tonooka, S M Kelly, N Gadegaard, E Hendry, A O Govorov, and M Kadodwala. Induced Chirality through Electromagnetic Coupling between Chiral Molecular Layers and Plasmonic Nanostructures. *Nano Letters*, 12(2):977–983, 2012.

[94] M Decker, M W Klein, M Wegener, and S Linden. Circular dichroism of planar chiral magnetic metamaterials. *OPTICS LETTERS*, 32(7):856–858, 2007.

[95] M Decker, M Ruther, C E Kriegler, J Zhou, C M Soukoulis, S Linden, and M Wegener. Strong optical activity from twisted-cross photonic metamaterials. *OPTICS LETTERS*,

34(16):2501–2503, 2009.

[96] Abraham Vázquez-Guardado and Debashis Chanda. Superchiral Light Generation on Degenerate Achiral Surfaces. *Physical Review Letters*, 129:137601, 2018.

[97] M Schäferling, N Engheta, H Giessen, and T Weiss. Reducing the Complexity: Enantioselective Chiral Near-Fields by Diagonal Slit and Mirror Configuration. *ACS Photonics*, pages acsphotonics.6b00147–9, 2016.

[98] X Tian, Y Fang, and M Sun. Formation of Enhanced Uniform Chiral Fields in Symmetric Dimer Nanostructures. *Scientific reports*, 5(1):17534–12, 2015.

[99] Y Liu, W Zhao, Y Ji, R Y Wang, X Wu, and X D Zhang. Strong superchiral field in hot spots and its interaction with chiral molecules. *EPL (Europhysics Letters)*, 110(1):17008–7, 2015.

[100] M Schäferling, X Yin, N Engheta, and H Giessen. Helical Plasmonic Nanostructures as Prototypical Chiral Near-Field Sources. *ACS Photonics*, 1(6):530–537, 2014.

[101] SJ Yoo, M Cho, and Q-H Park. Globally enhanced chiral field generation by negative-index metamaterials. *Physical Review B*, 89(16):161405–5, 2014.

[102] T J Davis and E Hendry. Superchiral electromagnetic fields created by surface plasmons in nonchiral metallic nanostructures. *Physical Review B*, 87(8):085405, 2013.

[103] M Schäferling, X Yin, and H Giessen. Formation of chiral fields in a symmetric environment. *Optics Express*, 20(24):26326–26336, 2012.

[104] E Hendry, R V Mikhaylovskiy, L D Barron, M Kadodwala, and T J Davis. Chiral Electromagnetic Fields Generated by Arrays of Nanoslits. *Nano Letters*, 12:3640–3644, 2012.

[105] C García-Meca, R Ortuño, F J Rodríguez-Fortuño, J Martí, and A Martínez. Negative refractive index metamaterials aided by extraordinary optical transmission. *Optics Express*, 17(8):6026–6031, 2009.

[106] A Mary, S Rodrigo, F García-Vidal, and L Martín-Moreno. Theory of Negative-Refractive-Index Response of Double-Fishnet Structures. *Physical Review Letters*, 101(10):103902–4,

2008.

[107] J Valentine, S Zhang, T Zentgraf, E Ulin-Avila, D A Genov, G Bartal, and X Zhang. Three-dimensional optical metamaterial with a negative refractive index. *Nature*, 455(7211):376–379, 2008.

[108] A V Kildishev, W Cai, U K Chettiar, H-K Yuan, A K Sarychev, V P Drachev, and V M Shalaev. Negative refractive index in optics of metal-dielectric composites. *Journal of the Optical Society of America*, 23(3):423–433, 2006.

[109] S A Ramakrishna. Physics of negative refractive index materials. *Reports on Progress in Physics*, 68:449–521, 2005.

[110] L Gao, Y Kim, A Vázquez-Guardado, K Shigeta, S Hartanto, D Franklin, C J Progler, G R Bogart, J A Rogers, and D Chanda. Materials Selections and Growth Conditions for Large-Area, Multilayered, Visible Negative Index Metamaterials Formed by Nanotransfer Printing. *Advanced Optical Materials*, 2(3):256–261, 2014.

[111] D Chanda, K Shigeta, S Gupta, T Cain, A Carlson, A Mihi, A J Baca, G R Bogart, P Braun, and J A Rogers. Large-area flexible 3D optical negative index metamaterial formed by nanotransfer printing. *Nature Nanotechnology*, 6(7):402–407, 2011.

[112] U K Chettiar, A V Kildishev, H-K Yuan, W Cai, S Xiao, V P Drachev, and V M Shalaev. Dual-band negative index metamaterial: double negative at 813 nm and single negative at 772 nm. *OPTICS LETTERS*, 32(12):1671–1673, 2007.

[113] A Vázquez-Guardado, A Safaei, S Modak, D Franklin, and D Chanda. Hybrid coupling mechanism in a system supporting high order diffraction, plasmonic, and cavity resonances. *Physical Review Letters*, 113(26):263902, 2014.

[114] G Ameling and H Giessen. Microcavity plasmonics: strong coupling of photonic cavities and plasmons. *Laser & Photonics Reviews*, 7(2):141–169, 2012.

[115] F J García de Abajo. Colloquium: Light scattering by particle and hole arrays. *Reviews of Modern Physics*, 79(4):1267–1290, 2007.

[116] T R Jensen, G C Schatz, and R P Van Duyne. Nanosphere lithography: surface plasmon resonance spectrum of a periodic array of silver nanoparticles by ultraviolet-visible extinction spectroscopy and electrodynamic modeling. *The Journal of Physical Chemistry B*, 103(13):2394–2401, 1999.

[117] W-H Yang, G C Schatz, and R P Van Duyne. Discrete dipole approximation for calculating extinction and Raman intensities for small particles with arbitrary shapes. *Journal of Chemical Physics*, 103(3):869–875, 1995.

[118] P C Chaumet, T Zhang, A Rahmani, B Gralak, and K Belkebir. Discrete dipole approximation in time domain through the Laplace transform. *Physical Review E*, 88(6):063303, 2013.

[119] I G Savenko, R G Polozkov, and I A Shelykh. Giant Rabi splitting in a metallic cluster–cavity system. *Journal of Physics B: Atomic, Molecular and Optical Physics*, 45(4):045101, 2012.

[120] S Savasta, R Saija, A Ridolfo, O Di Stefano, P Denti, and F Borghese. Nanopolaritons: Vacuum Rabi Splitting with a Single Quantum Dot in the Center of a Dimer Nanoantenna. *ACS Nano*, 4(11):6369–6376, 2010.

[121] A Ji, T V Raziman, J Butet, R P Sharma, and O J F Martin. Optical forces and torques on realistic plasmonic nanostructures: a surface integral approach. *OPTICS LETTERS*, 39(16):4699–4702, 2014.

[122] M Moocarme, B Kusin, and L T V. Plasmon-induced lorentz forces of nanowire chiral hybrid modes. *Opt. Mater. Express*, 4(11):2355–2367, 2014.

[123] J Berthelot, S S Aćimović, M L Juan, M P Kreuzer, J Renger, and R Quidant. Three-dimensional manipulation with scanning near-field optical nanotweezers. *Nature Nanotechnology*, 9(4):295–299, 2014.

[124] E Sugawara, J-I Kato, Y Yamagata, M Ozaki, and R Furutani. Plasmonic trapping of submicro objects with metallic antennae. *Journal of Optics*, 18(7):075001, 2016.

[125] D C Marinica, M Zapata, P Nordlander, A K Kazansky, P M Echenique, J Aizpurua, and A G Borisov. Active quantum plasmonics. *Science Advances*, 1(11):e1501095–e1501095, 2015.

[126] W Fan, B J Lawrie, and R C Pooser. Quantum plasmonic sensing. *Physical Review A*, 92(5):053812, 2015.

[127] W Yan, M Wubs, and N Asger Mortensen. Projected Dipole Model for Quantum Plasmonics. *Physical Review Letters*, 115(13):137403, 2015.

[128] W Yan. Hydrodynamic theory for quantum plasmonics: Linear-response dynamics of the inhomogeneous electron gas. *Physical Review B*, 91(11):115416, 2015.

[129] M S Tame, K R McEnery, Ş K Özdemir, J Lee, S A Maier, and M S Kim. Quantum plasmonics. *Nature Physics*, 9(6):329–340, 2013.

[130] C Lee, M Tame, J Lim, and J Lee. Quantum plasmonics with a metal nanoparticle array. *Physical Review A*, 85(6):063823–18, 2012.

[131] Z Xi, Y Lu, W Yu, P Yao, P Wang, and H Ming. Strong coupling between plasmonic Fabry–Pérot cavity mode and magnetic plasmon. *Optics Letters*, 38(10):1591, 2013.

[132] J Cesario, R Quidant, G Badenes, and S Enoch. Electromagnetic coupling between a metal nanoparticle grating and a metallic surface. *Optics Letters*, 30(24):3404–3406, 2005.

[133] D Chanda, K Shigeta, T Truong, E Lui, A Mihi, M Schulmerich, P V Braun, R Bhargava, and J A Rogers. Coupling of plasmonic and optical cavity modes in quasi-three-dimensional plasmonic crystals. *Nature Communications*, 2:479–7, 2011.

[134] P Jouy, Y Todorov, A Vasanelli, R Colombelli, I Sagnes, and C Sirtori. Coupling of a surface plasmon with localized subwavelength microcavity modes. *Applied Physics Letters*, 98(2):021105, 2011.

[135] R Ameling, D Dregely, and H Giessen. Strong coupling of localized and surface plasmons to microcavity modes. *Optics Letters*, 36(12):2218–2220, 2011.

[136] L Fu, P Schau, K Frenner, W Osten, T Weiss, H Schweizer, and H Giessen. Mode coupling and interaction in a plasmonic microcavity with resonant mirrors. *Physical Review B*, 84(23):235402, 2011.

[137] R Taubert, R Ameling, T Weiss, A Christ, and H Giessen. From Near-Field to Far-Field Coupling in the Third Dimension: Retarded Interaction of Particle Plasmons. *Nano Letters*, 11(10):4421–4424, 2011.

[138] T Weiss, N A Gippius, G Granet, S G Tikhodeev, R Taubert, L Fu, H Schweizer, and H Giessen. Strong resonant mode coupling of Fabry–Perot and grating resonances in stacked two-layer systems. *Photonics and Nanostructures - Fundamentals and Applications*, 9(4):390–397, 2011.

[139] A Christ, S Tikhodeev, N Gippius, J Kuhl, and H Giessen. Waveguide-Plasmon Polaritons: Strong Coupling of Photonic and Electronic Resonances in a Metallic Photonic Crystal Slab. *Physical Review Letters*, 91(18):183901, 2003.

[140] B Auguié, X M Bendaña, W L Barnes, and F J García de Abajo. Diffractive arrays of gold nanoparticles near an interface: Critical role of the substrate. *Physical Review B*, 82(15):155447, 2010.

[141] A Yariv and P Yeh. *Photonics*. Optical Electronics in Modern Communications. Oxford University Press, 2007.

[142] X Chen, T Grzegorczyk, B-I Wu, J Pacheco, and J Kong. Robust method to retrieve the constitutive effective parameters of metamaterials. *Physical Review E*, 70(1):016608, 2004.

[143] D R Smith, S Schultz, P Markoš, and C M Soukoulis. Determination of effective permittivity and permeability of metamaterials from reflection and transmission coefficients. *Physical Review B*, 65(19):195104, 2002.

[144] C Menzel, C Rockstuhl, T Paul, F Lederer, and T Pertsch. Retrieving effective parameters for metamaterials at oblique incidence. *Physical Review B*, 77(19):195328, 2008.

[145] E D Palik. *Handbook of Optical Constants of Solids*. Academic Press, 1998.

[146] D B Amabilino. *Chirality at the Nanoscale*. Nanoparticles, Surfaces, Materials and More. Wiley-VCH, Weinheim, Germany, 2009.

[147] D M Lipkin. Existence of a new conservation law in electromagnetic theory. *Journal of Mathematical Physics*, 5(5):696–700, 1964.

[148] Y Tang and A E Cohen. Optical Chirality and Its Interaction with Matter. *Physical Review Letters*, 104(16):163901, 2010.

[149] L D Barron. *Molecular Light Scattering and Optical Activity*. Cambridge University Press, 2004.

[150] Y Tang and A E Cohen. Enhanced enantioselectivity in excitation of chiral molecules by superchiral light. *Science*, 332(6027):333–336, 2011.

[151] A Papakostas, A Potts, D M Bagnall, and S L Prosvirnin. Optical manifestations of planar chirality. *Physical Review Letters*, 90(10):107404, 2003.

[152] A S Schwanecke, A Krasavin, D M Bagnall, and A Potts. Broken time reversal of light interaction with planar chiral nanostructures. *Physical Review Letters*, 91(24):247404, 2003.

[153] S Prosvirnin and N Zheludev. Polarization effects in the diffraction of light by a planar chiral structure. *Physical Review E*, 71(3):037603, 2005.

[154] M Reichelt, S W Koch, A V Krasavin, J V Moloney, A S Schwanecke, T Stroucken, E M Wright, and N I Zheludev. Broken enantiomeric symmetry for electromagnetic waves interacting with planar chiral nanostructures. *Appl Phys B*, 84(1-2):97–101, 2006.

[155] J K Gansel, M Wegener, S Burger, and S Linden. Gold helix photonic metamaterials: a numerical parameter study. *Optics Express*, 18(2):1059–1069, 2010.

[156] S V Zhukovsky, C Kremers, and D N Chigrin. Plasmonic rod dimers as elementary planar chiral meta-atoms. *Optics Letters*, 36:2278, 2011.

[157] D N Chigrin, C Kremers, and S V Zhukovsky. Plasmonic nanoparticle monomers and dimers: from nanoantennas to chiral metamaterials. *Appl Phys B*, 105(1):81–97, 2011.

[158] F Eftekhari and T J Davis. Strong chiral optical response from planar arrays of subwavelength metallic structures supporting surface plasmon resonances. *Physical Review B*, 86(7):075428–7, 2012.

[159] M H Alizadeh and B M Reinhard. Plasmonically Enhanced Chiral Optical Fields and Forces in Achiral Split Ring Resonators. *ACS Photonics*, 2(3):361–368, 2015.

[160] E Hendry, R V Mikhaylovskiy, L D Barron, M Kadodwala, and T J Davis. Chiral Electromagnetic Fields Generated by Arrays of Nanoslits. *Nano Letters*, 12:3640–3644, 2012.

[161] R Tullius, A S Karimullah, M Rodier, B Fitzpatrick, N Gadegaard, L D Barron, V M Rotello, G Cooke, A Lapthorn, and M Kadodwala. "Superchiral" Spectroscopy: Detection of Protein Higher Order Hierarchical Structure with Chiral Plasmonic Nanostructures. *Journal of the American Chemical Society*, 137(26):8380–8383, 2015.

[162] M Hentschel, V E Ferry, and A P Alivisatos. Optical Rotation Reversal in the Optical Response of Chiral Plasmonic Nanosystems: The Role of Plasmon Hybridization. *ACS Photonics*, 2(9):1253–1259, 2015.

[163] J T Collins, C Kuppe, D C Hooper, C Sibilia, M Centini, and V K Valev. Chirality and Chiroptical Effects in Metal Nanostructures: Fundamentals and Current Trends. *Advanced Optical Materials*, 5:1700182, 2017.

[164] M L Nesterov, X Yin, M Schäferling, H Giessen, and T Weiss. The Role of Plasmon-Generated Near Fields for Enhanced Circular Dichroism Spectroscopy. *ACS Photonics*, 3(4):578–583, 2016.

[165] M M Coles and D L Andrews. Chirality and angular momentum in optical radiation. *Physical Review A*, 85(6):16–7, 2012.

[166] K Y Bliokh and F Nori. Characterizing optical chirality. *Physical Review A*, 83(2):021803, 2011.

[167] S M Barnett, R P Cameron, and A M Yao. Duplex symmetry and its relation to the conservation of optical helicity. *Physical Review A*, 86(1):013845–4, 2012.

[168] E T Jaynes and F W Cummings. Comparison of quantum and semiclassical radiation theories with application to the beam maser. In *Proceedings of the IEEE*, pages 89–109, 1963.

[169] V G Kravets, F Schedin, R Jalil, L Britnell, R V Gorbachev, D Ansell, B Thackray, K S Novoselov, A K Geim, A V Kabashin, and A N Grigorenko. Singular phase nano-optics in plasmonic metamaterials for label-free single-molecule detection. *Nature materials*, 12(4):304–309, 2013.

[170] N Liu, M Mesch, T Weiss, M Hentschel, and H Giessen. Infrared Perfect Absorber and Its Application As Plasmonic Sensor. *Nano Letters*, 10(7):2342–2348, 2010.

[171] J C Hulteen and R.P. Van Duyne. Nanosphere lithography: a materials general fabrication process for periodic particle array surfaces. *Journal of Vacuum Science & Technology A*, 13(3):1553, 1995.

[172] H Fredriksson, Y Alaverdyan, A Dmitriev, C Langhammer, D S Sutherland, M Zäch, and B Kasemo. Hole–Mask Colloidal Lithography. *Advanced Materials*, 19(23):4297–4302, 2007.

[173] A Nemiroski, M Gonidec, J M Fox, P Jean-Remy, E Turnage, and G M Whitesides. Engineering Shadows to Fabricate Optical Metasurfaces. *ACS Nano*, 8(11):11061–11070, 2014.

[174] M D Malinsky, K L Kelly, G C Schatz, and R P Van Duyne. Chain Length Dependence and Sensing Capabilities of the Localized Surface Plasmon Resonance of Silver Nanoparticles Chemically Modified with Alkanethiol Self-Assembled Monolayers. *Journal of the American Chemical Society*, 123(7):1471–1482, 2001.

[175] X.-M. Zhao, Y. Xia, and G. M. Whitesides. Soft lithographic methods for nano-fabrication. *Journal of Materials Chemistry*, 7(7):1069–1074, 1997.

[176] J A Rogers and R G Nuzzo. Recent progress in soft lithography. *Materials Today*, 8(2):50–56, 2005.

[177] N Kooy, K Mohamed, L T Pin, and O S Guan. A review of roll-to-roll nanoimprint lithography. *Nanoscale Research Letters*, 9(1):320, 2014.

[178] A Vázquez-Guardado, A Smith, W Wilson, J Ortega, J M Perez, and D Chanda. Hybrid cavity-coupled plasmonic biosensors for low concentration, label-free and selective biomolecular detection. *Optics Express*, 24(22):25785–12, 2016.

[179] M E Stewart, N H Mack, V Malyarchuk, J A Soares, T-W Lee, S K Gray, R G Nuzzo, and J A Rogers. Quantitative Multispectral Biosensing and 1D Imaging Using Quasi-3D Plasmonic Crystals. *Proceedings of the National Academy of Sciences of the United States of America*, 103(46):17143–17148, 2006.

[180] V Malyarchuk, F Hua, N Mack, V Velasquez, J White, R Nuzzo, and J A Rogers. High performance plasmonic crystal sensor formed by soft nanoimprint lithography. *Optics Express*, 13(15):5669–5675, 2005.

[181] S-W Lee, K-S Lee, J Ahn, J-J Lee, M-G Kim, and Y-B Shin. Highly Sensitive Biosensing Using Arrays of Plasmonic Au Nanodisks Realized by Nanoimprint Lithography. *ACS Nano*, 5(2):897–904, 2011.

[182] A Cattoni, P Ghenuche, A-M Haghiri-Gosnet, D Decanini, J Chen, J-L Pelouard, and S Collin. λ 3/1000 Plasmonic Nanocavities for Biosensing Fabricated by Soft UV Nanoimprint Lithography. *Nano Letters*, 11(9):3557–3563, 2011.

[183] D Franklin, R Frank, S-T Wu, and D Chanda. Actively addressed single pixel full-colour plasmonic display. *Nature Communications*, 8:1–10, 2017.

[184] L Gao, K Shigeta, A Vázquez-Guardado, C J Progler, G R Bogart, J A Rogers, and D Chanda. Nanoimprinting Techniques for Large-Area Three-Dimensional Negative Index Metamaterials with Operation in the Visible and Telecom Bands. *ACS Nano*, pages 5535–5542, 2014.

[185] A Safaei, S Chandra, A Vázquez-Guardado, J Calderon, D Franklin, L Tetard, L Zhai, M N Leuenberger, and D Chanda. Dynamically tunable extraordinary light absorption in monolayer graphene. *Physical Review B*, 96(16):165431, 2017.

[186] J C Shin, D Chanda, W Chern, K J Yu, J A Rogers, and X Li. Experimental Study of Design Parameters in Silicon Micropillar Array Solar Cells Produced by Soft Lithography and Metal-Assisted Chemical Etching. *IEEE Journal of Photovoltaics*, 2(2):129–133, 2012.

[187] D Shir, J Yoon, D Chanda, J-H Ryu, and J A Rogers. Performance of Ultrathin Silicon Solar Microcells with Nanostructures of Relief Formed by Soft Imprint Lithography for Broad Band Absorption Enhancement. *Nano Letters*, 10(8):3041–3046, 2010.

[188] K J Yu, L Gao, J S Park, Y R Lee, C J Corcoran, R G Nuzzo, D Chanda, and J A Rogers. Light Trapping in Ultrathin Monocrystalline Silicon Solar Cells. *Advanced Energy Materials*, 3(11):1401–1406, 2013.

[189] S Loeb and W J Catalona. What to do with an abnormal PSA test. *The Oncologist*, 13(3):299–305, 2008.

[190] P L Mai, N Wentzensen, and M H Greene. Challenges Related to Developing Serum-Based Biomarkers for Early Ovarian Cancer Detection. *Cancer Prevention Research*, 4(3):303–306, 2011.

[191] A V Vlassov, S Magdaleno, R Setterquist, and R Conrad. Exosomes: Current knowledge of their composition, biological functions, and diagnostic and therapeutic potentials. *Bioquimica et Biophysica Acta - General Subjects*, 1820(7):940–948, 2012.

[192] P Kharaziha, S Ceder, Q Li, and T Panaretakis. Tumor cell-derived exosomes: A message in a bottle. *Biochimica et Biophysica Acta - Reviews on Cancer*, 1826(1):103–111, 2012.

[193] G W Litman, J P Rast, M J Shamblott, R N Haire, M Hulst, W Roess, R T Litman, K R Hinds-Frey, A Zilch, and C T Amemiya. Phylogenetic diversification of immunoglobulin genes and the antibody repertoire. *Molecular Biology and Evolution*, 10(1):60–72, 1993.

[194] D Wild. *The immunoassay handbook: theory and applications of ligand binding, ELISA and related techniques*. Elsevier, Amsterdam, 3 edition, 2005.

[195] M E Stewart, C R Anderton, L B Thompson, J Maria, S K Gray, J A Rogers, and R G Nuzzo. Nanostructured Plasmonic Sensors. *Chemical Reviews*, 108(2):494–521, 2008.

[196] S Chen, M Svedendahl, M Käll, L Gunnarsson, and A Dmitriev. Ultrahigh sensitivity made simple: nanoplasmonic label-free biosensing with an extremely low limit-of-detection for bacterial and cancer diagnostics. *Nanotechnology*, 20(43):434015–10, 2009.

[197] S Zhang, Y Moustafa, and Q Huo. Different Interaction Modes of Biomolecules with Citrate-Capped Gold Nanoparticles. *ACS Applied Materials & Interfaces*, 6(23):21184–21192, 2014.

[198] H Im, H Shao, Y Il Park, V M Peterson, C M Castro, R Weissleder, and H Lee. Label-free detection and molecular profiling of exosomes with a nano-plasmonic sensor. *Nature Biotechnology*, 32(5):490–495, 2014.

[199] S S Aćimović, M A Ortega, V Sanz, J Berthelot, J L Garcia-Cordero, J Renger, S J Maerkl, M P Kreuzer, and R Quidant. LSPR Chip for Parallel, Rapid, and Sensitive Detection of Cancer Markers in Serum. *Nano Letters*, 14(5):2636–2641, 2014.

[200] S Y Hwang, C H Yoon, J Y Jeon, S C Choi, and E K Lee. Quantitative assay of hepatitis B surface antigen by using surface plasmon resonance biosensor. *Biotechnology and Bioprocess Engineering*, 10(4):309–314, 2005.

[201] J W Chung, S D Kim, R Bernhardt, and J C Pyun. Application of SPR biosensor for medical diagnostics of human hepatitis B virus (hHBV). *Sensors and Actuators B: Chemical*, 111-112:416–422, 2005.

[202] A J Haes, L Chang, W L Klein, and R P Van Duyne. Detection of a Biomarker for Alzheimer's Disease from Synthetic and Clinical Samples Using a Nanoscale Optical Biosensor. *Journal of the American Chemical Society*, 127(7):2264–2271, 2005.

[203] M K Kang, J Lee, A H Nguyen, and S J Sim. Label-free detection of ApoE4-mediated β-amyloid aggregation on single nanoparticle uncovering Alzheimer's disease. *Biosensors and Bioelectronic*, 72:197–204, 2015.

[204] M Mesch, C Zhang, P V Braun, and H Giessen. Functionalized Hydrogel on Plasmonic Nanoantennas for Noninvasive Glucose Sensing. *ACS Photonics*, 2(4):475–480, 2015.

[205] C-A Peng and S Pachpinde. Longitudinal Plasmonic Detection of Glucose Using Gold Nanorods. *Nanomaterials and Nanotechnology*, 4:9, 2014.

[206] X Liu, S Zhang, P Tan, J Zhou, Y Huang, Z Nie, and S Yao. A plasmonic blood glucose monitor based on enzymatic etching of gold nanorods. *Chemical Communications*, 49(18):1856–3, 2013.

[207] M Cottat, N Thioune, A-M Gabudean, N Lidgi-Guigui, M Focsan, S Astilean, and M Lamy de la Chapelle. Localized Surface Plasmon Resonance (LSPR) Biosensor for the Protein Detection. *Plasmonics*, 8(2):699–704, 2012.

[208] J Zhao, A Das, X Zhang, G C Schatz, S G Sligar, and R P Van Duyne. Resonance Surface Plasmon Spectroscopy: Low Molecular Weight Substrate Binding to Cytochrome P450. *Journal of the American Chemical Society*, 128(34):11004–11005, 2006.

[209] L Guo, J A Jackman, H-H Yang, P Chen, N-J Cho, and D-H Kim. Strategies for enhancing the sensitivity of plasmonic nanosensors. *Nano Today*, 10(2):213–239, 2015.

[210] J Li, J Ye, C Chen, Y Li, N Verellen, V V Moshchalkov, L Lagae, and P Van Dorpe. Revisiting the Surface Sensitivity of Nanoplasmonic Biosensors. *ACS Photonics*, 2(3):425–431, 2015.

[211] M A Otte, B Sepúlveda, W Ni, J Juste-Pérez, L M Liz-Marzán, and L M Lechuga. Identification of the Optimal Spectral Region for Plasmonic and Nanoplasmonic Sensing. *ACS Nano*, 4(1):349–357, 2010.

[212] G T Hermanson. *Bioconjugate Techniques*. Academic Press, Boston, 2013.

[213] L Guo, G Chen, and D-H Kim. Three-Dimensionally Assembled Gold Nanostructures for Plasmonic Biosensors. *Analytical Chemistry*, 82(12):5147–5153, 2010.

[214] L A Dubois and D K Gray. Dopamine-secreting Pheochromocytomas: In Search of a Syndrome. *World Journal of Surgery*, 29(7):909–913, 2005.

[215] P A Tippett, A J McEwan, and D M Ackery. A re-evaluation of dopamine excretion in phaeochromocytoma. *Clinical Endocrinology*, 25(4):401–410, 1986.

[216] W Januszewicz, B Wocial, A Januszewicz, P Gryglas, and A Prejbisz. Dopamine and dopa urinary excretion in patients with pheochromocytoma–diagnostic implications. *Blood pressure*, 10(4):212–216, 2001.

[217] B Anagnoste, L S Freedman, M Goldstein, J Broome, and K Fuxe. Dopamine-β-Hydroxylase Activity in Mouse Neuroblastoma Tumors and in Cell Cultures. *Proceedings of the National Academy of Sciences*, 69(7):1883–1886, 1972.

[218] A N A Van Der Horst-Schrivers, T E Osinga, I P Kema, B F A M Van Der Laan, and R P F Dullaart. Dopamine Excess in Patients with Head and Neck Paragangliomas. *Anticancer research*, 30(12):5153–5158, 2010.

[219] A W E Soh and P C Kek. Dopamine-secreting Carotid Body Paragangliomas-Biochemical Control with Radiotherapy. *Internal Medicine*, 51(6):613–618, 2012.

[220] J W Yi, E M Oh, K E Lee, and J Y Choi. An exclusively dopamine secreting paraganglioma in the retroperitoneum: a first clinical case in Korea. *Journal of the Korean Surgical Society*, 2012.

[221] G Eisenhofer, D S Goldstein, P Sullivan, G Csako, F M Brouwers, E W Lai, K T Adams, and K Pacak. Biochemical and Clinical Manifestations of Dopamine-Producing Paragangliomas: Utility of Plasma Methoxytyramine. *The Journal of Clinical Endocrinology & Metabolism*, 90(4):2068–2075, 2005.

[222] K L Adams, M Puchades, and A G Ewing. In Vitro Electrochemistry of Biological Systems. *Annual review of analytical chemistry (Palo Alto, Calif.)*, 1(1):329–355, 2008.

[223] D L Robinson, A Hermans, A T Seipel, and R M Wightman. Monitoring Rapid Chemical Communication in the Brain. *Chemical Reviews*, 108(7):2554–2584, 2008.

[224] S Sansuk, E Bitziou, M B Joseph, and J A Covington. Ultrasensitive detection of dopamine using a carbon nanotube network microfluidic flow electrode. *Analytical ...*, 85(1):163–169, 2012.

[225] P Gil-Loyzaga and N Parés-Herbute. HPLC detection of dopamine and noradrenaline in the cochlea of adult and developing rats. *Brain research. Developmental brain research*, 48(1):157–160, 1989.

[226] R Baron, M Zayats, and I Willner. Dopamine-, L-DOPA-, adrenaline-, and noradrenaline-induced growth of Au nanoparticles: assays for the detection of neurotransmitters and of tyrosinase activity. *Analytical Chemistry*, 77(6):1566–1571, 2005.

[227] K Liu, H Pang, J Zhang, H Huang, Q Liu, and Y Chu. Synthesis and characterization of a highly stable poly (3,4-ethylenedioxythiophene)-gold nanoparticles composite film and its application to electrochemical dopamine sensors. *RSC Advances*, 4(17):8415–8420, 2014.

[228] Y Lin, C Chen, C Wang, F Pu, J Ren, and X Qu. Silver nanoprobe for sensitive and selective colorimetric detection of dopamine via robust Ag-catechol interaction. *Chemical communications (Cambridge, England)*, 47(4):1181–1183, 2011.

[229] A Gutiérrez, A Gasnier, M L Pedano, J M Gonzalez-Dominguez, A Ansón-Casaos, J Hernández-Ferrer, L Galicia, M D Rubianes, M T Martínez, and G A Rivas. Electrochemical Sensor for the Quantification of Dopamine Using Glassy Carbon Electrodes Modified with Single-Wall Carbon Nanotubes Covalently Functionalized with Polylysine. *Electroanalysis*, 27(7):1565–1571, 2015.

[230] Y-R Kim, S Bong, Y-J Kang, Y Yang, R K Mahajan, J S Kim, and H Kim. Electrochemical detection of dopamine in the presence of ascorbic acid using graphene modified electrodes. *Biosensors and Bioelectronics*, 25(10):2366–2369, 2010.

[231] Y Liu, P She, J Gong, W Wu, S Xu, J Li, K Zhao, and A Deng. A novel sensor based on electrodeposited Au–Pt bimetallic nano-clusters decorated on graphene oxide (GO)–electrochemically reduced GO for sensitive detection of dopamine and uric acid. *Sensors and Actuators B: Chemical*, 221:1542–1553, 2015.

[232] Y Wang, Y Zhang, C Hou, and M Liu. Magnetic Fe3O4@MOFs decorated graphene nanocomposites as novel electrochemical sensor for ultrasensitive detection of dopamine.

RSC Advances, 5:98260–98268, 2015.

[233] J Jiang and X Du. Sensitive electrochemical sensors for simultaneous determination of ascorbic acid, dopamine, and uric acid based on Au@Pd-reduced graphene oxide nanocomposites. *Nanoscale*, 6:11303–11309, 2014.

[234] X Feng, Y Zhang, J Zhou, Y Li, S Chen, L Zhang, Y Ma, L Wang, and X Yan. Three-dimensional nitrogen-doped graphene as an ultrasensitive electrochemical sensor for the detection of dopamine. *Nanoscale*, 7(6):2427–2432, 2015.

[235] X Zhang, X Chen, S Kai, H-Y Wang, J Yang, F-G Wu, and Z Chen. Highly sensitive and selective detection of dopamine using one-pot synthesized highly photoluminescent silicon nanoparticles. *Analytical Chemistry*, 87(6):3360–3365, 2015.

[236] T Peik-See, A Pandikumar, H Nay-Ming, L Hong-Ngee, and Y Sulaiman. Simultaneous electrochemical detection of dopamine and ascorbic acid using an iron oxide/reduced graphene oxide modified glassy carbon electrode. *Sensors*, 14(8):15227–15243, 2014.

[237] D M Fernandes, M Costa, C Pereira, B Bachiller-Baeza, I Rodríguez-Ramos, A Guerrero-Ruiz, and C Freire. Novel electrochemical sensor based on N-doped carbon nanotubes and Fe3O4 nanoparticles: Simultaneous voltammetric determination of ascorbic acid, dopamine and uric acid. *Journal of Colloid And Interface Science*, 432:207–213, 2014.

[238] V Zucolotto, M Ferreira, and M R Cordeiro. Nanoscale processing of polyaniline and phthalocyanines for sensing applications. *Sensors and Actuators B*, 113(2):809–815, 2006.

[239] J S Lee, J Oh, S G Kim, and J Jang. Highly Sensitive and Selective Field-Effect-Transistor NonEnzyme Dopamine Sensors Based on Pt/Conducting Polymer Hybrid Nanoparticles. *Small*, 11(20):2399–2406, 2015.

[240] C Zhao, Z Jiang, X Cai, L Lin, X Lin, and S Weng. Ultrasensitive and reliable dopamine sensor based on polythionine/AuNPs composites. *JOURNAL OF ELECTROANALYTICAL CHEMISTRY*, 748:16–22, 2015.

[241] M Zhong, Y Teng, S Pang, L Yan, and X Kan. Pyrrole–phenylboronic acid: A novel monomer for dopamine recognition and detection based on imprinted electrochemical sensor. *Biosensors and Bioelectronic*, 64:212–218, 2015.

[242] G Xu, W Wang, B Li, Z Luo, and X Luo. A dopamine sensor based on a carbon paste electrode modified with DNA-doped poly(3,4-ethylenedioxythiophene). *Microchimica Acta*, 182(3-4):679–685, 2014.

[243] C Xue, Q Han, Y Wang, J Wu, T Wen, R Wang, J Hong, X Zhou, and H Jiang. Amperometric detection of dopamine in human serum by electrochemical sensor based on gold nanoparticles doped molecularly imprinted polymers. *Biosensors and Bioelectronic*, 49:199–203, 2013.

[244] Z Guo, G-Q Huang, J Li, Z-Y Wang, and X-F Xu. Graphene oxide-Ag/poly-l-lysine modified glassy carbon electrode as an electrochemical sensor for the determination of dopamine in the presence of ascorbic acid. *JOURNAL OF ELECTROANALYTICAL CHEMISTRY*, 759(Part 2):113–121, 2015.

[245] A Babaei and M Afrasiabi. A glassy carbon electrode modified with MCM-41/nickel hydroxide nanoparticle/multiwalled carbon nanotube composite as a sensor for the simultaneous determination of dopamine, piroxicam, and cefixime. *Ionics*, 21(6):1731–1740, 2015.

[246] R Suresh, K Giribabu, R Manigandan, S Praveen Kumar, S Munusamy, S Muthamizh, A Stephen, and V Narayanan. New electrochemical sensor based on Ni-doped V2O5 nanoplates modified glassy carbon electrode for selective determination of dopamine at nanomolar level. *Sensors and Actuators B: Chemical*, 202:440–447, 2014.

[247] R K Shervedani and M Bagherzadeh. Determination of dopamine in the presence of high concentration of ascorbic acid by using gold cysteamine self-assembled monolayers as a nanosensor. *Sensors and Actuators B*, 115(2):614–621, 2006.

[248] J Li, X Li, Y Zhang, R Li, D Wu, B Du, Y Zhang, H Ma, and Q Wei. Electrochemiluminescence sensor based on cationic polythiophene derivative and NH2–graphene for dopamine

detection. *RSC Advances*, 5:5432–5437, 2014.

[249] N Fourati, M Seydou, C Zerrouki, A Singh, S Samanta, F Maurel, D K Aswal, and M Chehimi. Ultrasensitive and Selective Detection of Dopamine Using Cobalt-Phthalocyanine Nanopillar-Based Surface Acoustic Wave Sensor. *ACS Applied Materials & Interfaces*, 6(24):22378–22386, 2014.

[250] M Li, W Guo, H Li, W Dai, and B Yang. Electrochemical biosensor based on one-dimensional MgO nanostructures for the simultaneous determination of ascorbic acid, dopamine, and uric acid. *Sensors and Actuators B: Chemical*, 204:629–636, 2014.

[251] S Elhag, Z H Ibupoto, X Liu, O Nur, and M Willander. Dopamine wide range detection sensor based on modified Co3O4 nanowires electrode. *Sensors and Actuators B: Chemical*, 203:543–549, 2014.

[252] L Li, L Yang, Y Teng, M Zhong, X Lu, and X Kan. Preparation and Application of Imprinted Electrochemical Sensor Based on Dopamine Self-Polymerization. *Journal of the Electrochemical Society*, 161(14):B312–B316, 2014.

[253] B Wu, C Miao, L Yu, Z Wang, C Huang, and N Jia. Sensitive electrochemiluminescence sensor based on ordered mesoporous carbon composite film for dopamine. *Sensors and Actuators B: Chemical*, 195:22–27, 2014.

[254] D G Gardner and D Shoback. *Greenspan's Basic and Clinical Endocrinology*. McGraw-Hill Companies, 9 edition, 2011.

[255] D R Raj, S Prasanth, T V Vineeshkumar, and C Sudarsanakumar. Surface plasmon resonance based fiber optic dopamine sensor using green synthesized silver nanoparticles. *Sensors and Actuators B: Chemical*, 224:600–606, 2015.

[256] J-H Choi, J-H Lee, B-K Oh, and J-W Choi. Localized Surface Plasmon Resonance-Based Label-Free Biosensor for Highly Sensitive Detection of Dopamine. *Journal of Nanoscience and Nanotechnology*, 14(8):5658–5661, 2014.

[257] Y Choi, J-H Choi, L Liu, B-K Oh, and S Park. Optical Sensitivity Comparison of Multiblock Gold–Silver Nanorods Toward Biomolecule Detection: Quadrupole Surface Plasmonic Detection of Dopamine. *Chemistry of Materials*, 25(6):919–926, 2013.

[258] M Reza Hormozi Nezhad, J Tashkhourian, J Khodaveisi, and M Reza Khoshi. Simultaneous colorimetric determination of dopamine and ascorbic acid based on the surface plasmon resonance band of colloidal silver nanoparticles using artificial neural networks. *Analytical Methods*, 2(9):1263–1269, 2010.

[259] J Biswal, N Misra, L C Borde, and S Sabharwal. Synthesis of silver nanoparticles in methacrylic acid solution by gamma radiolysis and their application for estimation of dopamine at low concentrations. *Radiation Physics and Chemistry*, 83:67–73, 2013.

[260] D Sebők, E Csapó, T Preočanin, G Bohus, N Kallay, and I Dékány. Adsorption of Ibuprofen and Dopamine on Functionalized Gold Using Surface Plasmon Resonance Spectroscopy at Solid-Liquid Interface. *Croatica Chemica Acta*, 86(3):287–295, 2013.

[261] S Kumbhat, D R Shankaran, S J Kim, K V Gobi, V Joshi, and N Miura. A novel receptor-based surface-plasmon-resonance affinity biosensor for highly sensitive and selective detection of dopamine. *Chemistry Letters*, 35(6):678–679, 2006.

[262] J Matsui, K Akamatsu, N Hara, D Miyoshi, H Nawafune, K Tamaki, and N Sugimoto. SPR Sensor Chip for Detection of Small Molecules Using Molecularly Imprinted Polymer with Embedded Gold Nanoparticles. *Analytical Chemistry*, 77(13):4282–4285, 2005.

[263] K Reed, A Cormack, A Kulkarni, M Mayton, D Sayle, F Klaessig, and B Stadler. Exploring the properties and applications of nanoceria: is there still plenty of room at the bottom? *Environmental Science: Nano*, 1:390–405, 2014.

[264] A S Karakoti, N A Monteiro-Riviere, R Aggarwal, J P Davis, R J Narayan, W T Self, J McGinnis, and S Seal. Nanoceria as Antioxidant: Synthesis and Biomedical Applications. *JOM (Warrendale, Pa. : 1989)*, 60(3):33–37, 2008.

[265] S Das, J M Dowding, K E Klump, J F McGinnis, W Self, and S Seal. Cerium oxide nanoparticles: applications and prospects in nanomedicine. *Nanomedicine*, 8(9):1483–1508, 2013.

[266] G Bulbul, A Hayat, X Liu, and S Andreescu. Reactivity of nanoceria particles exposed to biologically relevant catechol-containing molecules. *RSC Advances*, 6:60007–60014, 2016.

[267] W S Mielczarek, E A Obaje, T T Bachmann, and M Kersaudy-Kerhoas. Microfluidic Blood Plasma Separation for Medical Diagnostics: Is it Worth it? *Lab on a Chip*, 16:3441–3448, 2016.

[268] S Tripathi, Y V BalaVarun Kumar, A Agrawal, A Prabhakar, and S S Joshi. Microdevice for plasma separation from whole human blood using bio-physical and geometrical effects. *Scientific reports*, 6:26749, 2016.

[269] A Prabhakar, Y V Bala Varun Kumar, S Tripathi, and A Agrawal. A novel, compact and efficient microchannel arrangement with multiple hydrodynamic effects for blood plasma separation. *Microfluidics and Nanofluidics*, 18:995–1006, 2015.

[270] C Guo, R D Shah, R K Dukor, T B Freedman, X Cao, and L A Nafie. Fourier transform vibrational circular dichroism from 800 to 10,000 cm^{-1}: Near-IR-VCD spectral standards for terpenes and related molecules. *Vibrational Spectroscopy*, 42(2):254–272, 2006.